

Atmospheric Halocarbons

-

Detection of Previously Unobserved Compounds and Assessment of Mediterranean Emission Regions

A thesis submitted to attain the degree of
DOCTOR OF SCIENCES of ETH ZURICH
(Dr. sc. ETH Zurich)

presented by

FABIAN SCHOENENBERGER

MSc ETH in Atmospheric and Climate Science, ETH Zurich

born on 28.01.1984

citizen of Kirchberg SG

accepted on the recommendation of

Prof. Dr. Thomas Peter, examiner

Dr. Stefan Reimann, co-examiner

Prof. Dr. Andreas Engel, co-examiner

2016

*“It always seems impossible
until it’s done.”*

Nelson Mandela

Abstract

The group of halogenated greenhouse gases comprises chlorofluorocarbons (CFCs), hydrochlorofluorocarbons (HCFCs), hydrofluorocarbons (HFCs), chlorocarbons (e.g. CCl_4), bromocarbons (halons, CH_3Br) and several other fluorinated gases (e.g. SF_6 , NF_3). They are mainly used for applications such as refrigeration, air conditioning, foam blowing, and as solvents or propellants. Although they are satisfying the market's specific requirements, all of these substances are contributing to climate change and the chlorine and bromine-containing substances additionally destroy ozone in the stratosphere. As a consequence both, the Montreal Protocol and the Kyoto Protocol are aiming at reducing the emissions of these compounds. The Montreal Protocol by totally banning emissive uses of ozone-depleting substances and recently by also including a reduction scheme for HFCs. The Kyoto Protocol by including fluorinated gases into the basket of compounds to be reported as emissions by each country on a yearly basis. Country emission reports are based on so-called bottom-up inventories that are produced by combining emissions factors for individual processes with statistical information on their activity. This approach may involve relatively large uncertainties due to uncertain or missing data on source activities and related emission factors. In addition, the bottom-up estimate inhibits the potential weaknesses of omitting important source processes altogether, leading to incompleteness and underreporting. Therefore in recent years, top-down approaches, which combine atmospheric measurements with atmospheric transport and chemistry models, have been used in support of bottom-up inventories.

As part of this study we performed two measurement campaigns in the Mediterranean, where until now no long-term measurements of halogenated compounds have been available. These campaigns provided the basis for the first top-down emission estimates of halocarbons of several industrialized and densely populated Mediterranean regions. The first campaign was performed in the Eastern Mediterranean at Finokalia (Crete) in 2012-2013. By combining measurements from Finokalia, Jungfrauoch, Mace Head and Mt. Cimone with meteorological transport models, emissions from cities and industrialized regions in Greece, Turkey and Egypt could be estimated. Emissions of the groups of analysed HFCs (HFC-134a, HFC-125, HFC-152a, HFC-143a) and HCFCs (HCFC-22, HCFC-142b) were estimated at 14.7 (6.7 - 23.3) $\text{Tg CO}_2\text{eq yr}^{-1}$ and 9.7 (4.3 - 15.7) $\text{Tg CO}_2\text{eq yr}^{-1}$, respectively for the Eastern Mediterranean region. These findings account for a $\sim 17\%$ and $\sim 53\%$

share of total European domain emissions as derived from our top-down assessment. The comparison with bottom-up emission inventories from these countries showed a good agreement for most compounds, except for large discrepancies for HFC-152a, for which UNFCCC reported emissions from Greece were more than a factor of four larger than our top-down estimate. The second campaign was performed at the high-mountain site Pic du Midi (French Pyrenees) in 2013-2015, where emissions related to densely populated areas in Spain and in France could be assessed. An inverse estimate of total HFC-134a and HFC-125 emissions from the Iberian Peninsula was relatively insensitive to utilisation of the additional measurements from Pic du Midi in addition to those from the three existing sites at Jungfraujoch, Mace Head and Mt. Cimone. However, a more detailed spatial allocation could be achieved when using the Pic du Midi observations.

Many halocarbons in the atmosphere are not monitored on a regular basis, as they have never been produced in large quantities and for this reason emissions are assumed to be negligible. Therefore, an additional key contribution of this thesis was the detection of previously unreported atmospheric halocarbons. It was possible to detect HCFC-31 (CH_2ClF) in the atmosphere for the first time world-wide. Northern hemispheric records showed that HCFC-31 concentrations were peaking in 2012 at ~ 170 ppq (parts-per-quadrillion, 10^{-15}) and decreasing afterwards. The measured mole fractions were used in a global 12-box model to estimate global peak emissions of 840 t yr^{-1} ($\pm 90 \text{ t yr}^{-1}$) in 2011. The origin of the atmospheric HCFC-31 could be traced to emissions from the industrial production of HFC-32 (CH_2F_2). In this large-scale process hydrofluoric acid (HF) is used to exchange the chlorine atoms in dichloromethane (CH_2Cl_2) with fluorine. However, if the conversion is not complete, HCFC-31 is formed as a by-product. In recent years, global HFC-32 production has been rising continuously. Therefore, the recent decline in emissions of HCFC-31 could point to improvements in the production process.

This study shows the potential of the combination of measurements and meteorological transport models to act as an early warning tool for newly emitted gases and to estimate regional scale emissions in regions with limited information on emissions factors and activity data. In future, with application on the global scale, this could contribute to building trust between different countries related to their relative greenhouse gas emission inventories.

Zusammenfassung

Die Gruppe der halogenierten Treibhausgase umfasst Fluorchlorkohlenwasserstoffe (FCKWs), teilhalogenierte Fluorchlorkohlenwasserstoffe (HFCKWs), Fluorkohlenwasserstoffe (HFKWs), Chlorkohlenstoffe (z.B. CCl_4), bromierte Kohlenstoffe (z.B. Halone, CH_3Br) und eine Vielzahl anderer fluorierte Gase (z.B. SF_6 , NF_3). Diese Substanzen werden hauptsächlich in Kühlanlagen, Klimageräten, Schaumstoffen, sowie als Lösungs- oder Treibmittel eingesetzt und erfüllen die dabei an sie gestellten Anforderungen der Industrie perfekt. Allerdings tragen sie auch zur Klimaänderung bei und die mit Chlor und Brom versehenen Verbindungen sind zusätzlich in der Lage stratosphärisches Ozon abzubauen. Als Konsequenz dieser Umweltgefahren wurden internationale Abkommen wie das Montreal Protokoll und das Kyoto Protokoll ausgearbeitet, deren Ziel es ist, die Emissionen solcher Substanzen zu reduzieren. So wurde der Ausstoß und der Gebrauch von ozonabbauenden Substanzen unter dem Montreal Protokoll verboten und erst kürzlich ein Reduktionsplan für die Benützung von Fluorkohlenwasserstoffen verabschiedet. Im Rahmen des Kyoto Protokolls hingegen müssen die Emissionen gelisteter Treibhausgase, die auch fluorierte Verbindungen umfassen, jährlich von den jeweiligen Ländern rapportiert werden. Diese sogenannten bottom-up Inventare beruhen auf der Kombination von Emissionsfaktoren von spezifischen Prozessen und deren Aktivität. Wegen unsicherer oder fehlender Daten über quellenspezifische Aktivitäten und deren Emissionsfaktoren ist dieser Ansatz jedoch fehleranfällig. Zusätzlich könnten wichtige Quellen übersehen werden, was zu unvollständigen und unterschätzten Emissionszahlen führen würde. Um diese klassischen bottom-up Inventare zu unterstützen und zu validieren wurden deshalb in den letzten Jahren top-down Methoden verwendet. Dabei werden Messungen der Mischungsverhältnisse der untersuchten Substanzen in der Atmosphäre kombiniert mit atmosphärischen Transportmodellen, um deren Emissionen abzuschätzen.

Im Rahmen der vorliegenden Arbeit wurden zwei Messkampagnen im Mittelmeerraum durchgeführt, wo bis anhin keine Langzeitbeobachtungen von halogenierten Substanzen existierten. Zum allerersten Mal konnten dadurch die Emissionen halogener Kohlenwasserstoffe aus mehreren industrialisierten und stark bevölkerten Regionen im mediterranen Raum abgeschätzt werden. Die erste Kampagne fand zwischen 2012 und 2013 im östlichen Mittelmeerraum in Finokalia (Kreta) statt. Durch die Kombination der erhobenen Messungen mit einem meteorologischen Transportmo-

dell konnten Emissionen von Städten und industrialisierten Regionen in Griechenland, der Türkei und Ägypten quantifiziert werden. Jährliche Emissionen der analysierten HFKWs (HFKW-134a, HFKW-125, HFKW-152a, HFKW-143a) und HFCKWs (HFCKW-22, HFCKW-142b) wurden für den östlichen Mittelmeerraum auf 14.7 (6.7-23.3) Tg CO₂eq beziehungsweise 9.7 (4.3-15.7) Tg CO₂eq geschätzt. Das entspricht einem Anteil von ~17% und ~53% an den totalen top-down Emissionen des untersuchten Europäischen Raums. Für die meisten Substanzen wurden die bottom-up Inventare durch die Analyse gestützt, ausser für HFKW-152a wo grössere Abweichungen festgestellt wurden. So waren die von Griechenland rapportierten Emissionen um mehr als Faktor 4 höher als die durch unsere top-down Methode ermittelten Werte. Eine zweite Messkampagne wurde von 2013 bis 2015 auf der hochalpinen Station Pic du Midi (Französische Pyrenäen) durchgeführt. Dieser Standort ermöglichte uns die Beobachtung und Quellzuordnung von Emissionen aus dichter besiedelten Gebieten in Spanien und Frankreich. Eine inverse Abschätzung der totalen Emissionen von HFKW-134a und HFKW-125 ergab, dass die zusätzlichen Messdaten keine grösseren Änderungen an den Emissionsabschätzungen durch die vorhandenen Messstationen Jungfraujoch, Mace Head und Mt. Cimone bewirken. Allerdings ermöglicht die Einbindung der Beobachtungen vom Pic du Midi eine höhere räumliche Auflösung der abgeschätzten Emissionen in dieser Region.

Viele der halogenierten Verbindungen in der Atmosphäre werden nicht kontinuierlich überwacht, da sie nie in grossen Mengen als Konsumgut produziert wurden und man deren Emissionen folglich als vernachlässigbar annimmt. Mit der vorliegenden Studie war es uns möglich erstmals weltweit HFCKW-31 (CH₂ClF) in der Atmosphäre nachzuweisen. In der Nordhemisphäre zeigten die HFCKW-31 Messungen einen Höhepunkt der atmosphärischen Mischungsverhältnisse im Jahr 2012 mit ~170 ppq (parts-per-quadrillion, 10⁻¹⁵), sowie einen negativen Trend in den Jahren danach. Mit Hilfe der Messwerte und einem globalen 12-box Modell wurden in 2012 weltweite Emissionen von bis zu 840 t (± 90 t) ermittelt. Die Entstehung von atmosphärischem HFCKW-31 konnte auf die Herstellung des Kühlmittels HFKW-32 (CH₂F₂) zurückgeführt werden. Bei der Produktion von HFKW-32 wird Flussäure (HF) zu Dichlormethan (CH₂Cl₂) zugefügt, was unter ungenügend kontrollierten Prozessbedingungen zur Bildung von HCFC-31 als Beiprodukt führt. In den letzten Jahren hat die Produktion von HFKW-32 laufend zugenommen. Obwohl die Produktion von HFKW-32 weltweit immer noch zunimmt, wurden nach 2011 abnehmende Emissionen abgeschätzt, was auf verbesserte Produktionsbedingungen zurückzuführen sein könnte.

Die Messungen und Analysen, die im Rahmen dieser Arbeit durchgeführt wurden, dienen einerseits als Frühwarnsystem um die Konzentration von neu emittierten Gasen in der Atmosphäre zu über-

prüfen und deren Quellen zu ermitteln. Andererseits bietet die Kombination von atmosphärischen Messungen und meteorologischen Transportmodellen eine Möglichkeit regionale Emissionen abzuschätzen – vor allem in Regionen mit limitierten Informationen über Emissionsfaktoren und Aktivitäten. Auf globaler Basis könnte dies dazu beitragen, das gegenseitige Vertrauen der verschiedenen Länder in die rapportierten Treibhausgasinventare zu stärken.

Contents

Abstract	v
Zusammenfassung	vii
List of Figures	xiii
List of Tables.....	xv
List of Abbreviations	xvi
Chapter 1 Introduction	1
Chapter 2 Scientific Background	7
2.1 General Properties of Halocarbons	7
2.2 Environmental Impact of Anthropogenic Halocarbons.....	9
2.3 Regulatory Treaties for Halocarbons	10
2.4 Observations of Atmospheric Halocarbons	13
2.5 Atmospheric Transport Models and Emission Estimation.....	15
Chapter 3 Methods	19
3.1 Instrumentation.....	19
3.2 Empa-2013 Primary Standard Preparation and Halocarbon Identification	20
3.3 Lagrangian Particle Dispersion Model (FLEXPART).....	23
3.4 Atmospheric Bayesian Inversion	25
Chapter 4 First observations, trends and emissions of HCFC-31 (CH₂ClF) in the global atmosphere	29
Abstract.....	29
4.1 Introduction	29
4.2 Methods	31
4.2.1 Measurements	31
4.2.2 Analytical Setup.....	32
4.2.3 Modelling.....	34
4.3 Results and Discussion	34
4.3.1 Observations.....	34
4.3.2 Emissions and Potential Sources	36
4.4 Conclusion.....	38
Acknowledgements	39

Chapter 5	Abundance and sources of atmospheric halocarbons in the Eastern Mediterranean	41
	Abstract	41
5.1	Introduction	42
5.2	Methods	44
5.2.1	Observational Sites	44
5.2.2	Analytical Methods	45
5.2.3	Data Treatment	45
5.2.4	Transport Simulations	47
5.2.5	Atmospheric Inversion	48
5.2.6	A priori Emissions	49
5.2.7	Covariance Treatment	51
5.2.8	Sensitivity Inversions	53
5.3	Results and Discussion	54
5.3.1	Flow Regime and Observations at Finokalia	54
5.3.2	Base Inversion	58
5.3.3	Sensitivity Inversions	62
5.3.4	Regional Total Emissions	66
5.3.5	Summary of Halocarbon Emissions	73
5.3.6	Temporal Variability of HFC-152a Emissions	74
5.3.7	The Impact of Halocarbon Observations at Finokalia	75
5.4	Conclusion	77
	Acknowledgements	79
Chapter 6	Halocarbon emissions on the Iberian Peninsula, inferred from atmospheric measurements in the French Pyrenees.	81
6.1	Site Description	81
6.2	Observations	82
6.2.1	Flask Samples and Local Pollution Sources	83
6.2.2	In situ Observations	86
6.3	Atmospheric Inversion Method	88
6.4	Simulated Mole Fractions	89
6.5	Regional Emission Estimates	91
Chapter 7	Conclusion and Outlook	95
	References	99
	Acknowledgements	113

List of Figures

Figure 1.1: Average sensitivity footprint of (a) the existing European AGAGE stations for the time period of both measurement campaigns and (b) for the AGAGE sites combined with the stations at Finokalia and Pic du Midi during the measurement campaigns.	4
Figure 2.1: Phase-down scheme for HFCs according to the 2016 Kigali Amendment to the Montreal Protocol. Dotted lines show the period which is used to define baseline figures for the respective groups of countries.	12
Figure 2.2: Global distribution of AGAGE and NOAA/GMD observation sites for halocarbons.	14
Figure 3.1: Schematic flow scheme of Medusa preconcentration unit (from <i>Miller, et al.</i> [2008]).	20
Figure 3.2: Schematic illustration of the Empa-2013 primary calibration standard preparation setup.	21
Figure 4.1: (A) Atmospheric record of HCFC-31 (CH_2ClF). Vertical bars: measurement precision ($\pm 1\sigma$) for flask measurements, often smaller than the symbol size, and $\pm 1\sigma$ for in situ measurements, referring to weekly means. Solid lines: dry air mole fractions from the AGAGE 12-box model for the model surface boxes 30°N to 90°N (in blue) and 30°S to 90°S (in red). (B) Growth rates derived from Figure 4.1A for dry air mole fractions in the model surface boxes. (C) Model-derived global emissions in t yr^{-1}	35
Figure 5.1: Illustration of region definition used in the discussion of emission estimates: Greece (light turquoise), Turkey (Turkey, Cyprus; pale yellow), Balkans (Serbia, Montenegro, Kosovo, Albania, Bosnia and Herzegovina, Croatia, Slovenia, Macedonia; light green), Eastern (Ukraine, Romania, Moldova, Bulgaria; pale pink), Middle East (Jordan, Lebanon, Syria, Palestine, Israel; blue), Egypt (pale purple), Maghreb (Morocco, Algeria, Tunisia, Libya; orange), Central E (Poland, Slovakia, Czech-Republic, Hungary; grey), Central W (Switzerland, Liechtenstein, Germany, Austria, Denmark; purple), Western (France, Luxembourg, Netherlands, Belgium; pale green), Italy (red), Iberian Peninsula (Spain, Portugal; yellow), British Isles (Ireland, United Kingdom; light turquoise).....	50
Figure 5.2: Average FLEXPART derived source sensitivities for Finokalia and two characteristic flow regimes during the measurement campaign: a) shows the variable flow during winter and spring and b) northeasterly flow during the summer months.....	55
Figure 5.3: Halocarbon observations in 2013, during the time of the measurement campaign in Finokalia (red) and simultaneous measurements at Jungfraujoch (purple) and Monte Cimone (green). The corresponding background estimated with REBS is shown in the darker shade of the respective color.	57
Figure 5.4: HFC-134a time series of the base inversion for 2013, showing the observed mole fractions at the respective sites (grey) and the simulated values (a priori: red; a posteriori: blue) and their baseline conditions (a priori: light red; a posteriori: light blue).	59
Figure 5.5: a) Emissions difference (posterior – prior) of the BASE inversion of HFC-134a. b) Relative reduction of the a posteriori uncertainty compared to the a priori uncertainties.	62
Figure 5.6: Difference of the a posteriori and a priori emissions for (a) the S-ML and (b) the S-MS inversions of HFC-134a. (c) regional emission estimates: a priori emissions (red) and a posteriori emissions (BASE = green, S-ML = blue, S-MS = purple). The uncertainties given are two standard deviations of the analytic uncertainty assigned to the a priori emissions and derived by the inversion as a posteriori uncertainties.	64
Figure 5.7: Difference of the a posteriori and a priori emissions for (a) the S-UH and (b) the S-UL inversions. (c) regional emission estimates: a priori emissions (red) and a posteriori emissions (BASE = green, S-UH = blue, S-UL = purple). The uncertainties given are two standard deviations of the analytic uncertainty assigned to the a priori emissions and derived by the inversion as a posteriori uncertainties.	65
Figure 5.8: Annual emissions for the aggregated regions. A priori emissions are shown in red, with uncertainty giving the 95% confidence range. For the a posteriori estimates boxes show the range of all sensitivity inversions, whereas the thick horizontal line gives the mean of all sensitivity inversions. In addition, the blue error bars give the analytic uncertainty (95% confidence level) averaged over all uncertainty inversions.	70

Figure 5.9: Annual per capita (p.C.) emissions in CO ₂ equivalents, derived from the base inversion and all sensitivity inversions. The results have been computed using the 100-yr GWP (GWP100) values of [Carpenter and Reimann, 2014]. The bars show the average mean of all inversions, whereas the error bars show our uncertainty estimate including analytical and structural uncertainty (see Section 5.3.4 for details).	73
Figure 5.10: Spatial distribution of the Pearson Correlation Coefficient (R) for (a) the entire time series of HFC-152a observations at Finokalia and the per-cell source sensitivity and for (b) the period of the pollution peaks, which are highlighted in red in (c) the observed (black) and simulated a posteriori (BASE inversion) (blue) mole fractions of HFC-152a.	74
Figure 5.11: Regional annual emission estimates of 2013. The a priori of our base inversion is shown in red. A posteriori results are shown for the BASE inversion (blue), the inversion excluding Finokalia (S-NFKL, green) and the inversion only using observations from Finokalia (S-OFKL, purple). Error bars represent the 95% confidence levels. Note that for the inversion based on Finokalia observations alone (S-OFKL) the inversion domain was cropped in the West and no a posteriori emission for the western part of the domain were estimated.	76
Figure 5.12: HFC-134a uncertainty reduction (%) achieved by (a) the inversion excluding observations from Finokalia (S-NFKL) and (b) the BASE inversion using observations from all four sites including Finokalia.	77
Figure 6.1: FLEXPART footprints during the Pic du Midi campaign period for the existing AGAGE network (a) and the AGAGE network including Pic du Midi.	82
Figure 6.2: Pic du Midi observations (unfiltered and filtered for assumed local pollution) for each compound. Mean wind direction during the sampling period of each individual observation is shown, as well as wind speed (calm conditions with wind speed < 5 m/s (red), normal to windy conditions with wind speed > 5 m/s (blue)).	85
Figure 6.3: Unfiltered observations from Pic du Midi (red), Mt. Cimone (green) and Jungfraujoch (purple) during the campaign period from Oct. 2013 – Jun. 2015.	86
Figure 6.4: Indication of regions/countries for which individual emission estimates were derived (the country abbreviations follow the ISO 2-letter country codes): United Kingdom, Ireland (UK-IR: green), Spain, Portugal (ES-PT: turquoise), France (FR: yellow), Italy (IT: blue), Switzerland, Austria, Liechtenstein (CH-AT-LI: purple), Belgium, Netherlands, Luxembourg (BE-NL-LU: orange), Germany, Denmark (DE-DK: red), Poland, Czech Republic, Slovakia, Hungary (PL-CZ-SK-HU: pink), Slovenia, Croatia (SI-HR: grey).	89
Figure 6.5: Observed (black) and simulated (prior: red; posterior: blue) HFC-134a time series at the four sites Pic du Midi (PDM), Jungfraujoch (JFJ), Monte Cimone (CMN) and Mace Head (MHD). Also given are the baseline mole fractions as used in the simulations (prior: light red; posterior: light blue). Note that the y axes were scaled for each site separately. All data represent 3-hourly averages.	90
Figure 6.6: Taylor plots of the model performance for (left) HFC-134a, (centre) HFC-125, (right) HFC-152a at the four observation sites and for (open symbols) a priori and (filled symbols) a posteriori emissions.	91
Figure 6.7: Annual average emissions for different Western and Central European countries/regions for the year 2014: (top) HFC-134a, (bottom) HFC-125. A priori values are given in red, a posteriori values in blue and green for the inversion with and without PDM, respectively. The error bars represent the 1-s uncertainty of the annual average emissions.	92
Figure 6.8: Annual average emission distribution of (top) HFC-134a, (middle) HFC-125 and (bottom) HFC-152a: (left) a priori, (centre) a posteriori difference with PDM, (right) a posteriori difference without PDM for the year 2014.	93

List of Tables

Table 2.1: Important representatives of four generations of halogenated compounds.	8
Table 5.1: Basic statistics for the 3-hourly aggregates of the observations taken at all sites during the campaign period (Dec. 2012 – Aug.2013). Observation sites are: Finokalia (FKL), Jungfraujoch (JFJ), Mace Head (MHD), Mt. Cimone (CMN). Shown are the number of observations (N), the mean, minimum (Min), maximum (Max) and standard deviation (SD) for the observations and the baseline values, estimated with REBS. The mean measurement uncertainty (σ_o) was determined from the standard deviation of reference gas measurements and the baseline uncertainty (σ_b) was derived as one constant value by the REBS method (see Section 5.2.3).	46
Table 5.2: Setup for the base inversion (Base) and the sensitivity inversions (S-XX). Method refers to the uncertainty treatment explained in Section 5.2.7. The sites are abbreviated as follows: Finokalia (FKL), Jungfraujoch (JFJ), Mace Head (MHD) and Monte Cimone (CMN).	53
Table 5.3: Inversion performance of the BASE inversion at Finokalia (FKL), Jungfraujoch (JFJ), Mace Head (MHD) and Monte Cimone (CMN). N is the number of observations used for the inversion. RMSE, R^2 and TSS denote the root mean square error, coefficient of determination and the Taylor skill score of the complete signal and R^2_{abg} is the coefficient of determination of the signal above background.	61
Table 5.4: Inversion performance of the base inversion and the sensitivity inversions S-ML and S-MS for HFC-134a at Finokalia (FKL), Jungfraujoch (JFJ), Mace Head (MHD) and Monte Cimone (CMN). N is the number of observations used for the inversion. RMSE is the root mean square error in ppt (parts per billion 10^{-12}). R^2 denotes the coefficient of determination of the complete signals and R^2_{abg} is the coefficient of determination of the signals above background. TSS shows the Taylor Skill Score of the entire signal.	63
Table 5.5: Regional emissions as estimated in the a priori inventory and by the atmospheric inversion. All values are given in in Mg yr ⁻¹ . A posteriori estimates are shown as the mean values, derived from the BASE inversion and the sensitivity inversions S-ML, S-MS, S-UH and S-UL. The uncertainty range gives the maximum range provided by the respective mean values of all inversions plus the mean of the analytic uncertainty ($p < 0.05$) estimated by each individual inversion. Smaller and distant countries were aggregated to larger regions: Turkey (Turkey, Cyprus), Balkans (Serbia, Montenegro, Kosovo, Albania, Bosnia and Herzegovina, Croatia, Slovenia, Macedonia), Eastern (Ukraine, Romania, Moldova, Bulgaria), Middle East (Jordan, Lebanon, Syria, Palestine, Israel), Maghreb (Morocco, Algeria, Tunisia, Libya), Central E (Poland, Slovakia, Czech-Republic, Hungary), Central W (Switzerland, Liechtenstein, Germany, Austria, Denmark), Western (France, Luxembourg, Netherlands, Belgium), Iberian Peninsula (Spain, Portugal), British Isles (Ireland, United Kingdom).	69
Table 6.1: Mole fraction measured in flask samples, taken throughout the observatory on Pic du Midi. Every flask was measured twice and the mean of both measurements is given. Location denotes the place where the flask sample was collected as well as the direction of the sample site as seen from the ADS air inlet on the roof of the Laboratory building. X is referring to a location in the same building on different levels of the laboratory building.	83
Table 6.2: Basic statistics for the observations taken during the Pic du Midi campaign. Observation sites are: Pic du Midi (PDM), Jungfraujoch (JFJ), Mace Head (MHD), Mt. Cimone (CMN). Shown are the number of observations (n.obs), the mean, minimum (min), maximum (max) and standard deviation (sd) of the observations and the background, which was estimated with REBS. The mean measurement uncertainty (mean unc) is the moving window uncertainty of the observations and the constant uncertainty (const unc) derived by REBS for the background.	87

List of Abbreviations

ADS	Adsorption-Desorption System
AGAGE	Advanced Global Atmospheric Gases Experiment
BLT	Bernard Lyot Telescope
CFC	Chlorofluorocarbon
CH ₄	Methane
CO	Carbon monoxide
CO ₂	Carbon dioxide
ECMWF	European Centre for Medium-Range Weather Forecasts
GC-MS	Gas Chromatography - Mass Spectrometry
GHG	Greenhouse gas
GWP	Global Warming Potential
Halon	Halogenated hydrocarbon containing both Cl or Br
HCFC	Hydrochlorofluorocarbon
HFC	Hydrofluorocarbon
HFO	Hydrofluoroolefine
IPCC	Intergovernmental Panel on Climate Change
LPDM	Lagrangian Particle Dispersion Model
PBL	Planetary Boundary Layer
NOAA	National Oceanic and Atmospheric Administration
ODP	Ozone Depletion Potential
ODS	Ozone Depleting Substances
PPT	Parts Per Trillion (10 ⁻¹²)
PPQ	Parts Per Quadrillion (10 ⁻¹⁵)
REBS	Robust Extraction of Baseline Signal
RMSE	Root Mean Square Error
SRR	Source Receptor Relationship
UNEP	United Nations Environmental Programme
UNFCCC	United Nations Framework Convention on Climate Change

Chapter 1 Introduction

The atmosphere is a comparatively small entity of the Earth. Therefore, even relatively small emissions of natural and anthropogenic substances can have a considerable influence on its physical and chemical properties. One group of these substances are the halogenated organic compounds, which are greenhouse gases and affect the global climate but some of which are also able to deplete the stratospheric ozone layer. For this reason, measurements of these compounds are of paramount interest to address relevant scientific questions related to these issues and also inform policy makers and the general public about their behaviour in the atmosphere.

Greenhouse gases (GHG), such as water vapour and carbon dioxide (CO₂), are of major importance for the Earth's radiative balance, due to their ability to absorb outgoing longwave radiation and emit it back to the Earth's surface. Since the start of industrialization, human activities have continued to affect the Earth's energy budget by adding GHGs to the system, enhancing their atmospheric levels to concentrations that are unprecedented in at least the last 800'000 years [*IPCC*, 2014b]. Although the complex reaction of the climate system to the additional burden of GHGs is not yet fully understood, there is widely accepted evidence, that the additional energy introduced into the system reflects itself through an increase in the average surface temperature, causing further consequences such as sea level rise or the alteration of the global atmospheric circulation, which may affect the likelihood of the occurrence and strength of extreme weather events such as heat waves, droughts or intense rainfall events. The continued increase of GHG concentrations in the atmosphere is predicted to cause further warming and subsequent changes in the Earth's vulnerable climate system, increasing the likelihood of irreversible impacts on ecosystems and humanity, thus making it one of the most important topics of today's society [*IPCC*, 2014a].

CO₂ is currently responsible for the largest part of the anthropogenic radiative forcing (1.82 Wm⁻²), and makes up for most of the anthropogenic GHG emissions together with CH₄ (methane) and N₂O (nitrous oxide) [*IPCC*, 2013]. Additionally, synthetic GHGs such as halocarbons and several fluorinated compounds (e.g. SF₆, NF₃) contribute substantially to global warming. Halocarbon is a collective term for organic substances containing fluorine, chlorine or bromine, which includes ozone

depleting substances (ODSs) such as chlorofluorocarbons (CFCs) and hydrochlorofluorocarbons (HCFCs), as well as non-ozone depleting hydrofluorocarbons (HFCs), perfluorocarbons (PFCs) and newer generations' hydrofluoroolefines (HFOs). These compounds have been used in a wide range of applications (e.g. refrigeration, air conditioning, foam blowing, solvent usage, aerosol propellants and fire retardants). An estimated $0.35 \pm 0.01 \text{ Wm}^{-2}$ of direct radiative forcing, are caused by the major long-lived synthetic GHGs (GHG with lifetimes of at least 1 year and no significant natural sources). This is equivalent to 19% of the radiative forcing increase due to CO_2 after industrialization started [Rigby, *et al.*, 2014].

While most halocarbons are only strong GHGs, because of their persistence in the atmosphere and their sometimes large greenhouse warming potentials (GWPs), earlier generation halocarbons such as CFCs and HCFCs in addition contribute to stratospheric ozone depletion. The scientific community proposed, that the chemical breakdown of these ODSs in the stratosphere releases chlorine and bromine radicals which are able to catalytically destroy ozone, leading to the so-called “ozone hole”, mostly occurring over Antarctica [Molina and Rowland, 1974; Farman, *et al.*, 1985]. These threatening findings led to the negotiation of the Montreal Protocol, which regulated ODSs, leading to the successful global phase-out of CFCs for emissive uses in 2010, thereby avoiding a predicted destruction of 67% of the globally-averaged column ozone by 2065 [Newman, *et al.*, 2009]. The regulations of ODSs by the Montreal Protocol forced the industry to replace CFCs with less harmful HCFCs used as transitional products. Although a less potent class of ODSs, HCFCs themselves are regulated by the Montreal Protocol with a less stringent phase-out schedule. They were subsequently replaced by chlorine-free HFCs, which are no longer harmful to the ozone layer, but some of them have large GWPs and are very persistent in the atmosphere. Therefore, they are regulated under the United Nations Framework Convention on Climate Change (UNFCCC) and the associated Kyoto Protocol. Although HFC emissions are still small in comparison to CO_2 emissions, without further regulations HFC emissions could have grown to 9-19 % of projected global CO_2 emissions by 2050 [Velders, *et al.*, 2009]. However, in the 2016 Kigali Amendment to the Montreal Protocol it was decided to phase-down the consumption of HFCs to around 15% of their original uses, accounted as CO_2 equivalents.

The protocols, under which the synthetic halocarbons are regulated, require the participating parties to quantify their countries' individual emissions, which are based on statistical data of production, consumption and destruction figures (bottom-up estimates). Using this method, reporting of ozone depleting halocarbons under the Montreal Protocol is performed globally and with the exception of

CCl_4 [SPARC, 2016] complies well with global emission estimates, using global box models and measurements [Carpenter and Reimann, 2014]. In the Kyoto-Protocol, however, bottom-up emissions only have to be reported by industrialized countries, which fails to account for an evergrowing part of global emissions. Furthermore, reporting to the Kyoto Protocol could carry significant uncertainties and the danger of incomplete reporting [Levin, *et al.*, 2010; Nisbet and Weiss, 2010; Keller, *et al.*, 2012; Rigby, *et al.*, 2014; Lunt, *et al.*, 2015]. Therefore, to verify these emissions, top-down approaches, based on atmospheric measurements and atmospheric transport and chemistry models have been introduced. Besides the validation of reported inventories, these methods have the additional benefit of being able to provide emission estimates in regions where bottom-up inventories are not available, such as in developing countries.

Combined with global scale box-models, atmospheric observations allow the independent monitoring of global emissions, based on changes in the atmospheric background concentrations [Rigby, *et al.*, 2010; Carpenter and Reimann, 2014; Laube, *et al.*, 2014; Schoenenberger, *et al.*, 2015; Vollmer, *et al.*, 2015b]. The advances in measurement techniques, both regarding their sensitivity and the temporal resolution, the increasing resolution of atmospheric transport models, and the increase in available computational power offer the opportunity to use more and more elaborate inversion methods. These allow the estimation of halocarbon emissions on either continental and country-level scales, which are then comparable with reported inventories [Manning, *et al.*, 2003; Stohl, *et al.*, 2009; Kim, *et al.*, 2010; Brunner, *et al.*, 2012a; Brunner, *et al.*, 2012b; Keller, *et al.*, 2012; Saikawa, *et al.*, 2012; Maione, *et al.*, 2014; Lunt, *et al.*, 2015; Henne, *et al.*, 2016]. However, the informative value of these estimates is limited by the availability of longer term continuous observations, the density of the observation networks, and the characteristics of the individual observation sites [Henne, *et al.*, 2010].

In Europe, the Advanced Global Atmospheric and Gases Experiment (AGAGE) network provides high-frequency measurements of atmospheric halocarbons at 4 sites: Mace Head (Ireland), Zeppelin mountain (Norway), Jungfraujoch (Switzerland) and Mt. Cimone (Italy) [Prinn, *et al.*, 2000]. Although data from this network have been frequently used to verify Western European halocarbon emissions [Reimann, *et al.*, 2008; Brunner, *et al.*, 2012b; Keller, *et al.*, 2012], Southern European regions such as the Iberian Peninsula and Southeastern Europe are underrepresented, making regional estimates based on measurements from the existing AGAGE network very uncertain (Figure 1.1).

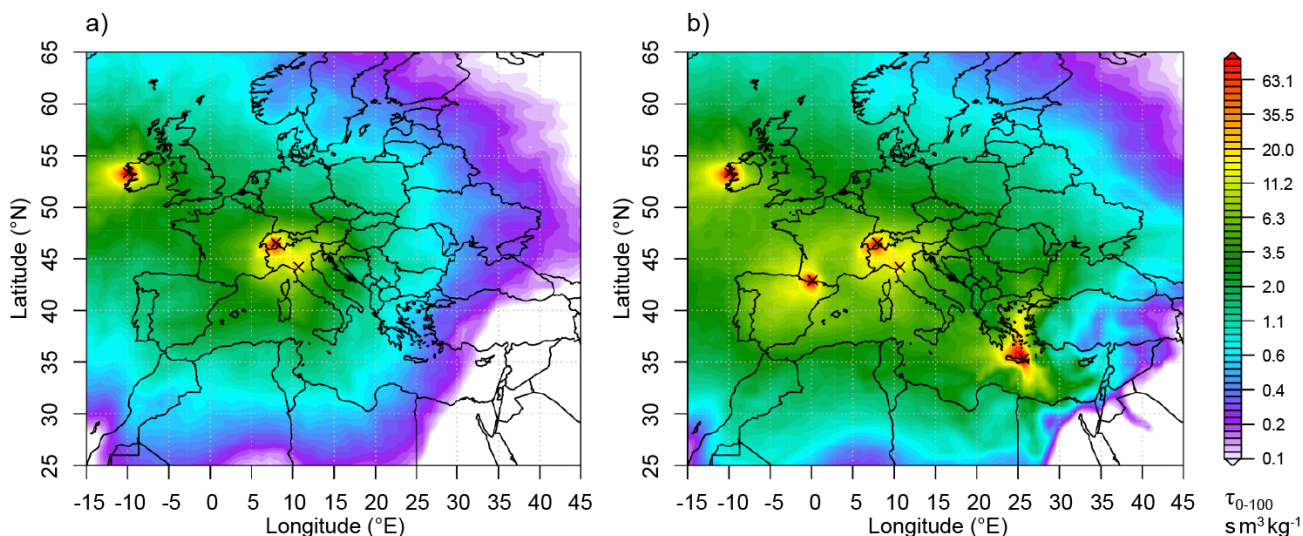


Figure 1.1: Average sensitivity footprint of (a) the existing European AGAGE stations for the time period of both measurement campaigns and (b) for the AGAGE sites combined with the stations at Finokalia and Pic du Midi during the measurement campaigns.

In addition to reported consumption and uses, halocarbons can potentially be released during industrial production, where halocarbons are used as feedstock and intermediate compounds. Within these processes, the use of ODSs is still allowed and due to leakage or incorrect factory practice, non-negligible emissions can occur. In addition, many of these intermediates have never been widely used in consumer products and are therefore not measured regularly in global observation networks. From this vantage point, highly sensitive, state-of-the-art GCMS techniques (see Section 3.1), are an invaluable tool to continuously scan the troposphere for unmonitored halogenated compounds and serve as an early warning system for stakeholders in industry and policy.

In this thesis, all of the above mentioned issues are addressed. We performed an extensive scan of the troposphere, finding a number of unmonitored compounds including ODSs (e.g. HCFC-31), anaesthetics (isoflurane, desflurane and sevoflurane) and fourth generation synthetic halocarbons (HFC-1234yf, HFC-1234ze(E), HCFC-1233zd(E)). I then concentrated on a more detailed analysis of HCFC-31, an ODS regulated by the Montreal Protocol, without any known consumer applications. For the first time an atmospheric budget for HCFC-31 was determined and possible emission sources were identified. Furthermore, the uncovered areas of the AGAGE measurement network towards Southern Europe were addressed by performing two halocarbon measurement campaigns. In the first half year campaign, we sampled Southeastern Europe and adjacent Mediterranean regions in Finokalia (Crete). The second campaign, lasting for 1.5 years, was set up on Pic du Midi (FR), with the aim to survey emissions from the Iberian Peninsula and France. The obtained observations were then used to attribute regional emission sources, using a Lagrangian Particle Dispersion Model (LPDM) and Bayesian inversion methods.

The thesis is structured as follows: In Chapter 2, a scientific background for the performed tasks is given. Chapter 3 provides a detailed discussion about the instrumentation and methods used to scan the atmosphere for unmonitored compounds and the inverse estimation of regional emissions from the obtained measurements during the campaigns. In Chapter 4, HCFC-31 as one of the detected unmonitored substances is analysed in detail. First an atmospheric budget history is determined using measurements from the global AGAGE network and in situ measurements at Empa (Dübendorf, CH), as well as flask samples from around the globe, including Antarctica. In a second part, possible sources of HCFC-31 are addressed. Chapter 5 presents the results of the halocarbon observation campaign from December 2012 - August 2013 in Finokalia (Greece). In combination with continuous observations from the AGAGE sites Jungfraujoch (Switzerland), Mace Head (Ireland) and Monte Cimone (Italy), this allows the first detailed halocarbon emission estimate in Southeastern Europe and gives a first insight into regional halocarbon emissions from adjacent Mediterranean countries such as Greece, Turkey, Egypt, Jordan and Israel. In Chapter 6, we discuss the halocarbon measurements collected during 1.5 years at the Pic du Midi research facility, providing additional insight into emission sources on the Iberian Peninsula and France. All the major findings of this thesis are summarized in Chapter 7 and conclusions are drawn regarding the top-down estimation of halocarbon emissions and the ongoing search for new halocarbons in the atmosphere, providing an early warning system for the industry and decision makers. Additionally this chapter provides an outlook on suggested future research.

Chapter 2 Scientific Background

2.1 General Properties of Halocarbons

Halocarbons (halogenated hydrocarbons) are produced from hydrocarbons, by replacing one or more of the hydrogen atoms by at least one halogen atom. Fluorine and chlorine are the most commonly encountered halogens in halocarbons, but bromine, iodine or combinations of any of these halogens also occur.

The inclusion of halogens in the molecular structure induces polar covalent bonds, which change the physical and chemical properties of the compound significantly, fulfilling many of the industries' requirements. In comparison to hydrocarbons, halocarbons are chemically less reactive, less flammable, and their increased melting and boiling temperatures cause halocarbons often to be liquid at room temperature. These characteristics, among other compound specific advantages, make them the industry's preferred group of compounds for a wide variety of applications such as foam blowing, air conditioning, solvent use, refrigeration, fire extinction, as propellants or as feedstock for the production of polymers [*Midgley and McCulloch, 1999; Carpenter and Reimann, 2014*].

Although halocarbons exist, which have both natural and anthropogenic sources (e.g. methyl bromide (CH_3Br) or methyl chloride (CH_3Cl) [*Rhew, et al., 2000*]), the most abundant halocarbons present in today's atmosphere are solely man-made. These synthetic halocarbons can be classified into four generations (Table 2.1). The chlorofluorocarbons (CFCs) are fully halogenated compounds, containing both chlorine and fluorine, and can only be broken down by highly energetic UV light, only available in the stratosphere. Due to the resulting persistence in the atmosphere and their high GWP, CFCs are strong greenhouse gases. On top of that, along with other species, such as brominated halons, as well as CCl_4 and CH_3CCl_3 , CFCs are strongly ozone-depleting substances (ODSs). Hydrochlorofluorocarbons (HCFCs), considered as transitional replacement compounds for CFCs are structurally similar to their predecessors, despite containing at least one C-H bond. The hydrogen makes HCFCs susceptible for a faster degradation process with hydroxyl radicals (OH) in the troposphere, reducing their lifetime. Therefore most of the halogens carried by HCFCs are prevented from reaching the stratospheric ozone layer. However, HCFCs are still classified as

ODSs and as strong GHGs as well [Farman, 1990; Harris and Wuebbles, 2014]. Hydrofluorocarbons (HFCs), third generation substitutes for CFCs and HCFCs, do not contain anymore chlorine or bromine, thus having effectively no direct destructive effect on the ozone layer (ODP = 0). Nevertheless, HFCs are still potent GHGs and play a non-negligible role in future global warming [Velders, et al., 2009; Velders, et al., 2012]. To avert the radiative effect of HFCs, a fourth generation of synthetic halocarbons (i.e. hydrofluoroolefines, HFOs) with shorter lifetimes and hence lower GWPs have been developed recently. However, their stable degradation products, such as trifluoroacetic acid, could still have negative effects on the environment [Henne, et al., 2012].

Table 2.1: Important representatives of four generations of halogenated compounds.

Industrial Designation	Chemical Formula	Total Lifetime ¹ (years)	100-yr GWP ²	ODP ³
1st Generation Halocarbons				
CFC-11	CCl ₃ F	52	4'660	1.0
CFC-12	CCl ₂ F ₂	102	11'200	0.73
Carbon tetrachloride	CCl ₄	44	1'730	0.72
Halon-1301	CBrF ₃	72	6'290	15.2
Halon-1211	CBrClF ₂	16	1'750	6.9
Halon-2402	CBrF ₂ CBrF ₂	28	1'470	15.7
2nd Generation Halocarbons				
HCFC-22	CHClF ₂	11.9	1'760	0.034
HCFC-141b	CH ₃ CCl ₂ F	9.4	782	0.102
HCFC-142b	CH ₃ CClF ₂	18	1'980	0.057
3rd Generation Halocarbons				
HFC-134a	CH ₂ FCF ₃	9.7	1'300	0
HFC-125	CHF ₂ CF ₃	31	3'170	0
HFC-143a	CH ₃ CF ₃	51	4'800	0
HFC-152a	CH ₃ CHF ₂	1.6	138	0
HFC-23	CHF ₃	228	12'400	0
HFC-32	CH ₂ F ₂	5.4	677	0
HFC-365mfc	CH ₃ CF ₂ CH ₂ CF ₃	8.7	804	0
4th Generation Halocarbons				
HFO-1234yf	CH ₂ CF ₂ CF ₃	10.5 days	<1	0

¹ Total lifetimes from [Carpenter and Reimann, 2014] (except HFO-1234yf from [Myhre, et al., 2013] and CCl₄ from [SPARC, 2016])

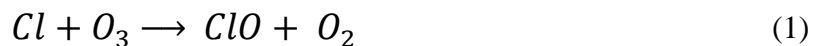
² [Myhre, et al., 2013]

³ ODP represents the relative amount of ozone degradation compared to CFC-11 (ODP=1). Figures from [Harris and Wuebbles, 2014].

2.2 Environmental Impact of Anthropogenic Halocarbons

Replacing refrigerants considered too dangerous for domestic appliances due to their toxicity and flammability (e.g. chloromethane, carbon tetrachloride, isobutane, propane), CFCs became the refrigerant of choice in the early 20th century [Midgley and McCulloch, 1999]. In the 1970s, *Molina and Rowland* [1974] raised first concerns, that CFCs released to the atmosphere would accumulate in the troposphere and be transported to the stratosphere, where they would be able to deplete ozone.

Once migrated to the stratosphere, CFCs are photolysed by highly energetic UV radiation, releasing chlorine radicals. By cycling between Cl and ClO, chlorine atoms are able to trigger a catalytic loss mechanism for stratospheric ozone [Molina and Rowland, 1974; Jacob, 1999].



Molina and Rowland's concerns were justified years later, when *Farman et al.* [1985] discovered a severe thinning of the ozone layer above the Antarctic continent, later becoming famous under the term "ozone hole" [Jones and Shanklin, 1995]. This severe ozone depletion is made possible due to the accumulation of CFC degradation products (HCl, ClONO₂) in the polar vortex and the presence of polar stratospheric clouds (PSCs). PSCs only form under very cold conditions which are consistently encountered over Antarctica during springtime. Due to the heterogeneous reaction site provided by the PSC, the reservoir species HCl or ClONO₂, usually terminating the ozone loss reaction, can be photolytically converted back to ClO and finally chlorine radicals, allowing an uninterrupted destruction of stratospheric ozone as soon as the sun rises over the horizon. The depletion of stratospheric ozone, which was also observed in the Arctic and on a less severe level in the entire global stratosphere [Chipperfield, 1991; Stolarski, et al., 1992; Muller, et al., 1997] increases the amount of harmful UV-B radiation reaching the Earth's surface, causing severe risks for our health and the environment by increasing skin cancer, weakening the human immune system, or damaging crops and natural ecosystems [Molina and Rowland, 1974; Andersen, et al., 2013; Robinson and Erickson, 2015]. Additionally, it was recognized, that CFCs and HCFCs are highly efficient in absorbing infrared radiation, leading to a significant impact on global climate when accumulating in the atmosphere [Ramanathan, 1975; Hodnebrog, et al., 2013].

As a consequence of the discovery of the ozone hole, caused by CFCs and related compounds (e.g. halons, brominated species), the Montreal Protocol was established in 1987 and entered into force in 1989, developing the framework to phase-out the production and consumption of CFCs for emissive uses on a global level. This fostered the development of non-ozone depleting HFCs, which, however, like their predecessors (e.g. CFCs, HCFCs, halons) may still be strong greenhouse gases.

Greenhouse gases (GHGs) are defined as gases that absorb in the wavelength range where most of the infrared terrestrial radiation is emitted (5-50 μm). Thereby the internal energy level (vibrational and rotational transition) of the gas molecule is increased, allowing the molecule to re-emit longwave radiation. A common metric to define the impact of a greenhouse gas on the Earth's climate is the greenhouse warming potential, which combines the gases radiative efficiency (the ability of the molecule to absorb radiation) and its lifetime, usually expressed as GWP integrated over a time horizon of 100 years (GWP-100) [Hodnebrog, *et al.*, 2013]. To a large part halocarbons are very effective GHGs, because they absorb outgoing infrared radiation in a spectral range, where CO_2 and water vapour only absorb weakly. This range between 8 and 13 μm , is referred to as “atmospheric window”, which is of great importance for the definition of the global surface temperature in the unperturbed state [Jacob, 1999; IPCC/TEAP, 2005; Hodnebrog, *et al.*, 2013; Myhre, *et al.*, 2013]. Although the Montreal Protocol was able to reduce the accumulation of CFCs and HCFCs in the atmosphere, averting a possibly strong impact on the future global climate, the replacement and growing need of these compounds with ozone safe HFCs, including direct and future emissions from banks, could have a significant impact on the future radiative forcing [Velders, *et al.*, 2009; Miller and Kuijpers, 2011; Velders, *et al.*, 2014]. To avoid growing climatic implications based on CFC substitutes, shorter lived HFCs are developed. However, although the effect on global climate becomes small, the faster break-down process and wash-out can result in more localized accumulations of degradation products, which may be environmentally toxic. An example is HFC-1234yf, discussed as a short lived replacement for the commonly used HFC-134a in mobile applications. HFC-1234yf is broken down to trifluoroacetic acid (TFA), a mild phytotoxin which is able to accumulate in Earth's hydrosphere [Henne, *et al.*, 2012].

2.3 Regulatory Treaties for Halocarbons

With the growing acceptance of the Molina-Rowland theory and the evident observation of an adverse effect of CFCs on the ozone layer over Antarctica, the Montreal Protocol was signed in 1987 and entered into force on the 1. January of 1989 [Braathen, *et al.*, 2012; Andersen, *et al.*, 2013]. The reduction mechanism of the Montreal Protocol is based on clearly defined phase out schedules for

each group of compounds, separately specified for developed (non-Article 5) and developing (Article 5) countries. A complete ban of CFCs was due in 1996 in non-Article 5 and 2010 in Article 5 countries, respectively. The phase out of the less harmful HCFCs is less stringent and only began in 1996 in non-Article 5 countries, whereas the freeze and subsequent reduction just went into force in 2013 in Article-5 countries. After step-wise reduction over ~20 years, a complete phase out for this compound group is planned for 2030 and 2040 for developed and developing countries, respectively. The original treaty and the following amendments have been ratified by 197 nations and became the first treaty in the history of the United Nations to achieve universal ratification [UNEP, 2016].

As a consequence of the control of ODSs under the Montreal Protocol, observations of anthropogenic chlorine and bromine mole fractions in the troposphere and stratosphere are decreasing. Assuming full compliance with the Montreal Protocol, the ozone layer is expected to recover in coming decades and healing of the Antarctic ozone hole is emerging [World Meteorological Organization (WMO), 2014; Solomon, *et al.*, 2016]. As suggested from modelling studies, the Montreal Protocol not only avoided a major destruction of the ozone layer until mid-century [Newman, *et al.*, 2009], but had an additional benefit for the global climate by rapidly reducing the emission of very potent greenhouse gases into the Earth's atmosphere. The avoided annual emissions are estimated to 10 Gt CO₂eq, corresponding to about five times the annual reduction target of the Kyoto Protocol for 2008-2012 [Velders, *et al.*, 2007; Velders, *et al.*, 2012].

Due to their sometimes large GWPs, HFCs, used almost exclusively as alternatives to ODSs, are included in the greenhouse gases regulated by the 1997 Kyoto Protocol. The aim of this international treaty is to counteract global warming by legally binding participating developed countries (referred to as Annex-1 countries) to emission reduction targets of a “basket” of greenhouse gases (e.g. CO₂, CH₄, N₂O, HFCs, some PFCs, SF₆). Unlike the Montreal Protocol, the second commitment period agreed on in 2012 (known as Doha Amendment to the Kyoto Protocol) was only ratified by 71 countries as of October 2016, with large GHG emitters such as the United States not being part of it [UNFCCC, 2016b]. In comparison to the highly successful Montreal Protocol, emission directives are not specified on the level of individual compounds, but market-based mechanisms can be used as an additional tool to meet national reduction targets. This means that emission-reduction projects implemented by Annex-1 parties in developing countries can earn certified emission reduction credits, counting towards meeting Kyoto targets for the respective Annex-1 party.

All Annex-1 parties have to annually report statistically estimated emissions (so called bottom-up emission estimates) to the United Nations Framework Convention on Climate Change (UNFCCC).

Although these emission figures are publicly available, it is suspected that intentional underreporting could take place [Nisbet and Weiss, 2010].

Because HFC projections in business-as-usual scenarios show a large contribution to future climate forcing, a phase-down would have immediate effects for climate change mitigation due to the relatively high GWPs and short atmospheric lifetimes of these substances (in comparison to CO₂). Furthermore, a more stringent regulation of HFCs, which can be viewed as a side-effect of the Montreal Protocol, could avoid the build-up of HFC banks in e.g. air conditioners, which could have negative long-term effects on global climate upon later release to the atmosphere. Therefore, in October 2016, HFCs were included into the Montreal Protocol with varying schemes to effect a phase-down of the consumption to 15% of the original value. Industrial countries will start first and have a deadline until 2036 to reach this goal, whereas the phase-down of developing countries is planned between 2045 and 2047 (Figure 2.1). Although the Kyoto Protocol controls the emissions of HFCs in a basket of gases, the Montreal Protocol will be able to regulate production and consumption, allowing preservation of the Montreal Protocol's climate benefit [Velders, *et al.*, 2009; Velders, *et al.*, 2012; Andersen, *et al.*, 2013; Velders, *et al.*, 2014].

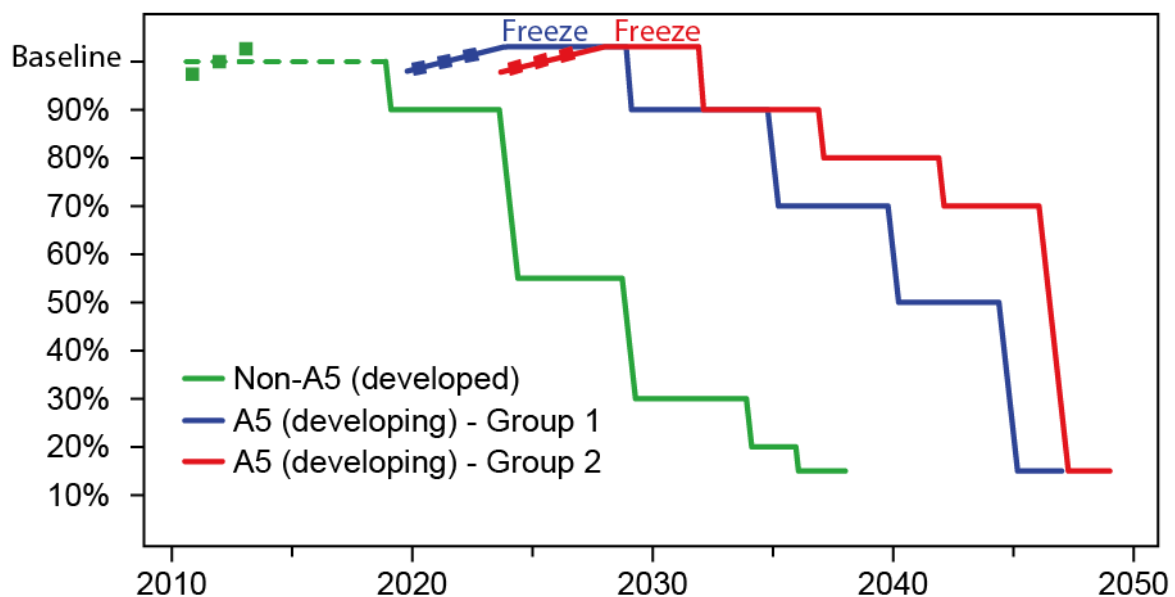


Figure 2.1: Phase-down scheme for HFCs according to the 2016 Kigali Amendment to the Montreal Protocol. Dotted lines show the period which is used to define baseline figures for the respective groups of countries.

2.4 Observations of Atmospheric Halocarbons

Due to their potential to severely damage the ozone layer and their strong impact on global climate, the monitoring of CFCs and their substitute compounds (e.g. HCFCs, HFCs) has been essential. The introduction of the electron capture detector (ECD) in the 1970's [Lovelock, 1974; Lovelock and Watson, 1978] facilitated continuous measurements of the low abundance CFCs. Based on this development, the first in situ global observation network became operational in 1978 within the Atmospheric Lifetime Experiment (ALE). It provided 4 daily measurements at 5 globally distributed observation sites (Adrigole (Ireland), Cape Meares (USA), Ragged Point (Barbados), Point Matatula (American Samoa) and Cape Grim (Tasmania)), which were chosen to ensure sampling of background levels in clean oceanic air [Prinn, *et al.*, 1983]. This pioneering project was succeeded by the Global Atmospheric Gases Experiment (GAGE, 1981-1985) and the Advanced Global Atmospheric Gases Experiment (AGAGE) which is operational to this day. Under the auspices of AGAGE, 12 coastal and mountainous stations provide observations of a comprehensive set of halogenated compounds at high frequency (~ 24 observations per day) [Prinn, *et al.*, 2000]. Additional continuous observations of ODSs are performed by the NOAA/GMD network [NOAA-ESRL, 2016b] (Figure 2.2). These temporally high-resolution measurements are complemented by a variety of periodic ground- and aircraft-based flask samples from around the globe (e.g. Antarctica [Vollmer, *et al.*, 2011], Greenland [NOAA-ESRL, 2016a] or the metropolitan area of Los Angeles [Barletta, *et al.*, 2011]), while satellite measurements of CFCs might be a first step towards future monitoring of halocarbon abundances distributed over the atmospheric column [Eckert, *et al.*, 2016].

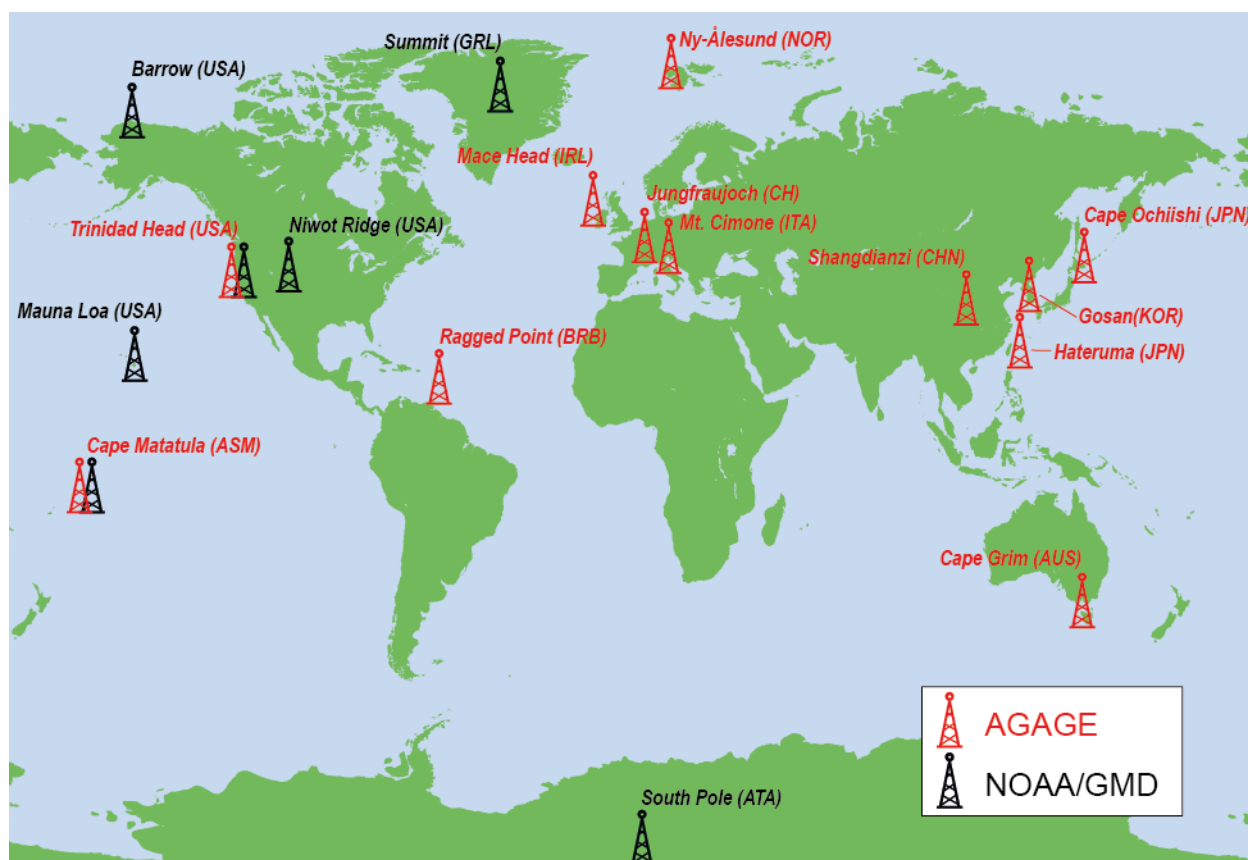


Figure 2.2: Global distribution of AGAGE and NOAA/GMD observation sites for halocarbons.

Europe is currently represented by 3 AGAGE observation sites, Ny-Alesund (Norway), Jungfraujoch (Switzerland), Mace Head (Ireland) and Monte Cimone (Italy) as an affiliated site. Mace Head is a coastal site, situated on the western coast of Ireland. It is mostly influenced by clean air advected from the Atlantic Ocean, representing background mole fractions, but frequently sees polluted air masses from the European continent. Although the occurrence of pollution events is more seldom, similar characteristics apply to the observation site at Ny-Alesund, located at the coast of Svalbard, above the Arctic Circle. Jungfraujoch and Monte Cimone are high alpine sites, located in the Swiss Alps at an elevation of 3580 m a.s.l. and in the Apennines in Northern Italy at 2160 m a.s.l., respectively. High altitude stations are typically influenced by free tropospheric air, representing background concentrations, but occasionally are able to observe polluted air masses from the European atmospheric boundary layer under favourable meteorological conditions. Although Ny-Alesund is not close enough to any emission sources, the other 3 AGAGE sites, are influenced frequently enough by anthropogenic emissions to provide satisfactory coverage of Western European emission sources [Henne, *et al.*, 2010]. However, despite existing campaign data for Eastern Europe [Keller, *et al.*, 2012], this network leaves Eastern Europe and the Mediterranean region (e.g. Spain, Portugal, Greece) as outstanding white spots on the map (Figure 1.1).

2.5 Atmospheric Transport Models and Emission Estimation

Global networks of measurement stations measuring halogenated species on a quasi-continuous basis provide an invaluable insight into the abundance and trends of these compounds in the troposphere over the years. However, international agreements such as the Montreal and Kyoto Protocol, rely on statistical bottom-up emission inventories, reported by individual countries. Therefore, the independent validation of spatially resolved national inventory data on the emission level is increasingly in demand to check compliance with those international treaties.

To establish a connection between atmospheric mole fractions measured at a receptor site, y , and trace gas fluxes to and from the atmosphere, x , a transport and chemistry model is required that can describe the relevant atmospheric processes.

Between the emission at a source location and the measurement at a receptor site, chemical pollutants undergo several processes in the atmosphere. They are transported, stirred and mixed, causing an initial pollution cloud to be dispersed and diluted. Depending on their molecular properties, the pollutants undergo chemical transformation and may be depleted, and are finally removed from the atmosphere by a deposition process [Haynes, 2005]. To simulate an accurate response at the receptor to a pollution pulse from an emission source, the adequate description of these mechanisms is essential.

In general two principles of atmospheric tracer modelling can be differentiated. Eulerian models are based on a fixed model grid, observing the properties of a pollutant as a function of time and space. Using the Lagrangian perspective, infinitesimally small air parcels (also referred to as particles) are observed by following them along with the mean flow, providing details about their location and properties at any time. The Eulerian approach implies instantaneous mixing within a grid cell, whereas the Lagrangian models are independent of a computational grid and therefore in principle allow for high resolution results, given a sufficiently large number of model particles. The main advantage of the Lagrangian approach however is, that no numerical diffusion is involved [Stohl, *et al.*, 2005], allowing the transport of atmospheric features with steep gradients, such as a pollution plume originating from a point source. Lagrangian models can also easily be inverted in time to enable an efficient determination of a measurement's sensitivity to upwind sources, which is considerably more complicated in the Eulerian framework and requires the development of an adjoint model.

As a consequence the Lagrangian perspective and more recently especially Lagrangian Particle Dispersion Models (LPDMs) have become particularly attractive in the field of source attribution.

In earlier approaches, halocarbon observations have been qualitatively attributed to their relevant source regions. Either with single-trajectory models (neglecting dispersion) for strong pollution events [Reimann, *et al.*, 2004; Stemmler, *et al.*, 2007; Reimann, *et al.*, 2008] or with more elaborate methods based on larger numbers of observations and trajectories, allocating emissions based on the trajectories' residence times within predefined grid cells, often referred to as "trajectory statistics" [Ashbaugh, *et al.*, 1985; Stohl, 1996; Scheifinger and Kaiser, 2007]. However, a quantitative source attribution is a more challenging task. One concept involves the inclusion of tracer compounds with well-known emission sources (tracer-ratio method) in the trajectory statistics approach [Reimann, *et al.*, 2005], but due to the unresolved subgrid-scale transport and mixing characteristics in the latter, LPDMs have gradually replaced trajectories to establish a quantitative relationship between sources and receptors [Seibert and Frank, 2004; Brunner, *et al.*, 2012b].

In general, one can write down the atmospheric model of concentrations as being a multi-dimensional function of surface fluxes, x , (and others) providing output variables y

$$y = G(x, \dots). \quad (4)$$

If all other influence factors are held constant, the change of atmospheric mole fractions, y , due to changes in trace gas fluxes, x , can be written as

$$dy = \frac{dG}{dx} dx, \quad (5)$$

where $\frac{dG}{dx}$ is the Jacobian matrix of first order derivatives of G . Deriving $\frac{dG}{dx}$ from a complex atmospheric transport and chemistry model is computationally very extensive and/or requires an adjoint version of the model. With the forward model one would analyse the Jacobian in a certain neighbourhood, x_0 , in which case the simulated mole fractions can be rewritten as

$$y = \left. \frac{dG}{dx} \right|_{x=x_0} (x - x_0) + G(x_0). \quad (6)$$

If the simulated mole fractions only depend linearly on the surface fluxes, $\frac{dG}{dx}$ becomes a matrix of constant values, M . If, in addition, $G(x_0 = 0) = 0$, meaning that there is no source of y other than surface fluxes x , equation 6 simplifies to

$$y = Mx \quad (7)$$

The above conditions can usually be assumed for greenhouse gases in the atmosphere that either undergo no atmospheric degradation (CO_2) or only (pseudo) first order decay chemistry (CH_4 , N_2O , halocarbons).

In this thesis two kinds of atmospheric models were used to derive M and subsequently optimise x , so that the simulated mole fractions, y , match the observations (Section 3.4). The first is a simplified transport and chemistry model of the global atmosphere, consisting of 12 boxes dividing the atmosphere into four equal-mass latitudinal boxes and three vertical layers. The model calculates transport between the boxes by parameterizing eddy diffusion and bulk advection, while compound losses are based on simple parametrizations of photolysis, OH oxidation (using a fixed OH field) and oceanic uptake (see Section 4.2). The second is a Lagrangian particle dispersion model (LPDM) applied in receptor-oriented, time-inverted mode to directly estimate M for regional emission contributions, which is further described in Section 3.3.

Chapter 3 Methods

3.1 Instrumentation

The detection and quantification of the analysed halogenated carbons presented in this thesis is challenging, due to their wide variety of volatilities and very low tropospheric abundances on a scale of parts per trillion (ppt, 10^{-12}), typically. To ensure high-precision measurements and improve the signal-to-noise ratio of such small mole fractions, it is common today to preconcentrate large volumes (~2L) of air, which are transferred to a coupled gas chromatography - mass spectrometry (GC-MS) system.

Two generations of preconcentration systems were used. For the remote campaigns in Finokalia (Greece) and on Pic du Midi (France), the adsorption-desorption system (ADS) was used. The ADS is a custom-built, automated preconcentration unit coupled to a GC-MS, developed in the 1990's by the University of Bristol and has since been used for the estimation of global emissions [e.g. *O'Doherty, et al.*, 2004; *Greally, et al.*, 2007; *Reimann, et al.*, 2008] and for regional measurement campaigns [e.g. *Keller, et al.*, 2012]. During the preconcentration phase a three-step adsorbent filled microtrap is cooled to -50°C by thermoelectric Peltier devices over a period of 40 min. For desorption, the trap is resistively heated to $\sim 220^{\circ}\text{C}$, and the trapped sample is transferred to the GC (Agilent 6890) and MS (Agilent 5973) using helium as carrier gas [*Simmonds, et al.*, 1995]. The instrument is designed to operate autonomously, providing air- or standard-observations on a 2 hourly basis. Due to its simple and robust construction, the ADS is suitable for automated remote halocarbon measurements involving air- or land-based transport of the instrument to the place of its use. However compared to its successor (Medusa), a smaller number of compounds can be measured using ADS technology and the detection limits are higher.

The “Medusa” is a further development of the ADS, based on the same principle of analysing larger, preconcentrated air samples on a GC-MS. The preconcentration process of the “Medusa” includes two HayeSep D filled cold-traps as shown schematically in Figure 3.1. During preconcentration, the traps are cooled to temperatures of -165°C using a low-temperature refrigeration unit. Unlike the ADS, species with different volatilities are transferred separately to the second cold-trap

where they are refocused before being transferred to the GC-MS. This method avoids interferences on the MS and extends the analytical range to species with lower volatility, while still maintaining the capability to measure compounds with higher boiling points [Miller, *et al.*, 2008]. The Medusa not only enhances the number of detectable compounds, but also increases measurement precision and allows a temporal sampling resolution of ~ 70 min. It is currently the standard instrument at the AGAGE observation sites (except at the affiliated site Mt. Cimone), from which the data were used to complement the campaign data for the inversions. It is also used at the Empa Laboratory for the detection of unmonitored low abundance halocarbons [Schoenenberger, *et al.*, 2015; Vollmer, *et al.*, 2015a; Vollmer, *et al.*, 2015b; Vollmer, *et al.*, 2015c].

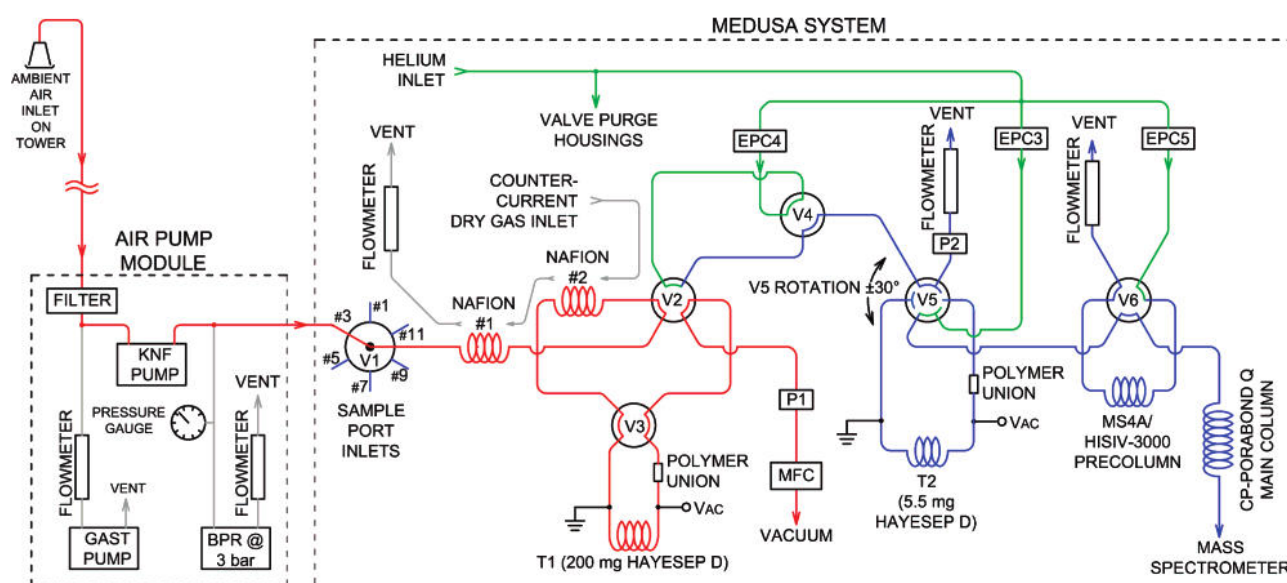


Figure 3.1: Schematic flow scheme of Medusa pre-concentration unit (from Miller, *et al.* [2008]).

Whether with the ADS or the Medusa, calibration of measurements is crucial. For this, reference standards are usually sampled alternating with air samples to detect and correct for drift in detector sensitivity. Because all standards are referenced to the same scale within the AGAGE project (those of the Scripps Institution of Oceanography (SIO), University of Bristol, or Empa), they also guarantee, that observations of all stations withing the AGAGE network are intercomparable.

3.2 Empa-2013 Primary Standard Preparation and Halocarbon Identification

The primary calibration scale, used for the calibration of the compounds analysed within the scope of the search for unmonitored substances in the troposphere is based on two different gas mixtures. One is a gravimetrically prepared, commercially obtained reference gas mixture (HCP-04Carba, Carbagas, Switzerland), containing several compounds with mole fractions in the 10 ppm (parts-

per-million, 10^{-6}) range. This gas mixture also contains HCFC-31, which is analysed in more detail as part of this thesis. The second one is a custom-made high-concentration standard (HCP-002).

The preparation of our custom-made primary standard follows a multi-step process, using the setup shown schematically in Figure 3.2. In a first step, we clean the compounds from impurities such as oxygen (O_2) or nitrogen (N_2) by distillation thereby taking advantage of the generally lower boiling point of these impurities compared to the analysed species. The cylinder containing the target compound is cooled by submerging it into liquid nitrogen. At such temperatures, the target compound becomes solid, whereas O_2 and N_2 remain in the liquid or gaseous phase. The cylinder is then warmed-up again to transform the sample back into liquid or gaseous form, using a water bath. During this process, the headspace of the cylinder is pumped away, removing available impurities. This process is repeated until the vapour pressure within the target compound cylinder is similar to values given in the literature, confirming the purity of our target compound.

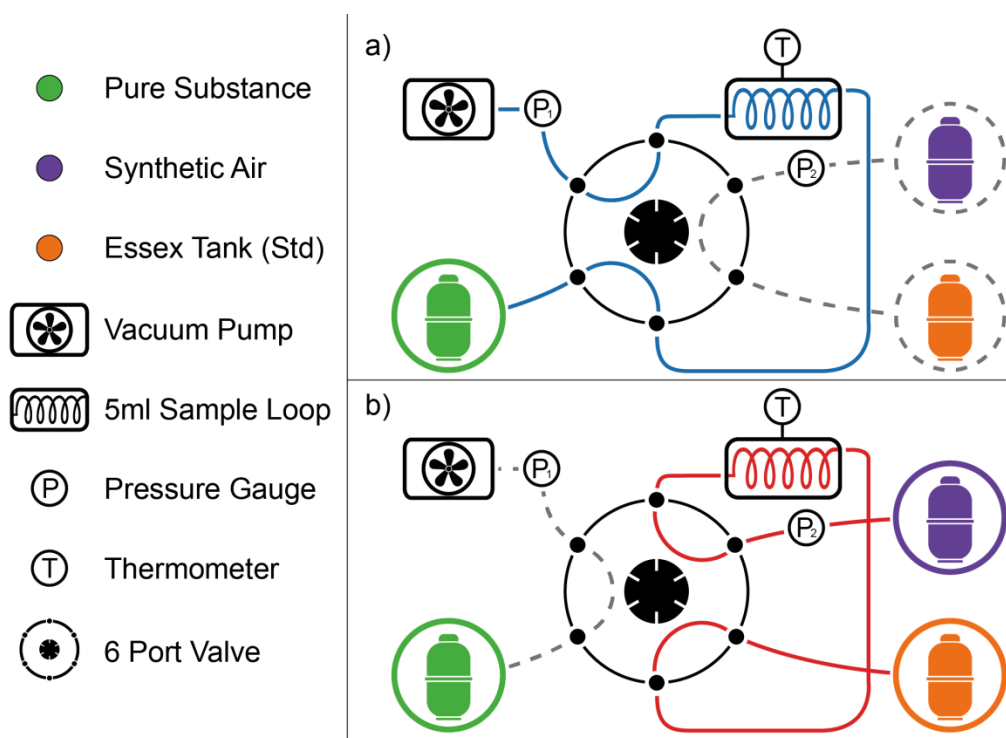


Figure 3.2: Schematic illustration of the Empa-2013 primary calibration standard preparation setup.

In a second step, termed “loading phase” (Figure 3.2a), sample loop aliquots are transferred to the target cylinder. After evacuating and flushing the sample loop with the target compound three times, the 5 ml sample loop is filled with the pure compound to a desired pressure. For some compounds with low vapor pressure, multiple injections are necessary.

During the third step, the 6 port valve of the system is set to the “injection position” (Figure 3.2b), flushing the content of the sample loop into the target tank, using synthetic air.

Both standards are subsequently merged and diluted from ppm to final near-two ppt (parts-per-trillion 10^{-12}) levels (EP-001), applying a multi-step pressure-based dilution. For this, synthetic air was used, which was previously purified following an elaborate clean-up technique using custom-made clean-up cartridges [Vollmer, *et al.*, 2015b]. To cross check the accuracy of the dilution, both standards include additional “boot-strap” compounds, for which we have independent primary calibrations. The bootstrap gases contained in “HCP-04Carba” are CFC-12 (CCl_2F_2), SF_6 , which were referenced to the SIO-05 scale [Prinn, *et al.*, 2000; Vollmer and Weiss, 2002] and methane (CH_4) which was measured using a “Picarro Analyzer” against a calibration scale of the National Oceanic and Atmospheric Administration (NOAA). “HCP-002” only includes methane, which was also used to check the quality of the injection process. These “boot-strap” gases are abundant in the high-concentration mixtures at elevated mole fractions, in order to reach near ambient concentrations in the intermediate (methane) and final dilutions (CFC-12, SF_6). The resulting filling EP-001 defines the “Empa-2013 primary calibration scale”. Measured mole fractions of CFC-12 and SF_6 were smaller by about 5% compared to the predicted mole fractions based on the sample loop injections and subsequent pressure-based dilutions. This was expected due to the expansion of the canisters upon pressurizing. Consequently, a correction was applied for the final mole fraction assignment in EP-001. EP-001 was used in the following to calibrate whole air secondary standards (E-094 and E-108), which were used to analyse flasks. The in-situ measurements were measured against lower-level whole air standards (quaternaries), which were regularly compared against these secondaries. Secondary and quaternary standards were spiked with some of the new compounds to achieve better signal strength, allowing for a better tracking of the MS sensitivities.

To identify the new compounds on our system and determine the retention times and target mass-over-charge (m/z) ratios for the following quantitative analysis, a diluted aliquot of the high concentration reference mixtures (HCP-04Carba and HCP-002) was measured on the GCMS in scan mode over an m/z range from 49-200. The resulting spectra were compared with published data, when available, to identify the respective compounds based on the intensity order of the fragments. For compounds with no published spectra, the masses for potential fragments of the full molecules were compared to the measured spectra. This allowed for full and unique identification of all compounds. For the quantitative analysis of samples on the GCMS in selective-ion mode, the respective target ion (T in units m/z), which is used for quantification and the qualifier ions (Qs in units m/z), were

chosen based on their intensity on our system, preferring higher ranked ions but trying to avoid possible interferences particularly for ubiquitous mass fragments such as CF_3^+ .

3.3 Lagrangian Particle Dispersion Model (FLEXPART)

For the derivation of source sensitivities, providing a direct relationship of a mass emission from a source location with the measured mole fraction at a receptor site, we used the Lagrangian particle dispersion model (LPDM) FLEXPART [Stohl, *et al.*, 2005]. FLEXPART is tailored to simulated long-range and mesoscale transport of trace compounds in the atmosphere. It has been extensively validated against data from long-range tracer studies [Stohl, *et al.*, 1998; Stohl and Trickl, 2001] and has been successfully employed in many recent halocarbon source allocation studies involving the same receptor sites or receptor sites with similar characteristics as the ones used during this thesis [Stohl, *et al.*, 2009; Vollmer, *et al.*, 2009; Stohl, *et al.*, 2010; Keller, *et al.*, 2011; Keller, *et al.*, 2012; Fang, *et al.*, 2014; Fang, *et al.*, 2015].

FLEXPART is an offline model that requires input from a three-dimensional meteorological model. This includes information on the horizontal and vertical wind, temperature, specific humidity, and surface fluxes of momentum and heat. In this study, we drive the transport model with meteorological fields from the operational analysis/forecast of the Integrated Forecast System (IFS) of the European Centre for Medium-Range Weather Forecasts (ECMWF). These fields were obtained on a 3-hourly basis, with a global resolution of 1° by 1° and a finer resolution 0.2° by 0.2° nested domain for the Alpine area. For dates later than June 2013 the model features 137 vertical model levels and 91 before then.

The transport of tracer material is simulated by calculating the trajectories of a large ensemble of infinitesimally small air parcels (also referred to as particles). These particles are advected based on the combination of the grid-resolved mean wind, superimposed by turbulent and mesoscale wind fluctuations, according to

$$\mathbf{X}(t + \Delta t) = \mathbf{X}(t) + \mathbf{v}(\mathbf{X}, t)\Delta t \quad (8)$$

where \mathbf{X} describes the position vector of the air parcel, t represents the time and Δt is the time increment used in the model. The wind vector \mathbf{v} is defined as

$$\mathbf{v} = \bar{\mathbf{v}} + \mathbf{v}_m + \mathbf{v}_t \quad (9)$$

with the grid scale wind vector $\bar{\mathbf{v}}$ and the mesoscale and turbulent wind fluctuations \mathbf{v}_m and \mathbf{v}_t , respectively. Mesoscale motions \mathbf{v}_m are approximated by the assumption, that information on the

sub-grid mesoscale wind variance can be related to grid-scale variance of the wind at every grid point. To parameterize turbulent motions \mathbf{v}_t , FLEXPART assumes the stochastic disturbance of an air parcel to be Gaussian. This assumption can be violated under convective conditions but is expected to cause minor errors, especially at sufficiently large transport distances, where particles are well-mixed within the whole planetary boundary layer (PBL). Using this assumption, the vertical wind component w can be described with the Langevin equation in the form

$$dw = -w \frac{dt}{\tau_{Lw}} + \frac{\partial \sigma_w^2}{\partial z} dt + \frac{\sigma_w^2}{\rho} \frac{\partial \rho}{\partial z} dt + \left(\frac{2}{\tau_{Lw}} \right)^{\frac{1}{2}} \sigma_w dW \quad (10)$$

with σ_w denoting the standard deviation of the turbulent vertical turbulent component and τ_{Lw} representing the Lagrangian autocorrelation timescale of the vertical velocity. Both of these parameters are specifically derived for the specific atmospheric stability conditions following the similarity suggestions by *Hanna* [1982] and are based on boundary layer parameters (e.g. the PBL height h_{mix} , the friction velocity, u_* , and the Monin-Obhukov length, L_M). The first term on the right-hand side describes the autocorrelated part of the turbulence. The second and third terms are the drift and density correction with ρ denoting the air density. These corrections are necessary to fulfill the well-mixed condition of particles and avoid accumulation of particles in or dissipation from certain areas of the flow with different turbulence intensity and atmospheric density. The fourth term describes a random component with dW being increments drawn randomly from a Gaussian distribution of mean zero and standard deviation 1 [*Stohl, et al.*, 2005].

PBL heights, another essential parameter of an LPDM, are diagnosed using a bulk Richardson concept, by setting the PBL height h_{mix} to the first model level for which the bulk Richardson number as defined by *Vogelezang and Holtslag* [1996] exceeds a threshold of 0.25. Other important mechanisms parameterized in FLEXPART include a moist convection scheme, simulating the vertical mass exchange in convective clouds (updrafts/downdrafts), as well as removal processes such as radioactive decay, dry- and wet deposition. A more detailed description of the model can be found in *Stohl et al.* [2005].

One of the major advantages of LPDMs is that they are essentially “self-adjoint”, providing the possibility to track the dispersion backwards in time using the identical model formulation as used in the forward model. Getting the time inverted model in the Eulerian framework however is a much more challenging and computationally demanding task [*Seibert and Frank*, 2004; *Brunner, et al.*, 2012b]. In our studies presented in Chapter 5 and Chapter 6, FLEXPART was therefore run in a

receptor-oriented backward mode, by releasing 50'000 particles at each 3-hourly interval from the receptor sites and following them backward in time for 10 days. The output generated by FLEXPART is the summed particle residence time $\tau_{i,j}$ in a grid cell i,j , within a layer of sampling height h . Assuming that pollutants are predominantly emitted from ground level into the lowest layer, h is defined as the layer between 0 - 100 m, the latter also being the minimal PBL height used in the model. The horizontal distribution of this estimated residence time is usually referred to as “footprint”. Division of the residence time $\tau_{i,j}$ by the air density in the respective grid box i,j and the molar weight ratio R_m of the pollutant compound and dry air

$$R_m = \frac{\mu_{dry-air}}{\mu_{pollutant}} \quad (11)$$

results in the source-receptor-relationship (SRR) $s_{i,j}$ in units of $s \, m^3 \, kg^{-1} \, mol \, mol^{-1}$ (Equation 12). The SRR describes the influence of an emission source of unit strength ($1 \, kg \, s^{-1}$) in the grid box i,j with Volume V , on the measured mole fraction χ at the receptor and is proportional to the average residence time $\tau_{i,j}$ for tracers with negligible loss in the atmosphere on the timescale of the LPDM.

$$s_{i,j} = \frac{\tau_{i,j}}{\rho_{i,j}} R_m \quad (12)$$

The sum of the product of the SRR and the emission field, providing emissions $E_{i,j}$ in units of $kg \, s^{-1}$ and accounting for the source grid box volume $V_{i,j}$, then yields the increase in mole fraction at the receptor

$$\chi_p = \sum_{i,j} \frac{s_{i,j} E_{i,j}}{V_{i,j}} \quad (13)$$

3.4 Atmospheric Bayesian Inversion

For the quantitative assessment of trace gas fluxes to and from the atmosphere, the information derived from the transport model has to be combined with the observed mole fractions in a specialised field of data assimilation referred to as inverse modelling.

Thereby, unknown variables in the so-called state vector are adjusted to optimize the match between the simulated and the observed mixing ratios. Because in our regional-scale approach the LPDM explains only emissions within the period of the backward simulation and from a spatially limited domain, the state-vector contains the gridded emissions as well as additional parameters characterizing the baseline mole fractions at the termination point of the LPDM back-trajectories,

which together with recent emissions add up to the measured mole fraction at the observation site. In inverse atmospheric flux estimation, the observations often don't contain sufficient independent information to unambiguously constrain the surface fluxes. To further constrain the model, a priori estimates of the state-vector variables are introduced, where prior emission estimates are based on emission inventories and subjective expert judgement, whereas baseline mixing ratios can be deduced using observation-based methods.

In the ‘‘Bayesian Inversion’’ approach, a frequently applied framework to estimate emissions of trace gases, the probability density functions (pdf) of the a priori information and the observations, which are based on a specified degree of uncertainty, are used to facilitate the estimation of an optimal solution and subsequently derive the pdf of the optimized a posteriori state vector.

The basis for the concept of the ‘‘Bayesian Inversion’’ is given by the theorem of Bayes, which allows the determination of $P(x|c)$, the probability density for the parameter values x , conditional on the true, observed values of c , provided that $P(c|x)$, the conditional probability of c for a given value of x , can be determined [Enting, 2002]:

$$P(x|c) = \frac{P(c|x) P(x)}{P(c)} \quad (14)$$

$P(c)$ and $P(x)$ provide the unconditional probability density of c and x .

If we define the parameters according to our inversion problem, with x being the state vector, containing the variables to be estimated (e.g. emission fluxes) and c being the observed mole fractions, the most probable solution of x with respect to c can be obtained by minimizing the cost function J , which, under the assumption of Gaussian distributed uncertainties takes the form of [Enting, 2002; Thompson and Stohl, 2014]

$$J = \frac{1}{2} (\mathbf{M}\mathbf{x}_{post} - \mathbf{y}_{obs})^T \mathbf{C}_{obs}^{-1} (\mathbf{M}\mathbf{x}_{post} - \mathbf{y}_{obs}) + \frac{1}{2} (\mathbf{x}_{post} - \mathbf{x}_{prior})^T \mathbf{C}_{prior}^{-1} (\mathbf{x}_{post} - \mathbf{x}_{prior}). \quad (15)$$

In Equation 15, differences between the simulated and the observed mole fractions $\mathbf{M}\mathbf{x}_{post}$ and \mathbf{y}_{obs} and deviations of the optimised state vector \mathbf{x}_{post} from the prior state vector \mathbf{x}_{prior} (which includes information about a priori emissions and the a priori baseline mole fractions) are penalized, weighted by the inverse of the respective uncertainty covariances. \mathbf{C}_{prior} is the uncertainty covariance matrix of the a priori uncertainties and \mathbf{C}_{obs} is the covariance matrix of the observation-model

mismatch, corresponding to the uncertainties of the observations and the transport model. The structure of these covariance matrices is further outlined in Section 5.2.7. \mathbf{M} is the sensitivity matrix mapping the emissions onto the observations, denoting the dependence on the emissions, which, in the case of the regional-scale inversion applied here, is the SRR as derived from FLEXPART and the baseline mole fractions, respectively.

Minimizing J yields a linear system of equations for the posterior state [Enting, 2002]

$$\mathbf{x}_{post} = \mathbf{x}_{prior} + (\mathbf{C}_{prior}\mathbf{M}^T\mathbf{M}\mathbf{C}_{prior}\mathbf{M}^T + \mathbf{C}_{obs})^{-1}(\mathbf{y}_{obs} - \mathbf{M}\mathbf{x}_{prior}) \quad (16)$$

as used in Chapter 5 and Chapter 6 of this thesis. The main numerical effort is solving the inverse of the matrix $\mathbf{S} = \mathbf{C}_{prior}\mathbf{M}^T\mathbf{M}\mathbf{C}_{prior}\mathbf{M}^T + \mathbf{C}_{obs}$, which is a $n \times n$ matrix, with n being the number of observations. Once \mathbf{S}^{-1} and \mathbf{x}_{post} are established also the covariance of the a posteriori state can be calculated

$$\mathbf{C}_{post} = \mathbf{C}_{prior} - \mathbf{C}_{prior}\mathbf{M}^T\mathbf{S}^{-1}\mathbf{M}\mathbf{C}_{prior}. \quad (17)$$

If any useful information is contained in the observations and the sensitivity matrix, the a posteriori covariances should be smaller than the a priori covariances. The reduction of uncertainty in the state variables is often expressed as a percentage reduction

$$r = \left(1 - \frac{\text{diag}(\mathbf{C}_{post})}{\text{diag}(\mathbf{C}_{prior})}\right) 100\% \quad (18)$$

where $\text{diag}()$ extracts the elements in the diagonal of the covariance matrices. Finally, the information contained in \mathbf{C}_{post} can be used to calculate the a posteriori uncertainty for aggregated elements of \mathbf{x} , for example when gridded emissions are summed to give total emissions from a larger region or country.

As all source attribution techniques per se, the Bayesian inversion framework as it is used in this thesis bears some weaknesses. One of the most important is the rather subjective definition of the uncertainty covariance matrices describing the a priori state and the combined model-data-mismatch, introducing an additional source of uncertainty to the result. Recently, more objective methods have been proposed to better cover these introduced uncertainties of the a priori information (e.g. hierarchical Bayesian approach [Ganesan, et al., 2014]) and the transport model [e.g. Gerbig, et al., 2008].

Chapter 4 First observations, trends and emissions of HCFC-31 (CH₂ClF) in the global atmosphere

The following chapter is adopted from :

Schoenenberger, F., M. K. Vollmer, M. Rigby, M. Hill, P. J. Fraser, P. B. Krummel, R. L. Langenfelds, T. S. Rhee, T. Peter, and S. Reimann (2015), First observations, trends, and emissions of HCFC-31 (CH₂ClF) in the global atmosphere, Geophys. Res. Lett., 42, 7817–7824, doi: 10.1002/2015GL064709.

Abstract

We report the first multiyear atmospheric record of HCFC-31 (CH₂ClF), based on flask samples and in situ analyses of air from both hemispheres. Although HCFC-31 has never been produced in large amounts, observed mole fractions in the Northern Hemisphere increased from 2000 onward, reaching 170 ppq (parts per quadrillion, 10⁻¹⁵) in 2011-2012 before decreasing rapidly. By combining our observations with a two-dimensional atmospheric chemistry-transport model, we infer an increase in global emissions from 240 t yr⁻¹ in 2000 to 840 t yr⁻¹ in 2011-2012, followed by a relatively fast decline to 570 t yr⁻¹ in 2014. Emissions of HCFC-31 originate most probably from intermediate product release during the manufacturing process of HFC-32 (CH₂F₂). The rapid decline in recent years could be due to changes in production methods rather than declines in diffusive sources such as landfills or HCFC-31 contaminations in merchandised HFC-32.

4.1 Introduction

Hydrochlorofluorocarbons (HCFCs) are a class of anthropogenic chemicals, used mainly in refrigeration and foam blowing. They were produced initially as chemicals for specific applications and later as replacement compounds to facilitate the phaseout of chlorofluorocarbons (CFCs), which have a large Ozone Depletion Potential (ODP). CFCs were identified as agents to catalyse stratospheric ozone destruction in the early 1970s [Molina and Rowland, 1974] and were banned from emissive usage under the Montreal Protocol, after the discovery of a severe thinning of the ozone layer over Antarctica [Farman, *et al.*, 1985]. HCFCs have at least one C–H bond, which makes

them susceptible to oxidation by hydroxyl radicals (OH) in the troposphere, resulting in a large fraction being destroyed before reaching the stratospheric ozone layer [Carpenter and Reimann, 2014]. Due to their chemical structure, containing both hydrogen and chlorine, HCFCs are denoted as transition substitutes and are also regulated by the Montreal Protocol. In developed countries, production and consumption are still allowed under certain restrictions, while in developing countries, they were not restricted until 2013 [Braathen, et al., 2012], resulting in an accelerated accumulation of HCFCs in the atmosphere during the past decades [Montzka, et al., 2009; Montzka, et al., 2015]. The most abundant HCFCs in the atmosphere are HCFC-22 (CHClF₂), HCFC-141b (CH₃CCl₂F) and HCFC-142b (CH₃CClF₂). In 2012, they reached mole fractions of 219.8 ppt (parts per trillion, 10⁻¹²), 22.5 ppt and 22.0 ppt, respectively, in the global background atmosphere [Carpenter and Reimann, 2014]. In addition to these abundant HCFCs, there are a number of minor HCFCs, such as HCFC-133a (C₂H₂ClF₃) [Laube, et al., 2014] and HCFC-225ca (C₃HCl₂F₅) [Kloss, et al., 2014], which were observed recently in the current atmosphere or in archived air samples. Despite the Montreal Protocol regulations for developed countries, most of these HCFCs are still increasing in the troposphere, due to the allowed, growing use in developing countries.

The topic of this study is HCFC-31 (chlorofluoromethane, CH₂ClF), for which we provide the first measurements in the global atmosphere. Little is known about this compound. Even though HCFC-31 has been used in two refrigerant blends (R-505, R-506) [Agarwal, et al., 2002], it has never been produced industrially in large amounts due to its flammable and carcinogenic character [Höhener, et al., 2003; Balsiger, et al., 2005; DFG, 2013]. HCFC-31 is an intermediate in the synthesis of HFC-32 (CH₂F₂) [Clemmer, et al., 2002; Wismer, 2003; Shantan Rao, et al., 2015], a widely used refrigerant. Further, it is a known product of the anaerobic degradation of CFC-11 (CCl₃F) and was found in emissions from landfills [Scheutz and Kjeldsen, 2003; Balsiger, et al., 2005; Scheutz, et al., 2007a; Scheutz, et al., 2010a].

HCFC-31 is removed from the atmosphere by the reaction with OH [Bhatnagar and Carr, 1996; Charmet, et al., 2013], resulting in a total lifetime of 1.2 years [Carpenter and Reimann, 2014]. It has a radiative efficiency of 0.08 Wm⁻² ppb⁻¹ and a resulting 100 year greenhouse warming potential (GWP) of 83, with an uncertainty of ±30% [Charmet, et al., 2013]. HCFC-31 contains chlorine and is therefore listed in the Montreal Protocol as an ozone depleting substance, with an ODP of 0.02 [Braathen, et al., 2012].

In this paper, we present the first atmospheric records of HCFC-31 based on measurements in archived air samples from various northern hemispheric and southern hemispheric locations and in

situ measurements at a Northern Hemisphere urban and a Southern Hemisphere remote observation site. To quantify global emissions from the observations, the atmospheric abundances are compared to the results of an atmospheric chemistry-transport model. Furthermore, we discuss potential sources and their possible contribution to global emissions.

4.2 Methods

4.2.1 Measurements

To reconstruct past abundances of HCFC-31, we use three different sets of samples for our analysis. For the Northern Hemisphere, the samples consist of air collected in canisters from various remote sites, filled during periods with relatively clean air (when the mole fractions of various compounds, including HCFC-31 are similar to those measured in background air) between 2000 and 2014. Additional northern hemispheric information is gained from air samples collected aboard the Korean research vessel “Araon” during the SHIPPO-2012 expedition, on a transect through the North Pacific from Incheon (South Korea) to Nome (Alaska, USA) (June 2012 - August 2012) [Park and Rhee, 2015]. To track the atmospheric history in the Southern Hemisphere, we analysed air samples from the South Korea Antarctic station King Sejong, located on the Barton Peninsula (King George Island; 62° 13' S, 58° 47' W), as part of a long term flask sampling program [Vollmer, *et al.*, 2011]. The record was complemented by eight archived air samples, collected at Cape Grim (Tasmania) (December 2012 - September 2014), to increase data availability during the reversal in the Southern Hemisphere and to overlap the records from King Sejong and Cape Grim [Langenfelds, *et al.*, 1996; Langenfelds, *et al.*, 2014]. Most of the above mentioned samples are the same as those used by Vollmer *et al.* [2015b] and more detailed sample information can be found there and in the Supporting Information of Schoenenberger *et al.* [2015].

We also measured HCFC-31 continuously, using Medusa-GCMS technology (see Section 4.2.2) [Miller, *et al.*, 2008]. One in situ measurement system is operating at Dübendorf, a suburban site near Zurich (Switzerland). The intercepted air masses at this site can potentially be affected by direct anthropogenic emissions of halogenated greenhouse gases (GHG) from the surrounding areas. Another Medusa-GCMS system is located at the Cape Grim Baseline Air Pollution Station, operated by the Australian Bureau of Meteorology. However data availability is sporadic at these stations due to chromatographic interferences on aged columns (see below). We complemented our intermittent in situ record at Dübendorf with biweekly flask sampling. Sample pairs were collected on the rooftop of the laboratory building into electropolished stainless steel canisters at ~4 bar using an oil free diaphragm pump (KNF-N-022-ANE, Neuberger).

4.2.2 Analytical Setup

Flask sample analyses were carried out at Empa (Swiss Federal Laboratories for Materials Science and Technology, Dübendorf, Switzerland), using a Medusa sample preconcentration unit which is coupled to a gas chromatograph (GC, Agilent 6890N) mass spectrometer (MS, Agilent 5975MS) [Miller, *et al.*, 2008]. The Medusa is equipped with Hayesep-D packed cold traps, which are cooled to -160 °C for preconcentration and heated to ~100 °C for desorption. To enhance peak size and allow for better measurement precision, most flasks were analysed by trapping 4 L of sample, compared to a standard volume of 2 L for routine continuous ambient air monitoring measurements. Preconcentrated samples are chromatographically separated on a 25 m x 0.32 mm ID Agilent CP-Porabond Q column with 5 µm film thickness before detection on a selected-ion mode quadrupole MS. This system has been used for both, HCFC-31 flask measurements and continuous in situ measurements of air from the laboratory building rooftop in Dübendorf.

We identified HCFC-31 on our Medusa-GCMS system by scanning diluted subsamples of a commercial reference multi-component gas mixture (Carbagas, Switzerland) for the mass/charge (m/z) ratio pattern of the most abundant mass fragments from published mass-spectra. On our Empa Medusa-GCMS we found HCFC-31 eluting at ~1170 sec (in the vicinity of perfluorocarbon PFC-318 (c-C₄F₈) and CFC-12 (CCl₂F₂)). It was identified in the mass spectrum based on its most abundant mass fragments m/z 68 as target ion for quantification and m/z 70 as qualifier ion.

During the aging of the chromatographic column, the retention time of HCFC-31 increases faster (5 sec over 10 months) compared to the initially later eluting CFC-12 (3.7 sec over 10 months). Over time, the two compounds interfere until eventually they completely co-elute. All ion fragments of HCFC-31 are also present in CFC-12 on our MS, which has only limited mass resolution (the CH₂³⁵ClF fragment with a m/z of 67.98 is unique for HCFC-31 but cannot be resolved from the CFC-12 fragment C³⁷ClF with a m/z of 67.96). Because of this limitation we lose the capability to detect HCFC-31 in instruments with aged columns and consequently in situ observations, using the same column, are only possible for approximately 10 months. However, HCFC-31 is integrated by peak height and data are flagged for chromatograms with significant peak overlap such that during the initial use of a new chromatographic column, the measurement integrity of HCFC-31 is not affected by the column aging. Ambient air data availability for the Empa Medusa-GCMS is January - October 2013 and November 2014 - July 2015. On the Cape Grim Medusa-GCMS, measurements are available from October 2014 to April 2015.

For the correction of short-term drifts of MS response, a working standard (“quaternary standard”) is measured after each two canister air sample measurements or after each in situ measurement, respectively. These quaternary standards are ambient air compressed into internally electropolished stainless steel canisters (Essex Cryogenics, Missouri, USA) at Rigi-Seebodenalp (Switzerland), using an oil-free diving compressor (SA-6, Rix Industries, USA) or with cryogenic methods at Cape Grim (Tasmania) [Langenfelds, *et al.*, 1996]. The mean measurement precision (1σ) for HCFC-31 is 2.8% for northern hemispheric flask samples after 2008, with atmospheric mole fractions larger than ~ 100 ppq. Older samples with lower abundances have a mean measurement precision (1σ) of 5.7%. Southern hemispheric flask samples with mole fractions below ~ 100 ppq during the whole sampling period have been measured with a mean precision (1σ) of 4.7%. The mean measurement precision for in situ measurements is somewhat lower at 6.0% (1σ), because only 2 L samples are trapped during standard operation of the Medusa-GCMS.

There are no commercial reference standards for HCFC-31 in the low mole fraction range of our observations. This required us to produce our own primary standard by dilution of a commercial ppm (parts per million, 10^{-6}) standard to a mole fraction of ~ 2 ppt, which defines our “Empa-2013 primary calibration scale”, to which all the data of this study are referenced. The accuracy for “Empa-2013” is estimated to be $\pm 6\%$, the overall uncertainty of our reported results is estimated to be $\pm 8\%$ and includes the calibration scale uncertainty, a small uncertainty ($\sim 1\%$) due to the propagation of standards and the analytical precisions outlined above.

Further laboratory tests were conducted to ensure measurement integrity. Experiments were conducted on the Empa Medusa-GCMS to check for potential system non-linearity. They confirmed that our Medusa-GCMS system behaves linearly in the mole fraction range of interest and within measurement uncertainties for HCFC-31 and no systematic biases could be observed. The tests also showed trap breakthrough volumes > 6 L, from which we conclude no sample loss despite the enhanced sample size during this study. The lowest detectable HCFC-31 mole fraction on our Medusa is 14 ppq (2 L samples, 3 times the amplitude of noise) suggesting that even though we are working with very low abundances, we operate well above our detection limits. Our instrument was also free of blank and memory effects well within the detection limits. The stability of HCFC-31 during storage was examined by repeated measurements of a number of samples within a timeframe of 1.5 years. The observed mole fraction differences were random in sign and smaller than the combined measurement uncertainty. We therefore start from the premise that HCFC-31 is stable in the canis-

ters used during this study and trends in mole fractions originate from changes in the troposphere and are not storage artefacts.

4.2.3 Modelling

Global HCFC-31 mole fractions and emission estimates are derived from the AGAGE (Advanced Global Atmospheric Gases Experiment) 12-box model [Cunnold, *et al.*, 1983; Rigby, *et al.*, 2013]. The model divides the Earth's atmosphere into four latitudinal boxes with boundaries at 30°S, the equator and 30°N and three vertical boxes, divided at 500 hPa and 200 hPa. For this study, we prescribed a stratospheric partial lifetime of 35 years [Carpenter and Reimann, 2014], and used OH reaction rates from Sander *et al.* [2011], which, when combined with mean global OH mole fractions from Rigby *et al.* [2013], lead to an overall lifetime of 1.3 years in the model. There is some uncertainty about the lifetime of this species in the literature [Carpenter and Reimann, 2014]. Therefore, we assumed a potential $\pm 20\%$ uncertainty in our lifetime estimates, which is approximately twice the discrepancy between the 2011 and 2014 WMO assessments. This uncertainty is propagated through to our derived emissions (following Rigby *et al.* [2014]).

The AGAGE 12-box model has been used extensively for inverse modelling of global emissions using background atmospheric measurements [Rigby, *et al.*, 2011; Rigby, *et al.*, 2013; Vollmer, *et al.*, 2015b]. In order to derive emissions, a Bayesian approach was used, based on independent a priori estimates of the rate of change of emissions [Rigby, *et al.*, 2011]. Due to the absence of inventory information on HCFC-31, we initiated the model with a prescribed a priori emissions growth rate of $0 \pm 0.5 \text{ kt yr}^{-1}$ from 2000 to 2014.

4.3 Results and Discussion

4.3.1 Observations

Measurements of atmospheric HCFC-31 abundances are shown in Figure 4.1A. The records show early northern mid-latitude dry-air mole fractions of ~ 30 ppq in 2000 and a distinct rise until 2011 - 2012, peaking at ~ 170 ppq. After 2012 measured mole fractions decreased to ~ 110 ppq in early 2015. Results from our northern Pacific air samples [Park and Rhee, 2015] correspond well with the northern hemispheric record, although we observe some variability in these samples. HCFC-31 mole fractions are lower for air advected over the remote Southern Pacific, while there is evidence for higher mixing ratios in air directly advected from the Asian continent. These observations are consistent with similar findings for other anthropogenic trace gases in the same samples [Vollmer, *et al.*, 2015b].

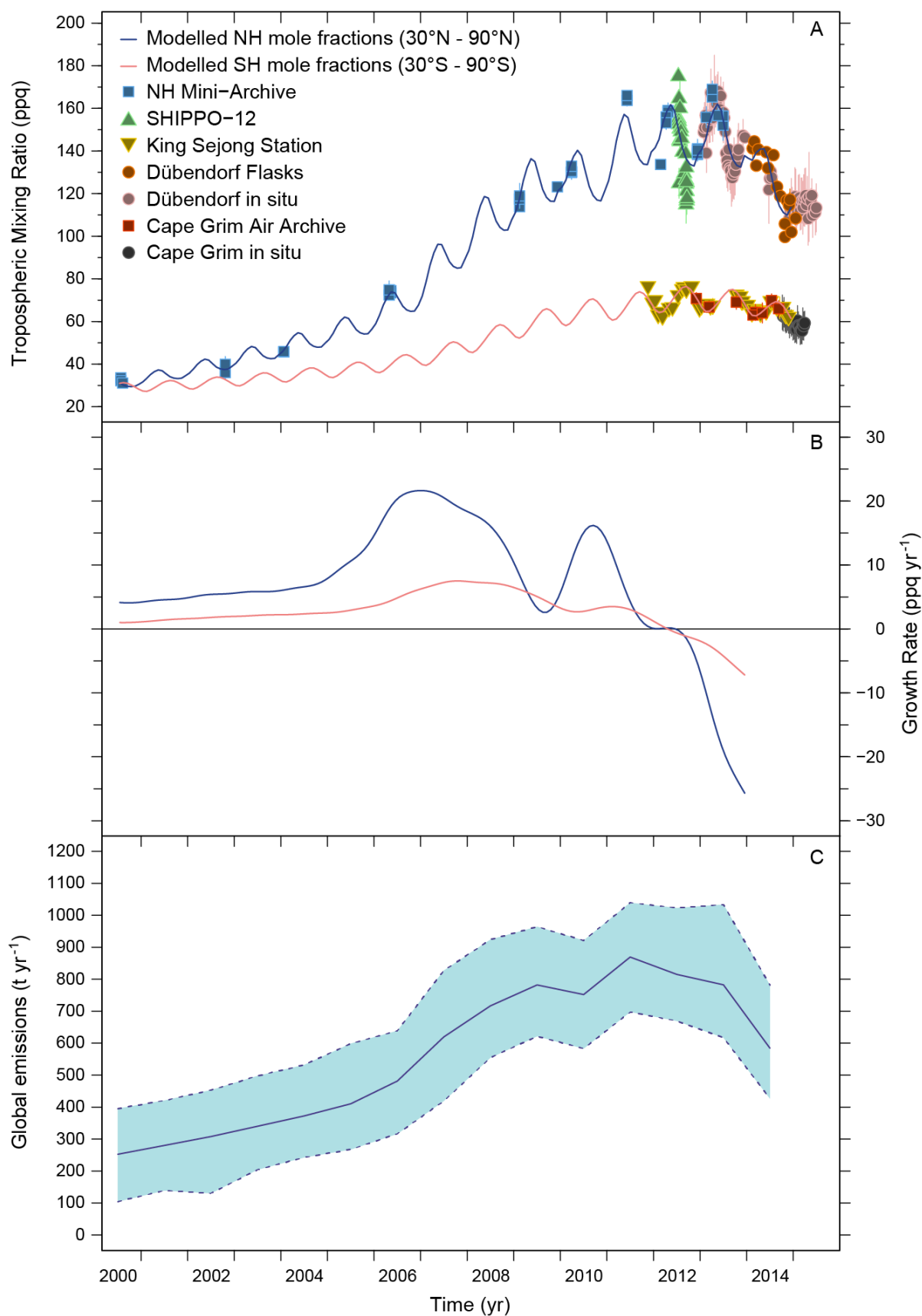


Figure 4.1: (A) Atmospheric record of HCFC-31 (CH₂ClF). Vertical bars: measurement precision ($\pm 1\sigma$) for flask measurements, often smaller than the symbol size, and $\pm 1\sigma$ for in situ measurements, referring to weekly means. Solid lines: dry air mole fractions from the AGAGE 12-box model for the model surface boxes 30°N to 90°N (in blue) and 30°S to 90°S (in red). (B) Growth rates derived from Figure 4.1A for dry air mole fractions in the model surface boxes. (C) Model-derived global emissions in t yr⁻¹.

In the Southern Hemisphere, mole fractions of HCFC-31 are lower, which is indicative of predominantly northern hemispheric emissions. While mean dry air mole fractions in Antarctic air samples from 2012 are ~70 ppq, Cape Grim in situ data from November 2014 - March 2015 drop to ~60 ppq, suggesting a rapid decrease also in the Southern Hemisphere.

The atmospheric history of HCFC-31 was reproduced using the derived emission estimates from the AGAGE 12-box model by running the model in forward mode. The modelled mole fractions agree well with measured values and the seasonal cycle is accurately captured. Maximum model-derived growth rates in the 2000 - 2007 period were ~25 ppq yr⁻¹ (Figure 4.1B). Then the northern hemispheric trend slowed down substantially in 2007 - 2008, followed by another period of increased growth rates in 2008 - 2011. After reaching the above-mentioned northern mid-latitudinal peak values of ~170 ppq in 2012, the model replicates the surprisingly quick and clear reversal of growth rates. The delay of the maximum in the southern hemispheric record, compared to that in the Northern Hemisphere is ~1 yr and corresponds to the typical time scale for interhemispheric tracer transport [Jacob, 1999].

At the suburban site in Dübendorf, we observe a strong seasonal cycle of HCFC-31. Our modelling shows, that this reflects the seasonal variability of OH, the primary sink for HCFC-31, which has a maximum in summer and a minimum in winter [Bhatnagar and Carr, 1996; Spivakovsky, *et al.*, 2000].

4.3.2 Emissions and Potential Sources

The emission estimates, inferred by the AGAGE 12-box model are shown in Figure 4.1C. First observations of changes in the tropospheric mixing ratio in 2000 translate to modelled global emissions of 240 t yr⁻¹ (± 170 t yr⁻¹). Beginning in 2004, we observe an increase of up to 30% per year in global emissions. Emissions stabilize between 2008 and 2012, with peak emissions of around 840 t yr⁻¹ (± 90 t yr⁻¹). In 2012, the emission increase stops and reverses in a sharp manner, decreasing by 30% to 570 t yr⁻¹ (± 110 t yr⁻¹) in 2014. From 2000 - 2014, a global time-integrated total of 8000 t of HCFC-31, with a global climate forcing equivalent to ~700 kt of CO₂, were emitted.

Besides direct synthesis, which has never been carried out in large amounts, there are, to the best of our knowledge, two methods, capable of releasing HCFC-31 into the atmosphere. An average of ~75% of CFC-11, formerly used as blowing agent, is still contained in insulation foam when products are shredded at the end of their operational life span [Scheutz, *et al.*, 2007b]. It is known, that in methanogenic, strongly reducing environments, prevalent in deeper layers of shredded waste land-

fills, CFC-11 can be dechlorinated, producing HCFC-31 [Scheutz and Kjeldsen, 2003; Balsiger, *et al.*, 2005; Scheutz, *et al.*, 2007a; Scheutz, *et al.*, 2010a]. While most of the reduced compounds are oxidized in shallower, aerobic layers, low emissions of HCFC-31 ($0.006 \text{ g m}^{-2} \text{ d}^{-1}$) were detected during a field study at a Danish waste facility [Scheutz, *et al.*, 2010b]. While we cannot exclude a contribution of HCFC-31 emissions from landfills, the rapid decline in global emissions from 2013 onwards is inconsistent with gradual changes expected from landfill emissions. Therefore only a minor contribution from this source is presumed for the measured HCFC-31 mole fractions in the atmosphere.

A more plausible explanation is emissions of HCFC-31 related to the production and use of HFC-32, a popular, non-ozone depleting substance used in mixtures such as R-407 and R-410 as substitute for phased-out refrigerants. In developed countries, major consumption of HFC-32 started around 2000, while the rapid increase of HFC-32 use in developing countries started around 2005 (Velders, National Institute for Public Health and the Environment, RIVM, unpublished data, 6. March 2015), resulting in estimated global emissions of $21'000 \pm 11'000 \text{ t yr}^{-1}$ in 2012 [O'Doherty, *et al.*, 2014]. To produce HFC-32, methylene chloride (CH₂Cl₂) or HCFC-22 (CHF₂Cl) is reacted with hydrogen fluoride (HF) or hydrogen (H₂), whereupon HFC-32 is extracted from the reactor effluent, comprising HFC-32, unreacted feedstock substances, HF or H₂, HCl and HCFC-31 as an intermediate substance [Frischknecht, 1999; Wismer, 2003]. However, assuming good factory practice, unreacted CH₂Cl₂ or CHF₂Cl and HCFC-31 are fully recovered during the extraction process and reinjected into the production chain (McFarland, Dupont, personal communication, 27. February 2015).

The rapid reversal of the estimated global emissions of HCFC-31 points to a shutdown of sources that were under direct and immediate human control and less likely to diffusive sources related to banked HCFC-31, stored in equipment or other reservoirs. We speculate that a significant fraction of past HCFC-31 emissions resulted from factory release during HFC-32 synthesis under potentially poorly optimized production conditions. Our observed rapid decline in these emissions would consequently be a result of improvements in the synthesis at one or a few factories, an overall reduction of their HFC-32 production, or both. Our hypothesis is supported by the absence of any known purposeful significant end-user application of HCFC-31, which could otherwise have a similar effect on the tropospheric mole fraction, once halted from release to the atmosphere.

There is a strikingly parallel behaviour between the atmospheric records and derived emissions of HCFC-31 and HCFC-133a, a recently discovered compound, which also has no known significant

end-use applications [Laube, *et al.*, 2014]. A reversal of atmospheric abundances and emissions was also found for HCFC-133a, over a similar period as for HCFC-31 (M. K. Vollmer, personal communication). This finding supports the hypothesis of [Laube, *et al.*, 2014] that an earlier interruption of the HCFC-133a increase in the atmosphere might be due to changes in production plants, presumably some of those for the synthesis of HFC-134a, HFC-125 or HFC-143a, where HCFC-133a is an intermediate product.

If HCFC-31 is an impurity in merchandised HFC-32, then the two would be co-emitted during the leakage of installed HFC-32. While atmospheric abundances and inferred emissions have also grown for HFC-32 during the growth period of HCFC-31 [O'Doherty, *et al.*, 2014], we propose that the reversal we find for HCFC-31 is inconsistent with this scenario. HFC-32 emissions continue to grow and the compound is built into refrigeration systems for which a sudden prevention of leakage is unrealistic. Also, our measurement program at urban Dübendorf includes HFC-32 for which we find large pollution events. However simultaneously occurring pollution events for HCFC-31 are absent from this record, suggesting no significant impurities of HCFC-31 in the HFC-32 installed within the air-mass footprint of our station. Measurements of potential HCFC-31 impurities in various HFC-32 products would lead to an improved understanding of such a HCFC-31 source, but it would be a difficult and elaborate task due to the large number of plants and the poorly traceable distribution.

4.4 Conclusion

We present the first measurements of HCFC-31 in the global background atmosphere. Although HCFC-31 has never been produced in large amounts, we observe a distinct increase in the tropospheric mixing ratio between 2000 and 2012. While the contribution to global radiative forcing and stratospheric ozone depletion is small for HCFC-31 alone, the collective effects of all HCFCs are significant [Montzka, *et al.*, 2009; Hodnebrog, *et al.*, 2013; Montzka, *et al.*, 2015], calling for high accuracy measurements in accordance with the Montreal Protocol and its amendments.

HCFC-31 is produced as an intermediate during the synthesis of HFC-32, a popular alternative used in mixtures for the replacement of ozone-depleting refrigerants. Due to the relatively rapid variations that we infer in global emissions of HCFC-31, we expect a limited number of industrial emitters to be the most plausible source for a large fraction of the measured HCFC-31.

Minor additional contributions can originate from the production of HCFC-31 during the anaerobic depletion of CFC-11 (e.g. in landfills) or the release of HCFC-31 as an unintended contamination in

merchandised HFC-32. However, we do not find evidence of significant co-emission of HCFC-31 and HFC-32 in observations at the Dübendorf station, where HFC-32 pollution events regularly occur, but coincident elevated HCFC-31 is absent.

The discovery of HCFC-31 in the global background atmosphere during this study and other examples of recently found, non-reported substances [Kloss, *et al.*, 2014; Laube, *et al.*, 2014; Vollmer, *et al.*, 2015b], highlights the necessity of a continuous top-down monitoring of feedstock, intermediates and products, even if production processes are designed not to lead to such emissions. Therefore HCFC-31 should be further monitored to ensure that its decline continues and additional efforts are needed to isolate the specific emission sources. Further, the ongoing search for previously unidentified chemicals in the atmosphere should be encouraged.

Acknowledgements

This research was funded by the Swiss National Science Foundation (project no. 200021-137638), the Swiss Federal Office for the Environment (FOEN) and the Swiss State Secretariat for Education and Research and Innovation (SERI). Additional support comes from InGOS (Integrated Non-CO₂ Greenhouse Gas Observing System) and the National Research Foundation of Korea for the Korean-Swiss Science and Technology Cooperation Program. We thank the personnel of the King Sejong Research station, the personnel (Australian Government Bureau of Meteorology) of the Cape Grim Baseline Air Pollution Station and the crew of the research vessel Araon for collecting the air samples for this research. Paul Steele (CSIRO) is deeply acknowledged for transferring archived air samples and for setting up continuous HCFC-31 measurements in Cape Grim. We acknowledge the support of our colleagues from the Advanced Gases Experiment (AGAGE). M. R. is supported by an advanced research fellowship from the UK Natural Environment Research Council (NERC) NE/1021365/1. T. S. R. is supported by the Korean Polar Research Program PE 13410. P.F. and P.K. are supported by CSIRO and the Bureau of Meteorology. Data in this study are available from the supplementary information and the corresponding author.

Chapter 5 Abundance and sources of atmospheric halocarbons in the Eastern Mediterranean

The following chapter is adopted from the paper draft for submission to Atmos. Chem. Phys. :

Schoenenberger F., S. Henne, M. Hill, M.K. Vollmer, G. Kouvarakis, N. Mihalopoulos, S. O'Doherty, M. Maione, L. Emmenegger, T. Peter and S. Reimann, Abundance and Sources of Atmospheric Halocarbons in the Eastern Mediterranean, Atmos. Chem. Phys., prepared for publication.

Abstract

A wide range of anthropogenic halocarbons is released to the atmosphere, contributing to stratospheric ozone depletion and global warming. Using measurements of atmospheric abundances for the estimation of halocarbon emissions on the global and regional scale has become an important top-down tool for emission validation in the recent past, but many populated and developing areas of the world are only poorly covered by the existing atmospheric halocarbon measurement network. Here we present six months of continuous halocarbon observations from Finokalia on the island of Crete in the Eastern Mediterranean. The gases measured are the hydrofluorocarbons (HFCs), HFC-134a (CH_2FCF_3), HFC-125 (CHF_2CF_3), HFC-152a (CH_3CHF_2) and HFC-143a (CH_3CF_3), and the hydrochlorofluorocarbons (HCFCs), HCFC-22 (CHClF_2) and HCFC-142b (CH_3CClF_2). The Eastern Mediterranean is home to 250 million inhabitants, consisting of a number of developed and developing countries, for which different emission regulations exist under the Kyoto and Montreal Protocols. Regional emissions of halocarbons were estimated with Lagrangian atmospheric transport simulations and a Bayesian inverse modelling system, using measurements at Finokalia in conjunction with those from the Advanced Global Atmospheric Gases Experiment (AGAGE) sites at Mace Head (Ireland), Jungfraujoch (Switzerland) and Monte Cimone (Italy). Measured peak mole fractions at Finokalia showed generally smaller amplitudes for HFCs than at the European AGAGE sites, except periodic peaks of HFC-152a, indicating strong upwind sources. Higher peak mole fractions were observed for HCFCs, suggesting continued emissions from nearby developing regions

such as Egypt and the Middle East. For 2013, the Eastern Mediterranean inverse emission estimates for the four analysed HFCs and the two HCFCs were 14.7 (6.7-23.3) Tg CO₂eq yr⁻¹ and 9.7 (4.3-15.7) Tg CO₂eq yr⁻¹, respectively. These emissions contributed 17.3% (7.9-27.4%) and 53% (23.5-86%) to the total inversion domain, which covers the Eastern Mediterranean as well as Central and Western Europe. Greek bottom-up HFC emissions reported to the UNFCCC were much smaller than our top-down estimates, whereas for Turkey our estimates agreed with UNFCCC-reported values for HFC-125 and HFC-143a, but were much and slightly smaller for HFC-134a and HFC-152a, respectively. Sensitivity estimates suggest an improvement of the a posteriori emission estimates, i.e. a reduction of the uncertainties by 40-80% compared to an inversion using only the existing Central European AGAGE observations.

5.1 Introduction

Anthropogenic halocarbons, i.e. chlorofluorocarbons (CFCs), hydrochlorofluorocarbons (HCFCs), hydrofluorocarbons (HFCs), halons and other brominated species, are used in a wide range of industrial and domestic applications (e.g., refrigeration, air conditioning, foam blowing, solvent usage, aerosol propellants and fire retardants). Whereas only chlorinated and brominated halocarbons are responsible for stratospheric ozone depletion, all halocarbons are potent greenhouse gases [Molina and Rowland, 1974; Farman, *et al.*, 1985; Myhre, *et al.*, 2013; Carpenter and Reimann, 2014].

Ozone depleting substances (ODSs) are regulated by the Montreal Protocol (MP), which resulted in the global phase-out of CFCs from emissive use by 2010. HCFCs, which serve as transitional replacement products, are subject to a less demanding multistep phase-out ending in 2030 for Non-Article-5 (developed) and 2040 for Article-5 (developing) countries [Braathen, *et al.*, 2012]. To track the development of CFC and HCFC emissions to the atmosphere, the MP requires signatory parties to produce an inventory of their ODS consumption and production [McCulloch, *et al.*, 2001].

HFCs, used as second generation replacement products for ODSs, do not contain chlorine or bromine. However, as some of them have a large global warming potential (GWP) and a projected rapid increase in their emissions, HFCs may significantly contribute to global radiative forcing as a direct consequence of protecting the ozone layer [Steinbacher, *et al.*, 2008; Velders, *et al.*, 2012; Rigby, *et al.*, 2014; Montzka, *et al.*, 2015]. HFCs are addressed within the Kyoto Protocol to the United Nations Framework Convention on Climate Change (UNFCCC). Signatory parties with binding emission reduction targets (Annex I) are required to submit their HFC emission inventories to the UNFCCC [UNFCCC, 1997]. These inventories are based on statistical “bottom-up” estimates,

using production and consumption data and have been suspected to carry significant uncertainties [e.g., *Levin, et al.*, 2010; *Keller, et al.*, 2012; *Rigby, et al.*, 2014; *Lunt, et al.*, 2015].

To validate reported inventories, “top-down” approaches, based on atmospheric measurements and atmospheric transport and chemistry models can be used. The combination of observations with simplified global scale box-models, allows the independent monitoring of global emissions [e.g., *Rigby, et al.*, 2010; *Carpenter and Reimann*, 2014; *Schoenenberger, et al.*, 2015; *Vollmer, et al.*, 2015b]. The application of more detailed atmospheric models has proven to be a powerful tool to quantify emissions on a spatially and temporally more explicit level enabling for emission estimates on a continental to country scale [*Manning, et al.*, 2003; *Stohl, et al.*, 2009; *Kim, et al.*, 2010; e.g. *Brunner, et al.*, 2012a; *Keller, et al.*, 2012; e.g., *Saikawa, et al.*, 2012; *Ganesan, et al.*, 2014; *Maione, et al.*, 2014; *Graziosi, et al.*, 2015; *Hu, et al.*, 2015; *Lunt, et al.*, 2015].

In Europe, the AGAGE network provides high-frequency observations of atmospheric halocarbons at 3 sites: Mace Head (Ireland), Zeppelin mountain (Spitsbergen, Norway), Jungfraujoch (Switzerland) and the affiliated station at Monte Cimone (Italy) [*Prinn, et al.*, 2000]. While data from this network have been frequently used in top-down estimates of Western European halocarbon emissions [e.g., *Reimann, et al.*, 2008; *Brunner, et al.*, 2012b; *Keller, et al.*, 2012], the network has a very limited sensitivity towards emission from Eastern European sources (Figure 1.1a). For Eastern European HFC emissions, the importance of extending the observational network was illustrated by the large discrepancies between bottom-up emissions reported to UNFCCC and those estimated top-down in an inverse modelling study using atmospheric observations obtained during a field campaign at K-Pusztas in Hungary [*Keller, et al.*, 2012].

Even less reliable information is available on halocarbon emissions from the Eastern Mediterranean region, comprising the Article 5/Annex I country Turkey, Non-Article 5/Annex I states such as Greece, Romania, Bulgaria and Cyprus and developing economies (Article 5/Non Annex I) such as Egypt and Israel with less stringent regulations and reporting requirements.

Estimating halocarbon emissions by top-down methods in the Eastern Mediterranean gains additional importance in the light of the beginning phase-out of HCFC emission in Article-5 countries under the Montreal Protocol. This motivated our halocarbon measurement campaign at Finokalia (Crete, Greece) from December 2012 to August 2013. Here, we present the observed atmospheric halocarbon levels and combine the dataset with halocarbon observations at Jungfraujoch, Mace Head and Monte Cimone, atmospheric transport modelling and a Bayesian inversion system to de-

rive the first comprehensive top-down emission estimates of HFC-134a (CH_2FCF_3), HFC-125 (CHF_2CF_3), HFC-152a (CH_3CHF_2), HFC-143a (CH_3CF_3), HCFC-22 (CHClF_2) and HCFC-142b (CH_3CClF_2) in the Eastern Mediterranean.

5.2 Methods

5.2.1 Observational Sites

Halocarbon measurements were conducted from December 2012 to August 2013 at the atmospheric observation site in Finokalia (FKL, 35.34°N, 25.67°E, 250 m a.s.l. [UOC, 2016]), which is part of the “Aerosol, Clouds and Trace gases Research Infrastructure” (ACTRIS). The station is located on the northeastern coast of Crete on top of a hill, facing the Mediterranean Sea within a sector from 270° to 90°. It is surrounded by sparse vegetation and olive tree plantations, without significant human activity in the near vicinity, except a small village 3 km to the South. Heraklion, the closest, more densely populated area (~200'000 inhabitants), is situated approximately 50 km west of Finokalia.

Operational meteorological observations, such as wind speed, wind direction, temperature, relative humidity and solar radiation are available at the station. In addition to classical air quality parameters (ozone, nitrogen oxides, carbon monoxide) the station is equipped with a large suite of aerosol measurements.

The halocarbon observations at Finokalia were complemented with data from the AGAGE sites at Jungfraujoch and Mace Head and from Monte Cimone for this study. The high-altitude site Jungfraujoch (JFJ, 7.99°E, 46.55°N, 3573 m a.s.l.) is located in the northern Swiss Alps. It is usually exposed to free tropospheric air but can also be affected by polluted boundary layer air from both sides of the Alps [Zellweger, *et al.*, 2003; Henne, *et al.*, 2010; Herrmann, *et al.*, 2015]. The Mace Head observatory (MHD, 9.90°W, 53.33°N, 15 m a.s.l.) on the west coast of Ireland is normally exposed to relatively clean air from the North Atlantic Ocean but can also be influenced by continental European air masses under certain atmospheric transport conditions. Similar to Jungfraujoch the high-altitude site Monte Cimone (CMN, 10.70°E, 44.18°N, 2165 m a.s.l.) in the Apennine Mountains in Northern Italy is often situated in the lower free troposphere, but especially during daytime receives polluted boundary layer air [Bonasoni, *et al.*, 2000].

5.2.2 Analytical Methods

In situ measurements of halocarbons at the Finokalia observation site were conducted using a gas chromatograph (Agilent 6890) mass spectrometer (Agilent 5973) (GCMS), coupled to an adsorption desorption system (ADS) for pre-concentration of samples from the air [Simmonds, *et al.*, 1995]. A similar instrument is used at Monte Cimone [Maione, *et al.*, 2013]. The ADS is the predecessor of the Medusa pre-concentration unit, which is currently used at the AGAGE sites Jungfraujoch and Mace Head [Miller, *et al.*, 2008].

Two litres of air were sampled every 2 hours, with a collection duration of 40 min, 2 m above the rooftop of the station building, using an inlet facing the open sea. For the correction of short-term drifts of the mass spectrometer response, a working standard was measured after each 10th air sample analysis. Two such standards were used throughout the project, both real-air samples compressed into internally electro-polished stainless steel canisters (Essex Cryogenics, Missouri, USA) at Rigi-Seebodenalp (Switzerland), using an oil-free diving compressor. These working standards were calibrated against standards provided by the Scripps Institution of Oceanography (SIO). All results are reported on SIO calibration scales and expressed as dry air mole fractions in parts per trillion (ppt), 10⁻¹². The respective scales are SIO-05 for HFC-134a, HFC-152a, HCFC-22 and HCFC-142b, SIO-07 for HFC-143a and SIO-14 for HFC-125.

The measurement precision, which is calculated separately for each compound, was estimated as the standard deviation of the working standard observations, inside a moving window covering 10 standard measurements (Table 5.1). Note that the precision for the ADS measurements at Finokalia was up to an order of magnitude worse than for the sites equipped with the Medusa system. This was partly caused by less frequent reference gas measurements by the ADS compared to the Medusa. Nevertheless, for the atmospheric inversion this reduction in measurement precision can be tolerated, since the largest part of the total uncertainty in the inversion is contributed by uncertainties in the transport model.

5.2.3 Data Treatment

Data quality was ensured by examining chromatographic quality and comparing observed mole fractions to observations at selected European AGAGE sites (JFJ, MHD, CMN). Specific observations, showing poor chromatographic quality or unrealistic measurement behaviour were excluded from the time series.

Due to hardware problems of our mass spectrometer, no measurements were conducted from 22 March to 14 April. During the summer (June to August), the observation data behaviour of HFC-134a and HFC-125 suggested a local pollution source in the vicinity (a few 100 m) of the station, assumed to be a leaking refrigeration/air conditioning system close by. Because the transport model (see section 5.2.4) cannot account for such local emissions, HFC-125 and HFC-134a data were removed during the summer when local wind speeds were below 4 m s^{-1} and the wind direction was NNE-E.

Table 5.1: Basic statistics for the 3-hourly aggregates of the observations taken at all sites during the campaign period (Dec. 2012 – Aug. 2013). Observation sites are: Finokalia (FKL), Jungfraujoch (JFJ), Mace Head (MHD), Mt. Cimone (CMN). Shown are the number of observations (N), the mean, minimum (Min), maximum (Max) and standard deviation (SD) for the observations and the baseline values, estimated with REBS. The mean measurement uncertainty (σ_o) was determined from the standard deviation of reference gas measurements and the baseline uncertainty (σ_b) was derived as one constant value by the REBS method (see Section 5.2.3).

	Site	N	Observations					Background (REBS)			
			Mean	Min	Max	SD	σ_o	Mean	Min	Max	σ_b
			[ppt]	[ppt]	[ppt]	[ppt]	[ppt]	[ppt]	[ppt]	[ppt]	[ppt]
HFC-134a	FKL	1467	80.8	72.8	94.2	3.4	0.8	79.7	77.2	83.0	1.9
	JFJ	1383	80.7	70.9	119.3	5.3	0.2	77.0	74.6	79.1	1.3
	MHD	1533	80.3	73.5	122.0	5.6	0.2	77.4	76.3	78.9	0.7
	CMN	1040	86.1	72.8	129.3	8.7	0.3	80.1	76.2	83.1	1.7
HFC-125	FKL	1193	15.9	12.8	22.3	1.3	0.4	15.3	14.1	16.1	0.6
	JFJ	1373	16.1	13.3	26.9	1.7	0.1	14.9	14.1	15.7	0.3
	MHD	1514	15.8	13.9	28.1	1.7	0.1	14.9	14.5	15.4	0.2
	CMN	1078	17.6	13.4	33.3	2.6	0.1	15.8	14.6	16.8	0.6
HFC-152a	FKL	1428	11.5	7.8	19.3	1.6	0.2	10.6	10.3	10.7	0.8
	JFJ	1395	10.8	6.9	25.0	1.7	0.1	10.0	9.4	10.5	0.8
	MHD	1527	10.9	8.4	15.0	0.9	0.1	10.6	9.7	10.8	0.4
	CMN	1096	11.7	7.3	21.6	1.9	0.1	10.3	9.7	10.7	0.7
HFC-143a	FKL	1252	17.4	13.2	29.6	2.2	1.2	16.3	15.8	16.7	0.9
	JFJ	1411	16.7	13.7	25.6	1.6	0.1	15.4	14.5	16.0	0.3
	MHD	1540	16.6	14.8	27.6	1.8	0.1	15.5	15.3	15.9	0.2
	CMN	1055	17.5	14.2	27.1	1.9	0.1	16.0	15.1	16.8	0.5
HCFC-22	FKL	1438	235.8	226.9	271.6	3.5	1.8	234.7	233.0	237.9	2.3
	JFJ	1389	234.9	224.9	252.4	2.9	0.6	234.2	233.0	236.3	2.2
	MHD	1523	235.8	230.3	259.8	1.8	0.6	235.2	235.0	236.0	1.1
	CMN	980	235.1	225.2	255.5	3.3	0.7	234.0	232.2	235.8	1.9
HCFC-142b	FKL	1075	23.9	21.3	27.2	0.9	0.6	23.7	22.6	24.5	0.5
	JFJ	1392	23.4	22.4	26.1	0.4	0.1	23.2	23.1	23.4	0.2
	MHD	1533	23.3	22.7	24.7	0.2	0.1	23.2	23.1	23.3	0.1
	CMN	1046	23.8	22.5	26.8	0.5	0.1	23.5	23.2	23.8	0.3

Since the transport simulations can only account for the regional emissions in a limited domain and during the time of backward integration (see Section 5.2.4), it was necessary to obtain a baseline mole fraction that represents the conditions at the endpoints of the transport simulation. To this end, a statistical method was applied to the observations assuming that a considerable part of the observations was not, or only weakly, influenced by emissions within the period of the transport simulation. The “Robust Estimation of Baseline Signal” (REBS) algorithm [Ruckstuhl, *et al.*, 2012] detects these baseline observations by iteratively fitting a local linear regression model to the data, excluding data points outside a range around the baseline and finally arriving at a smooth baseline curve. The measured dry air mole fraction, X_O , can then be represented as the sum of the baseline mole fraction, $X_{O,b}$, and the input due to recent emissions, $X_{O,E}$.

The REBS method was applied separately to the high frequency observation data of each compound and each observation site, using a temporal window width of 30 days and a maximum of 10 iterations with asymmetric robustness weights. Derived mean baseline values for each site and the respective baseline uncertainties, σ_b , are shown in Table 5.1. Finally, three-hourly aggregates were produced from the observations at Finokalia and the other European AGAGE sites (JFJ, MHD, CMN) in order to match the transport model’s temporal output interval.

5.2.4 Transport Simulations

The Lagrangian Particle Dispersion Model FLEXPART (version 9.02) [Stohl, *et al.*, 2005] was used to derive source sensitivities, also referred to as footprints, for 3-hourly intervals at all four observational sites. The source sensitivities quantify the effect of an emission source at a certain grid location and of unit strength (1 kg s^{-1}) on the mole fractions at the receptor. Multiplication of the source sensitivity with an emission field and summation over the entire grid yields the simulated mole fraction at the receptor [Seibert and Frank, 2004; Stohl, *et al.*, 2009]. FLEXPART calculates transport by mean and turbulent flow as well as transport within convective clouds. Here, it was driven by meteorological fields obtained from the operational analysis of the Integrated Forecast System (IFS), provided by the European Centre for Medium-Range Weather Forecasts (ECMWF). Input fields were available at 3-hourly intervals at a global resolution of 1° by 1° and a nested domain with a resolution of 0.2° by 0.2° for the Alpine area. FLEXPART was run in “backward” mode, where 50’000 particles were released from each observation site in 3-hourly intervals and followed 10 days backward in time. Assuming that emissions are predominantly originating at the ground, the source sensitivities were calculated for a layer reaching from 0 m to 100m above ground. According to the experience of previous studies, the release height of particles, followed by FLEX-

PART along backward trajectories, was set to 3000 m a.s.l. and 2000 m a.s.l. for the high-altitude stations JFJ and CMN, respectively, where model and real topography differ significantly [Keller, *et al.*, 2012]. For FKL a particle release height of 150 m a.s.l., corresponding to 30 m above the model topography, was chosen, 70 m below the real altitude. However, a comparison between this release height and a release at the true altitude above sea level did not show any significant differences.

Because of the long lifetime of the substances analysed in this study, removal processes were neglected in the FLEXPART simulations. Of the analysed compounds, HFC-152a has the shortest tropospheric lifetime of 1.6 years [Carpenter and Reimann, 2014]. Applying this average lifetime, only about 1.7 % of fresh HFC-152a emissions would be degraded during the 10 day transport period.

5.2.5 Atmospheric Inversion

To estimate spatially resolved emissions, a Bayesian inversion method [Enting, 2002] as implemented and described in Henne *et al.* [2016] was used. Here we only describe the most integral parts of the method and modifications as compared with Henne *et al.* [2016].

In short, the source sensitivities simulated by FLEXPART provide the link to describe a linear relationship between simulated mole fractions at the observation sites, y , and an emission field, x , which can be written in matrix notation as

$$y = \mathbf{M}x, \quad (19)$$

where \mathbf{M} is the source sensitivity matrix constructed from the individual source sensitivities. The state vector, x , contains the emissions of each grid cell in the inversion grid and baseline mole fractions, given at baseline nodes at discrete time intervals for each site. Consequently, the matrix \mathbf{M} contains two block matrices \mathbf{M}^E and \mathbf{M}^B , denoting the dependence on emissions and baseline mole fractions, respectively. \mathbf{M}^B is designed such that the elements represent temporally linear interpolated values between neighbouring baseline nodes [Stohl, *et al.*, 2009; Henne, *et al.*, 2016].

In the Bayesian approach, the a posteriori state, x_{post} , is obtained such that the simulations optimally fit the observations, y_O , under the presumption of a given prior state x_{prior} . This can be achieved by the minimization of the following cost function,

$$J = \frac{1}{2} (x_{post} - x_{prior})^T \mathbf{B}^{-1} (x_{post} - x_{prior}) + \frac{1}{2} (\mathbf{M}x_{post} - y_0) \mathbf{R}^{-1} (\mathbf{M}x_{post} - y_0), \quad (20)$$

where the first term gives the deviation of the posterior state vector x_{post} from the a priori state vector x_{prior} and the second term, the misfit between the simulated mole fractions, $\mathbf{M}x_{post}$, and the observations, y_0 . \mathbf{B} is the uncertainty covariance matrix of the a priori state vector and \mathbf{R} denotes the uncertainty covariance matrix of the data-mismatch and contains both observation and model uncertainties. Section 5.2.7 details how \mathbf{B} and \mathbf{R} were set up for this study.

To increase the spatial coverage of our analysis and thereby reduce the uncertainties at the periphery of the Eastern Mediterranean, simultaneous measurements from the three AGAGE sites in Western Europe were included in addition to those in Finokalia. Thus, our inversion grid covered most of Southern and Central Europe, reaching from the Atlantic to the Middle East. To represent the large variety of advection patterns, influencing the observations at the AGAGE sites in our study area, measurements from Dec. 2012 – Dec. 2013 were used in the inversion.

The applied inversion derives spatially-resolved, but temporally-constant emissions. In order to reduce the size of the inverse problem, which depends on the number of grid cells, an inversion grid with variable grid resolution was defined. Grid cells, for which the average source sensitivity was below a predefined threshold, were joined with their neighbours until the combined source sensitivity was sufficiently large or up to a maximum horizontal grid size of 6.4° by 6.4° . In contrast to previous studies, using variable grid resolutions [Stohl, *et al.*, 2009; Brunner, *et al.*, 2012a; Henne, *et al.*, 2016], the initially computed irregular grid was manually adjusted to ensure that large grid cells did not overlap with different emission regions. This assured a more accurate assignment of emissions per region and their uncertainties, especially in the case of large emissions close to regional borders, and when different a priori uncertainties were given to neighbouring regions.

5.2.6 A priori Emissions

A Bayesian inversion requires a priori knowledge of the state vector to guide the optimisation process. In order to specify a priori emissions and their uncertainty for each grid cell of the inversion grid, emission information was collected on the country/region level and then spatially disaggregated following population density. Since optimising emissions from small and distant (from the observation locations) countries can be afflicted with large uncertainties, we aggregated country-specific a priori information to larger regions (see Table 5.5 and Figure 5.1 for region definitions).

These were introduced with the intention to separate developed (Annex I/non-Article 5) and developing (non-Annex I/Article 5) countries wherever possible. Total a priori uncertainties were assigned to each country/region and each compound separately and then spatially disaggregated following the same population density as for the emissions, which results in constant relative uncertainties for each country/region. This is an improvement as compared with previous studies that used uniform relative uncertainty in the whole inversion domain. [e.g., *Keller, et al.*, 2012].

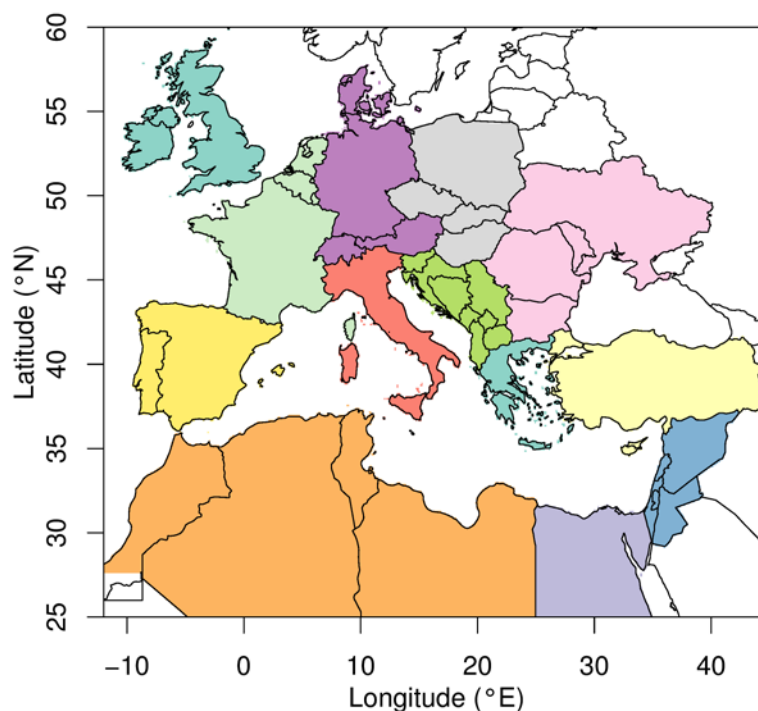


Figure 5.1: Illustration of region definition used in the discussion of emission estimates: Greece (light turquoise), Turkey (Turkey, Cyprus; pale yellow), Balkans (Serbia, Montenegro, Kosovo, Albania, Bosnia and Herzegovina, Croatia, Slovenia, Macedonia; light green), Eastern (Ukraine, Romania, Moldova, Bulgaria; pale pink), Middle East (Jordan, Lebanon, Syria, Palestine, Israel; blue), Egypt (pale purple), Maghreb (Morocco, Algeria, Tunisia, Libya; orange), Central E (Poland, Slovakia, Czech-Republic, Hungary; grey), Central W (Switzerland, Liechtenstein, Germany, Austria, Denmark; purple), Western (France, Luxembourg, Netherlands, Belgium; pale green), Italy (red), Iberian Peninsula (Spain, Portugal; yellow), British Isles (Ireland, United Kingdom; light turquoise).

Our a priori country total HFC emissions for Annex I parties were based on the 2016 National Inventory Submissions to the UNFCCC [UNFCCC, 2016a] for the year 2013, collected from individual country “common reporting format” tables. To estimate prior emissions for countries within our inversion domain not reporting to the UNFCCC (Non-Annex I), reported emissions were subtracted from estimated global emissions in 2012 provided by *Carpenter and Reimann* [2014]. The remaining emissions were further disaggregated to the individual country level, based on population data, provided by the UN population division [UN, 2016]. Uncertainties for reported “bottom-up” emissions were arbitrarily set to 20%, whereas estimated a priori emissions for non-reporting coun-

tries were given a higher uncertainty of 100% (Table 5.5). The sensitivity of our posterior emissions to these choices was analysed in additional inversion runs (see Section 5.2.8).

HCFC-22 global emission estimates provided by *Carpenter and Reimann* [2014] were distributed based on regionally estimated shares by *Saikawa et al.* [2012], assuming that contribution ratios of the regions defined in their study have not changed significantly since the period of 2005 – 2009. Emission estimates in areas with differing regional extents in our study compared to that of *Saikawa et al.* [2012] were rearranged using population data. The resulting prior emissions for the European domain compare well with estimated European emissions, derived by *Keller et al.* [2012] during their campaign in 2011. Uncertainties were calculated to add up to a combined uncertainty of the used global estimate from *Carpenter and Reimann* [2014] and the regional estimates derived by *Saikawa et al.* [2012] (Table 5.5).

Based on the assumption, that HCFC-142b and HCFC-22 emissions are largely collocated, the same above mentioned regional emission shares are used to derive HCFC-142b prior emissions. Resulting European emissions were further scaled to match HCFC-142b estimates from *Keller et al.* [2012], while Russian emissions, which were not covered in the above mentioned study, were scaled using temporally extrapolated emissions from EDGAR [*JRC/PBL*, 2009]. Due to the lack of information and on the basis that Article 5 countries are still allowed to use HCFCs after the phase-out of HCFCs in non-Article 5 countries, North African and Middle Eastern countries within our domain were left unscaled, but given a regional total uncertainty of 100% allowing for substantial corrections of the a priori emissions by the inversion. European regions containing developing and developed countries, as well as Russia were assigned a smaller uncertainty of 50%, reflecting the availability of scaling information.

5.2.7 Covariance Treatment

We followed three different strategies how to design the covariance matrices \mathbf{B} and \mathbf{R} . The first two (‘Global’ and ‘Local’) use complete uncertainty covariance matrices and are similar to the one used in *Henne et al.* [2016], whereas the third method (‘Stohl’) assumes uncorrelated uncertainties and uses diagonal-only uncertainty covariance matrices [*Stohl, et al.*, 2009]. The latter has already been used successfully to derive regional halocarbon emissions [e.g. *Vollmer, et al.*, 2009; *Keller, et al.*, 2012].

The uncertainty covariance matrix \mathbf{B} of the a priori state-vector consists of two symmetric block matrices \mathbf{B}^E and \mathbf{B}^B , containing the uncertainty covariance of the gridded a priori emissions and the

baseline mole fractions, respectively. Diagonal elements of \mathbf{B}^E , defining the uncertainty of each grid cell emission, were set proportional to the a priori emissions in each cell. The diagonal elements of \mathbf{B}^B were set to the constant value of the baseline uncertainty σ_b , as estimated by the REBS method for each observation site (see Section 5.2.3), scaled by a constant factor f_b . For the covariance methods ‘Global’ and ‘Local’ the off-diagonal elements of \mathbf{B}^E were defined according to a spatial correlation, decaying exponentially with the distance between a grid cell pair and utilising a correlation length, L , which was set to 200 km for all inversions. Furthermore, the baseline mole fractions were assumed to be correlated temporally, described by an exponentially decaying relationship in the off-diagonal elements of \mathbf{B}^B , based on the temporal correlation length, τ_b , set to 5 days. For the covariance method ‘Stohl’, \mathbf{B} only contained values in the diagonal, implying uncorrelated a priori uncertainties. For all three approaches it was assured that the total by-region a priori uncertainty of emissions is the same as defined above.

The covariance matrix \mathbf{R} contains the uncertainty of the observations and the model (data-mismatch), $\sigma_c = \sqrt{\sigma_O^2 + \sigma_{model}^2}$. For the covariance methods ‘Global’ and ‘Local’ the diagonal elements of \mathbf{R} were defined as a combination of the observation uncertainty σ_O and the model uncertainties σ_{model} . σ_O contained the measurement uncertainty (see Section 5.2.2) and σ_{model} was calculated iteratively for each site, incorporating the root mean square error (RMSE) between an a priori simulation and the observed mole fractions. Off-diagonal elements of \mathbf{R} were assumed to follow an exponentially decaying structure [Henne, *et al.*, 2016]. The temporal correlation length, τ_c , of the combined uncertainty, σ_c , was based on the autocorrelation of the a priori model residuals. Two different approaches were followed to determine τ_c . First (method ‘Global’), a constant value of τ_c for the entire time period and each site was estimated fitting an exponential decay to the first two lags of the global autocorrelation function of the residuals. In a second approach (‘Local’), the autocorrelation was evaluated locally within moving windows with a half-width of 80 data points (10 days). Again τ_c was then calculated from an exponential fit to the first three values of the autocorrelation function for each window. These procedures to estimate τ_c worked successfully for all compounds and sites, except for HFC-143a at Finokalia, for which large, unexplained peaks in the observed time series lead to very large values in the autocorrelation function and consequently τ_c . To allow for a meaningful inverse adjustment, a constant τ_c was used for HFC-143a, based on the mean value of τ_c for the other compounds.

In the alternative approach (‘Stohl’) \mathbf{R} was specified similar to the above mentioned method, using the RMSE between a priori simulation and observations. In addition, the extreme values in the resi-

dual distribution were filtered and assigned larger uncertainties, in order to derive a more Gaussian distribution of the a priori residuals normalised by σ_C [Stohl, *et al.*, 2009]. As a result, a disproportional influence of extreme values, which were not resolved well by the transport model, can be avoided. Furthermore, off-diagonal elements in \mathbf{R} were set to zero in this approach.

5.2.8 Sensitivity Inversions

The a posteriori uncertainty, analytically estimated by a Bayesian inversion, often strongly depends on assumptions made on the a priori and data-mismatch uncertainty as well as on the general design of the inversion system. A number of previous studies have shown that this analytical uncertainty is often too small to realistically cover the real a posteriori uncertainty [e.g., Bergamaschi, *et al.*, 2015]. To further explore the range of this structural uncertainty of the inversion setup and test the robustness of the a posteriori results, a set of sensitivity inversions were performed (see Table 5.2).

Table 5.2: Setup for the base inversion (Base) and the sensitivity inversions (S-XX). Method refers to the uncertainty treatment explained in Section 5.2.7. The sites are abbreviated as follows: Finokalia (FKL), Jungfraujoch (JFJ), Mace Head (MHD) and Monte Cimone (CMN).

Inversion	Method	Sites	Prior emissions uncertainty scaling factor
BASE	Global	FKL, JFJ, MHD, CMN	1
S-ML	Local	FKL, JFJ, MHD, CMN	1
S-MS	Stohl	FKL, JFJ, MHD, CMN	1
S-UH	Global	FKL, JFJ, MHD, CMN	1.5
S-UL	Global	FKL, JFJ, MHD, CMN	0.5
S-NFKL	Global	JFJ, MHD, CMN	1
S-OFKL	Global	FKL	1

The inversion using the a priori emissions as described above, the ‘Global’ method for setting up the covariance matrices \mathbf{B} and \mathbf{R} , and observations from all four sites was chosen to represent the base inversion (BASE) setup. The base case does not necessarily offer the best inversion settings for each substance and each site, as these are generally not known, but serves as a starting point to assess the sensitivity of the inversion towards differently chosen parameters.

A first set of sensitivity inversions was used to analyse the effect of different covariance matrix designs. In contrast to the BASE inversion, S-ML and S-MS used the ‘Local’ and ‘Stohl’ approach as described in Section 5.2.7.

We then explored the sensitivity of our a posteriori results towards a priori emission uncertainties, with regard to the inhomogeneous availability of a priori information on halocarbon emissions within our inversion grid. To this end, the a priori uncertainty for each region was increased/decreased by 50 % as compared to the base uncertainty (S-UH, S-UL).

In a third set of sensitivity runs the influence of the additional observations gathered during the campaign at Finokalia on the a posteriori emissions in western Europe, central Europe and the Eastern Mediterranean was tested. One sensitivity inversion was set up, excluding the observations from Finokalia (S-NFKL), whereas in a second inversion, only measurements from Finokalia were taken into account (S-OFKL). Using this approach, two questions can be answered. First, what is the gain of the Finokalia observations for top-down emission estimation in the Eastern Mediterranean and, second, did the inclusion of the additional AGAGE sites provide substantial constraints for the same area?

5.3 Results and Discussion

In this section an overview about the measurements taken in Finokalia (FKL) is followed by a comprehensive presentation and discussion of the inversion results. The performance of the BASE inversion is shown exemplarily for HFC-134a in more detail before the results of the sensitivity inversions are presented, highlighting the differences between the BASE case and these inversions. The “top-down” emission estimates for defined regions within the inversion domain are shown in the last section.

5.3.1 Flow Regime and Observations at Finokalia

During our measurement campaign from December 2012 to August 2013, local wind observations showed a transition from a northerly wind regime in December to a more variable wind regime with a bias towards westerly directions from January to June. July and August were characterized by very constant easterly to north-easterly winds. These local observations agree with the results of the atmospheric transport simulations, showing air transported to the station from the African continent and the Western Mediterranean in February and March (Figure 5.2a). The area of influence changes more towards South-eastern Europe in early summer, whereas in July and August, air is transported from a narrowly defined north-easterly sector (Figure 5.2b).

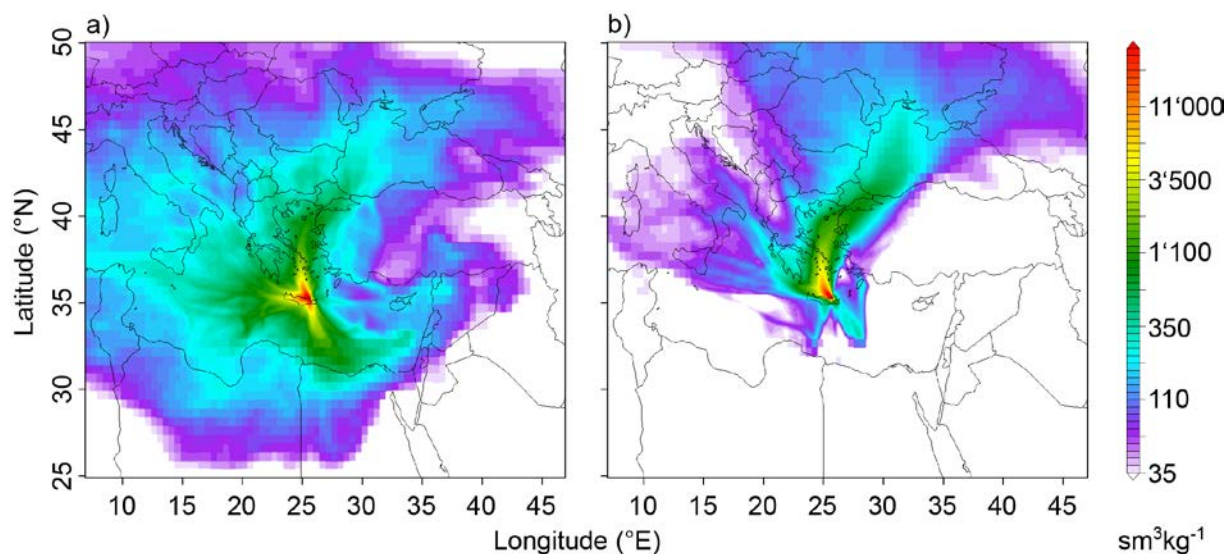


Figure 5.2: Average FLEXPART derived source sensitivities for Finokalia and two characteristic flow regimes during the measurement campaign: a) shows the variable flow during winter and spring and b) northeasterly flow during the summer months.

These conditions observed during the campaign in 2012/2013 agree with previous descriptions of the wind climatology at FKL, that also observed two distinct meteorological regimes in Crete. During the dry season from May to September, air masses are usually advected from central and eastern Europe and the Balkans, whereas the wet season from October to April is more variable in terms of air transport and favours air masses from the African continent and from marine influenced westerly sectors [Kouvarakis, *et al.*, 2000; Gerasopoulos, *et al.*, 2005]. Therefore, the halocarbon observations presented here can be expected to be the result of typical advection conditions at FKL.

The halocarbon observations collected at FKL during the campaign are shown in Figure 5.3, together with data from JFJ and CMN for comparison. The range of the observations at FKL and the temporal evolution of the atmospheric baseline signals agreed well between the sites.

For HFC-134a and HFC-125, which are mainly used as refrigerants in mobile and stationary air conditioning, the maximum measured mole fractions and the variability at FKL was smaller than what was simultaneously measured at the two other stations. This could be expected from the maritime influence at FKL, with the closest larger metropolitan areas at a distance of 350-700 km, as compared to nearby emission hot-spots for JFJ and CMN (e.g., Po Valley). For HFC-143a, pollution peaks were comparable to the measurements at CMN during a short period in the beginning of the campaign (Dec - Feb). After this period, the variability decreased with no more large pollution peaks observed. HFC-152a and HCFC-22 observations showed a similar pattern at FKL as at the other sites. Particularly high mole fractions during several pollution periods were observed for HCFC-22, indicating the proximity of emissions possibly from Article 5 countries, where the use of

HCFCs has just recently been capped. Although the highest observed mole fractions were relatively large, they occurred less frequently than those observed at JFJ and CMN. This was probably due to distant but strong pollution sources influencing the observations at FKL. HCFC-142b mole fractions showed large variability and comparably large peak mole fractions during the summer period at FKL, but again with a slightly lower frequency than at JFJ.

The mean baseline values at FKL for HFC-134a, HFC-125, HCFC-22 and HCFC-142b, calculated with the REBS method [Ruckstuhl, *et al.*, 2012], were within a range of ± 7 % of the baseline values derived for the other three sites (see Table 5.1). Maximum baseline deviations of ± 13 % were estimated for HFC-143a and HFC-152a as compared with JFJ.

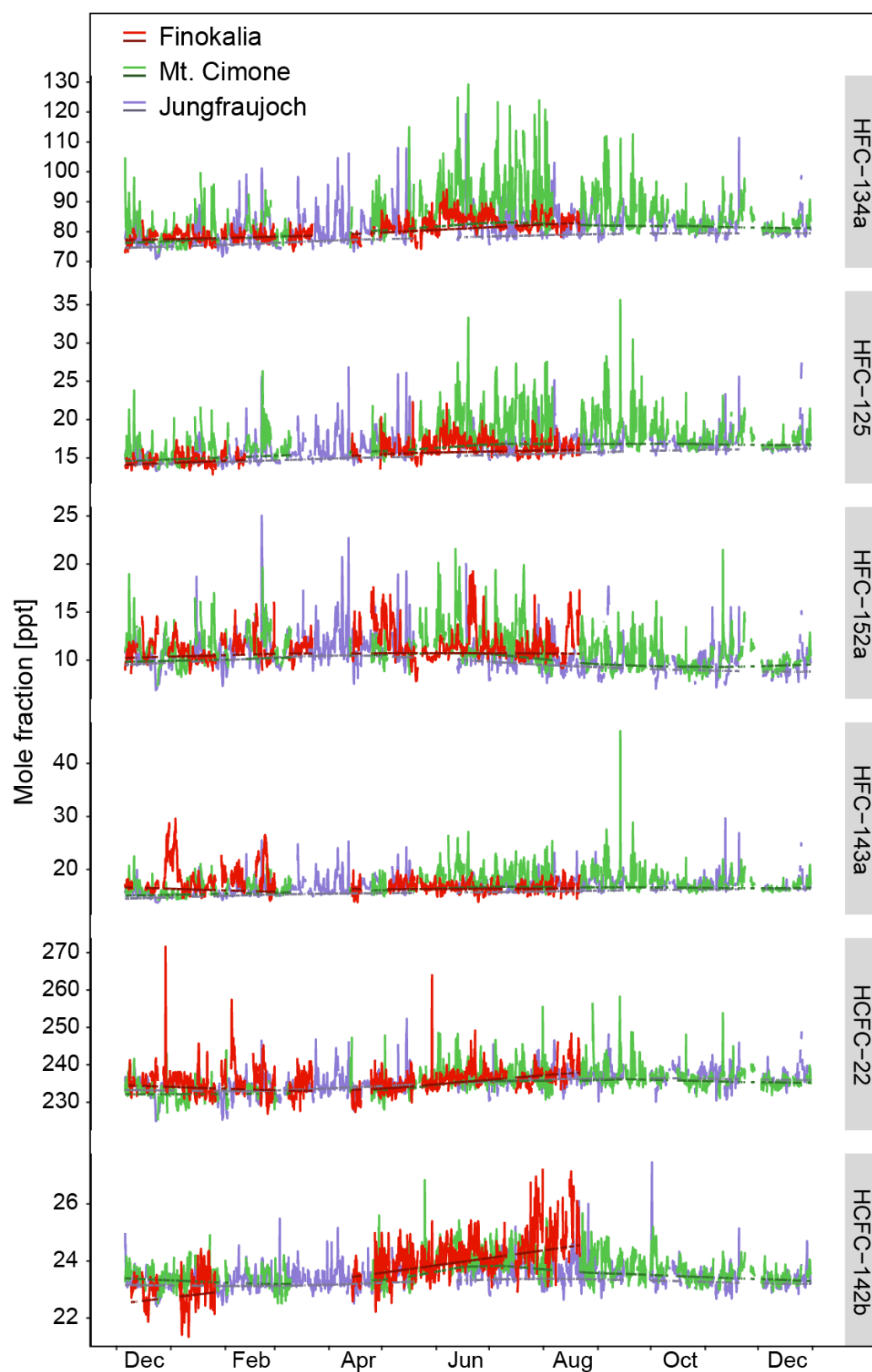


Figure 5.3: Halocarbon observations in 2013, during the time of the measurement campaign in Finokalia (red) and simultaneous measurements at Jungfraujoch (purple) and Monte Cimone (green). The corresponding background estimated with REBS is shown in the darker shade of the respective color.

5.3.2 Base Inversion

For the BASE inversion, the covariance design based on the ‘Global’ autocorrelation function, as described in Section 5.2.7, was used, combined with the complete set of observations from all four sites, including the observations from FKL. Exemplarily, a comparison of simulated prior and posterior HFC-134a with the underlying observations is shown in Figure 5.4. At all four sites the simulated a priori mole fractions reproduced the variability of the observations, indicating satisfactory performance of the transport model. Simulations of the a priori mole fractions showed a tendency to underestimate the observations during peak periods at JFJ, MHD, and CMN, whereas the a priori simulation generally overestimated the observations at FKL. Here, a similar behaviour of the a priori simulations was also observed for HFC-152a, whereas the tendency to underestimate the observations (like at the AGAGE sites) was apparent for all other analysed compounds. Since FKL and the AGAGE sites are mostly sensitive to distinctly different regions, the general overestimation in the prior simulations already points towards generally overestimated or spatially misallocated a priori emissions in the Eastern Mediterranean.

For all four stations, the inversion considerably improved the correlation between observations and simulations, which was evaluated based on the coefficient of determination R^2 . The performance of the simulated a posteriori signal increased to $R^2 = 0.74$ for FKL and MHD, 0.5 for JFJ and 0.54 for CMN, which corresponds to an improvement of R^2 by $\Delta R^2 = 0.33$ for FKL, $\Delta R^2 = 0.13$ for MHD, $\Delta R^2 = 0.17$ for JFJ and $\Delta R^2 = 0.15$ for CMN (Table 5.3). Only accounting for the simulated and observed signal above the baseline, the performance was lower for FKL ($R^2 = 0.29$), JFJ ($R^2 = 0.34$) and CMN ($R^2 = 0.28$). The correlation of the signal above the baseline for MHD ($R^2 = 0.73$) remains as high as for the complete signal. These values indicate good inversion performance results and are comparable to other studies, using similar inversion schemes [Stohl, *et al.*, 2009; Vollmer, *et al.*, 2009; Keller, *et al.*, 2012]. The performance ranking between the sites and the large above baseline correlation at MHD also agree with our expectations. The latter is due to the coastal location of MHD with negligible emissions west of the site for several thousand kilometres across the Atlantic Ocean and the fact that synoptic scale flow, which is well captured by the transport model, intermittently drives European emissions towards the site. In contrast, transport to JFJ and CMN is driven by small scale flow systems and baseline conditions are generally less well-defined in free tropospheric conditions that tend to be more variable. Finally, while FKL is a coastal site like MHD, it does not exhibit a well-defined baseline sector, since emission sources may be found at the entire coastline in the Eastern Mediterranean at distances around 1000 km from the site.

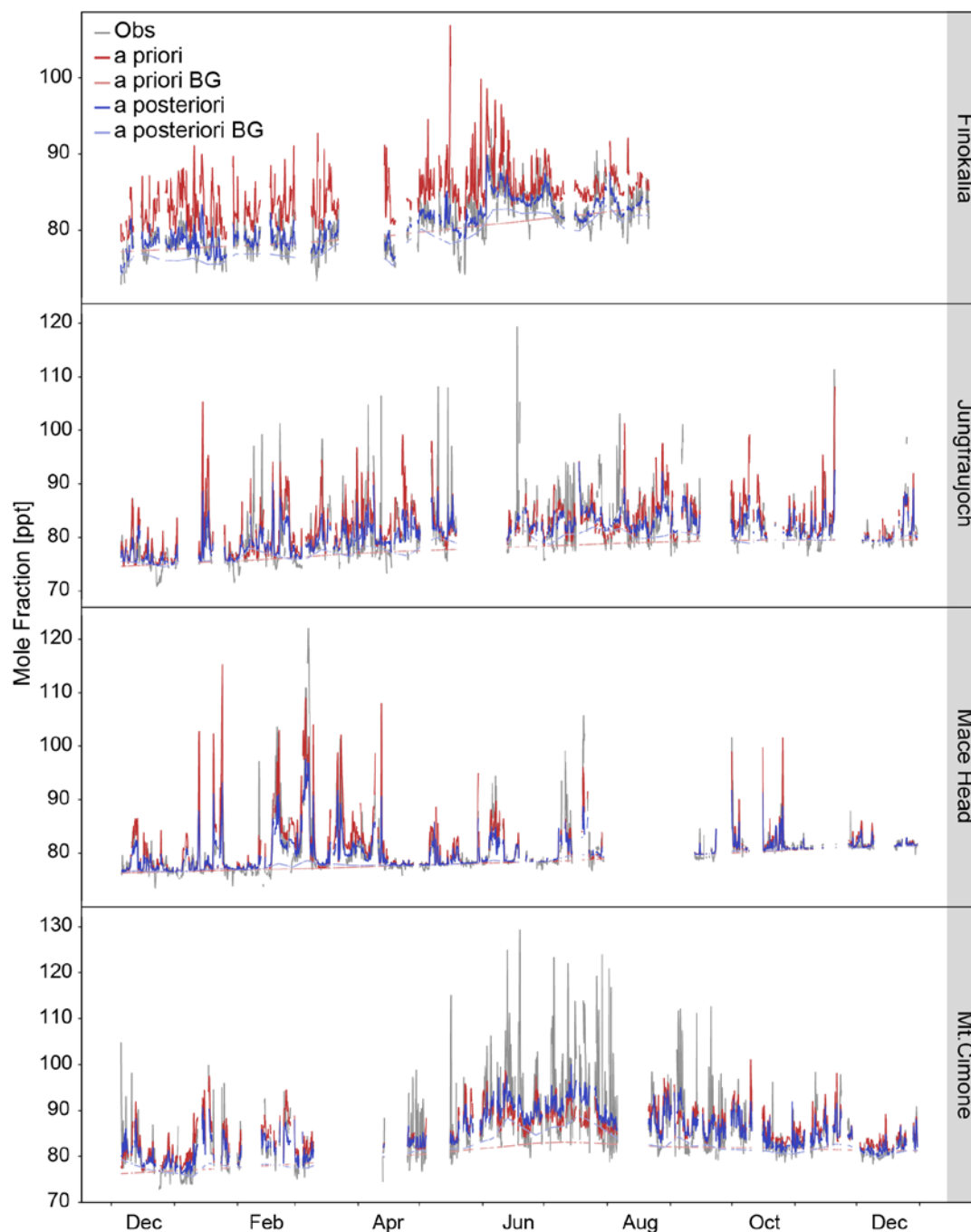


Figure 5.4: HFC-134a time series of the base inversion for 2013, showing the observed mole fractions at the respective sites (grey) and the simulated values (a priori: red; a posteriori: blue) and their baseline conditions (a priori: light red; a posteriori: light blue).

To evaluate the ability of the model to simulate the observed amplitudes correctly, we used the Taylor skill score (TSS), combining correlation and variability of observed and simulated mole fractions [Taylor, 2001]. The maximum attainable Pearson correlation coefficient, indicating a “perfect” simulation in terms of the strength of the relationship between simulated values and observations was set to 0.9. Thus a TSS of 1 indicates a perfect simulation with regards to amplitude and correlation, whereas a TSS of 0.65 means that the observed variability is under/overestimated by a factor of 2 for perfectly correlated simulations. Although the normalized standard deviation decreased for

FKL, the TSS was increased to 0.95 due to the improvement of the correlation of posterior results and observations, indicating, that although the relationship of observations and simulations was increased, the inversion did not adjust the amplitudes of the pollution peaks. At CMN the a posteriori TSS increased to 0.74, driven by both, an increase of the normalised standard deviation and correlation, whereas the TSS for JFJ and MHD decreased to 0.71 and 0.75 respectively. The latter is due to a reduction of simulated peak heights compared to the a priori simulation, while the correlation was strongly improved. In general, the resulting Taylor skill scores were in a similar range as in previous regional-scale inversion studies [Brunner, *et al.*, 2016; Henne, *et al.*, 2016].

Model and inversion performance were also evaluated using the Root-Mean-Square-Error (RMSE; a combined measure of variability and bias) between simulated and observed mole fractions. Its reduction from a priori to a posteriori simulations amounted to 20%, 12% and 10% for JFJ, MHD and CMN, respectively. The absolute a posteriori RMSE was in the range of 2.9 – 5 ppt for these sites. The RMSE improvement for FKL from the a priori RMSE (4.7 ppt) to the a posteriori RMSE (1.7 ppt) was much larger (64%). This can be attributed to the above mentioned overestimation of the simulated prior values and the optimisation by the inversion, which also included a considerable reduction of the baseline. Again, these RMSE reductions were in a similar range as those reported in previous studies [Stohl, *et al.*, 2009; Vollmer, *et al.*, 2009; Keller, *et al.*, 2012].

The inversion performance of HFC-125 and HCFC-142b was similar to HFC-134a, with mean posterior TSS of 0.81 and 0.78, respectively, compared to 0.78 for HFC-134a. For HFC-152a, HFC-143a and HCFC-22 they decreased to 0.73, 0.74 and 0.75, respectively (Table 5.3).

For the BASE inversion of the exemplary compound HFC-134a a posteriori were mostly smaller than a priori emissions with the exception of areas in Northern Italy, Slovenia, Croatia and along the western part of the British Channel (Figure 5.5a). Most pronounced emission differences in the Eastern Mediterranean were associated with the larger urban centres in Greece and Turkey (Athens, Thessaloniki, Istanbul), whereas in Western and Central Europe similarly large reductions were assigned to the Benelux area and the western part of Germany as well as to the UK. Within the same BASE inversion of HFC-134a the analytic uncertainty in the Eastern Mediterranean was reduced by more than 80% from its prior value for grid cells containing large metropolitan areas such as Athens and even Cairo (Figure 5.5b). For Western Turkey and large parts of the Balkans, the uncertainty was reduced by 30-60%, which shows, that we achieve satisfactory emission estimates for the targeted areas in the Eastern Mediterranean. Similar reductions are also achieved over large parts of Western and Central Europe, to which the AGAGE sites are sensitive. Although other adjacent

areas such as Middle Eastern countries bordering the Mediterranean Sea (e.g., Israel, Jordan) and countries further Northeast (e.g., Ukraine) were detected during our measurement campaign, the uncertainty was reduced less by the inversion (10-30%).

Table 5.3: Inversion performance of the BASE inversion at Finokalia (FKL), Jungfraujoch (JFJ), Mace Head (MHD) and Monte Cimone (CMN). N is the number of observations used for the inversion. RMSE, R^2 and TSS denote the root mean square error, coefficient of determination and the Taylor skill score of the complete signal and R^2_{abg} is the coefficient of determination of the signal above background.

	Site	N	RMSE (ppt)		R^2		R^2_{abg}		TSS	
			apriori	apost	prior	post	prior	post	prior	post
HFC-134a	FKL	1421	4.7	1.7	0.41	0.74	0.20	0.29	0.86	0.95
	JFJ	1946	4.5	3.6	0.33	0.50	0.25	0.34	0.82	0.71
	MHD	2005	3.3	2.9	0.61	0.74	0.61	0.73	0.93	0.75
	CMN	1801	5.8	5.1	0.39	0.54	0.25	0.28	0.62	0.74
HFC-125	FKL	1147	1.4	0.8	0.31	0.59	0.12	0.16	0.81	0.88
	JFJ	1938	1.2	1.2	0.45	0.54	0.34	0.40	0.79	0.74
	MHD	1975	1.0	0.8	0.63	0.74	0.62	0.71	0.88	0.89
	CMN	1840	1.8	1.6	0.42	0.53	0.29	0.32	0.62	0.76
HFC-152a	FKL	1428	4.0	1.2	0.00	0.43	0.00	0.11	0.39	0.62
	JFJ	1960	1.4	1.3	0.36	0.49	0.21	0.31	0.59	0.65
	MHD	2011	0.7	0.5	0.54	0.72	0.26	0.38	0.89	0.90
	CMN	1864	1.5	1.3	0.33	0.55	0.19	0.29	0.54	0.74
HFC-143a	FKL	1252	2.3	1.6	0.06	0.53	0.01	0.03	0.26	0.67
	JFJ	1973	1.2	1.1	0.43	0.48	0.36	0.38	0.83	0.70
	MHD	2052	1.1	0.9	0.63	0.72	0.65	0.71	0.79	0.85
	CMN	1814	1.5	1.4	0.41	0.48	0.31	0.31	0.74	0.72
HCFC-22	FKL	1426	3.7	2.7	0.15	0.42	0.05	0.15	0.52	0.62
	JFJ	1953	2.8	2.1	0.31	0.50	0.14	0.23	0.77	0.73
	MHD	1994	1.8	1.3	0.41	0.65	0.26	0.36	0.84	0.89
	CMN	1728	3.0	2.3	0.35	0.50	0.15	0.19	0.76	0.76
HCFC-142b	FKL	1065	0.6	0.5	0.52	0.64	0.00	0.02	0.79	0.87
	JFJ	1960	0.4	0.3	0.24	0.39	0.12	0.15	0.36	0.62
	MHD	2042	0.2	0.1	0.42	0.66	0.36	0.52	0.64	0.84
	CMN	1802	0.4	0.3	0.48	0.56	0.21	0.19	0.57	0.82

Similar patterns of uncertainty reduction resulted for HFC-152a, HFC-125, HCFC-22 and HCFC-142b. For HCFC-142b the reduction was lower for the Balkans (~ 10%), but similarly large for Western Turkey (20-40%). For HFC-143a, the uncertainty was reduced by 20 % for the area of Athens, whereas only negligible reductions were estimated for Turkey.

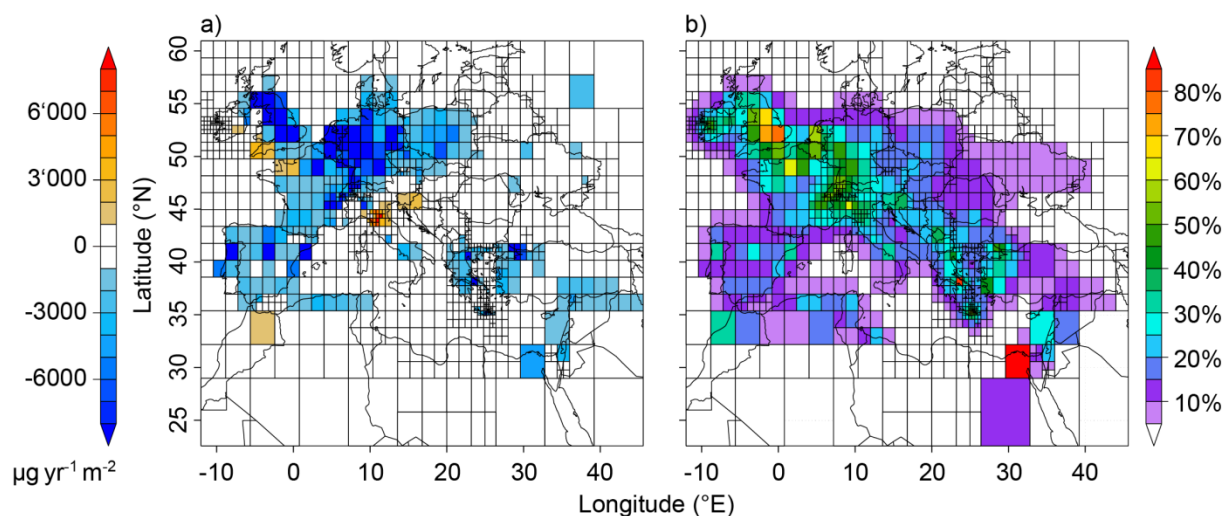


Figure 5.5: a) Emissions difference (posterior – prior) of the BASE inversion of HFC-134a. b) Relative reduction of the a posteriori uncertainty compared to the a priori uncertainties.

5.3.3 Sensitivity Inversions

Influence of Covariance Design

The first sensitivity inversion, S-ML, uses the ‘Local’ approach to estimate the temporal correlation length scale of the data-mismatch uncertainty (see Section 5.2.7). As a consequence, the weights different observations were given in the inversion were slightly redistributed as compared with the BASE inversion. For our exemplary compound HFC-134a, the model performance in terms of the RMSE was similar to the BASE inversion at FKL, CMN and JFJ. For MHD the RMSE was not reduced by the inversion, thus compared to the base inversion, posterior RMSE values were 14% higher. The same pattern was observed for the coefficient of determination R^2 , which was increased by less than 2% for FKL, CMN and JFJ, but dropped by approximately 8% at MHD. Despite the slight increase in the correlation at FKL, CMN and JFJ, the Taylor Skill Score decreased between 1-4%, indicating that in the S-ML case, the peak amplitudes are not as well simulated than in our BASE inversion. For MHD, the TSS was reduced by 12%, reflecting that in addition to the lower correlation, S-ML also underestimated the peak amplitudes at this coastal location.

The sensitivity case S-MS used uncorrelated a priori and data-mismatch uncertainties (see Section 5.2.7). As opposed to S-ML, the RMSE of S-MS for HFC-134a was improved by 14%, 6% and 2% at MHD, JFJ and CMN respectively, as compared with the BASE inversion, whereas no improvement was observed for FKL, which showed a small RMSE of 1.7 ppt in the BASE inversion al-

ready (Table 5.4). R^2 was generally higher for S-MS compared to the BASE inversion. It increased between 1-3% for FKL, CMN and MHD and by 6% for JFJ, showing the best absolute performance for MHD and FKL in the posterior R^2 , with 0.76 and 0.75, respectively. As indicated by higher Taylor skill scores (Table 5.4), S-MS was also able to more closely reproduce the amplitude of the peaks at all sites as compared to the BASE inversion.

Table 5.4: Inversion performance of the base inversion and the sensitivity inversions S-ML and S-MS for HFC-134a at Finokalia (FKL), Jungfraujoch (JFJ), Mace Head (MHD) and Monte Cimone (CMN). N is the number of observations used for the inversion. RMSE is the root mean square error in ppt (parts per billion 10^{-12}). R^2 denotes the coefficient of determination of the complete signals and R^2_{abg} is the coefficient of determination of the signals above background. TSS shows the Taylor Skill Score of the entire signal.

	Site	N	RMSE		R^2		R^2_{abg}		TSS	
			apriori	apost	prior	post	prior	post	prior	post
Base	FKL	1421	4.7	1.7	0.41	0.74	0.20	0.29	0.86	0.95
	JFJ	1946	4.5	3.6	0.33	0.50	0.25	0.34	0.82	0.71
	MHD	2005	3.3	2.9	0.61	0.74	0.61	0.73	0.93	0.75
	CMN	1801	5.8	5.1	0.39	0.54	0.25	0.28	0.62	0.74
S-ML	FKL	1421	4.7	1.7	0.41	0.75	0.20	0.28	0.86	0.95
	JFJ	1946	4.5	3.6	0.33	0.50	0.25	0.32	0.82	0.68
	MHD	2005	3.3	3.3	0.61	0.68	0.61	0.68	0.93	0.66
	CMN	1801	5.8	5.1	0.39	0.55	0.25	0.28	0.62	0.73
S-MS	FKL	1421	4.7	1.7	0.41	0.75	0.20	0.36	0.86	0.97
	JFJ	1946	4.5	3.4	0.33	0.53	0.25	0.4	0.82	0.80
	MHD	2005	3.3	2.5	0.61	0.76	0.61	0.75	0.93	0.90
	CMN	1801	5.8	5.0	0.39	0.55	0.25	0.31	0.62	0.78

Total HFC-134a emissions for the whole inversion domain were 10% lower for the S-ML case, whereas they were 30% higher for S-MS, as compared to the BASE inversion. While regional emissions from Greece and the Balkans were relatively unaffected in the S-ML case, more pronounced negative deviations compared to BASE were established for Turkey (-14%), Central W (FR, LU, NL, BE; -23%) and the Iberian Peninsula (ESP, PT; -22%) (Figure 5.5 and Figure 5.6b,c). A posteriori differences were less smooth in the S-MS inversion as compared to the BASE and S-ML inversions (Figure 5.6b), reflecting the effect of not using a spatial correlation in the a priori emissions. Regional emissions estimated with S-MS were generally higher as compared to the base inversion (Figure 5.6c). Significantly (40%, $p < 0.05$) higher emissions were obtained in the UK and Ireland, compared to the BASE inversion. Regional emissions of North-Western Europe and the Balkans were larger by 20-60% in S-MS.

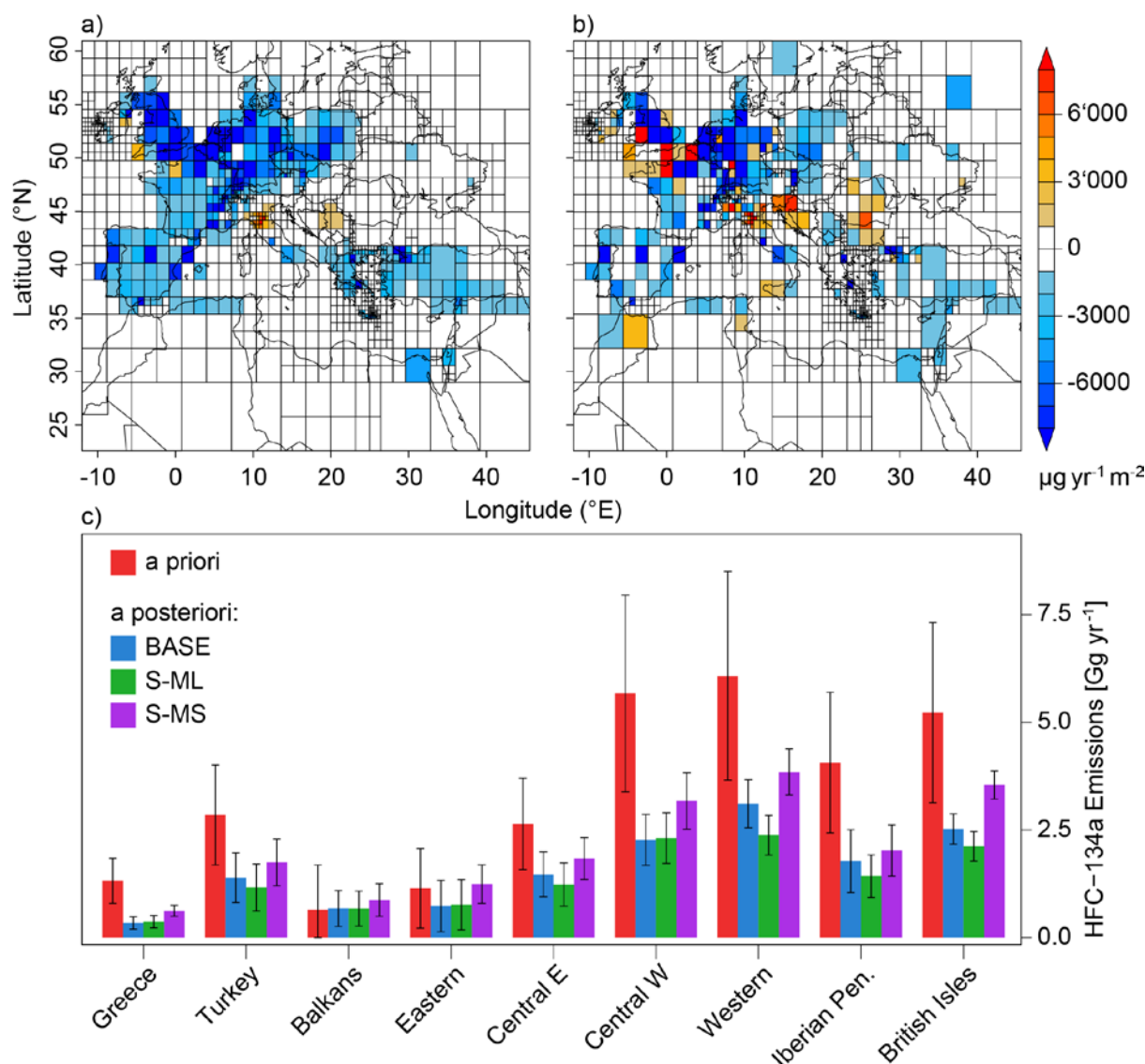


Figure 5.6: Difference of the a posteriori and a priori emissions for (a) the S-ML and (b) the S-MS inversions of HFC-134a. (c) regional emission estimates: a priori emissions (red) and a posteriori emissions (BASE = green, S-ML = blue, S-MS = purple). The uncertainties given are two standard deviations of the analytic uncertainty assigned to the a priori emissions and derived by the inversion as a posteriori uncertainties.

In summary, S-ML showed a slightly weaker performance than the BASE inversion, with insignificantly lower total emission estimates but similar analytic uncertainties. On a regional level, the impact of S-ML on the estimated emissions varies by region, showing less influence on the Balkans and Central W, whereas larger deviations were seen for Turkey, Western and the British Isles. On the contrary, S-MS performed slightly better and resulted in generally larger emissions than the BASE inversion, but confirmed the significant emission reductions as compared to the a priori emissions.

Influence of A priori Uncertainty

To assess the influence of our regionally assigned a priori uncertainties, the sensitivity inversions S-UL and S-UH were run with 50% smaller and larger a priori emission uncertainties as compared to

the base inversion. As expected, a posteriori model performance generally increased with larger a priori uncertainties because the optimisation is less constrained by the prior. However, HFC-134a domain total a posteriori emissions remained similar to those in the BASE inversion, whereas S-UL resulted in slightly increased emission estimates, remaining closer to the prior emissions (see supplement). A posteriori HFC-134a emission uncertainties were decreased (increased) by $\sim 28\%$ and $\sim 16\%$ in comparison to the BASE inversion, if a priori emission uncertainties were smaller and larger, respectively (Figure 5.7).

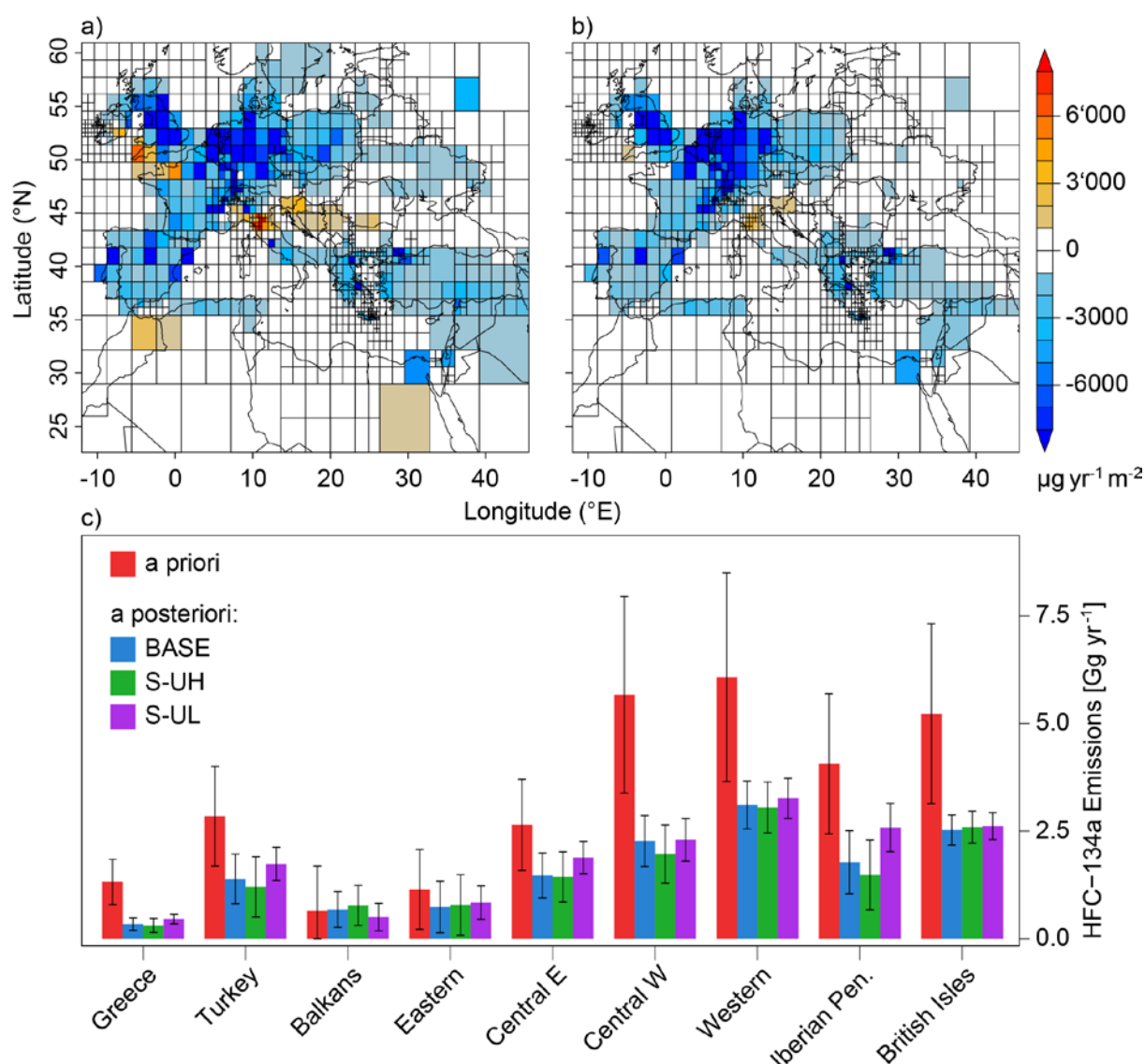


Figure 5.7: Difference of the a posteriori and a priori emissions for (a) the S-UH and (b) the S-UL inversions. (c) regional emission estimates: a priori emissions (red) and a posteriori emissions (BASE = green, S-UH = blue, S-UL = purple). The uncertainties given are two standard deviations of the analytic uncertainty assigned to the a priori emissions and derived by the inversion as a posteriori uncertainties.

In general, the absolute emission estimates for the study domain seemed to be very robust to changes in the a priori uncertainty. A posteriori emission estimates for the case with lower a priori uncertainties (S-UL), comprising all the analysed species except HFC-134a, showed insignificantly

larger total emissions. This reflects the constraint, which requires the results to follow the a priori emissions more closely in this case. Total a posteriori emissions in the case of larger a priori emission uncertainties remained close to our BASE case. Emission uncertainties in the a posteriori, as compared to the BASE inversion, were on average about 18% higher and 27 % lower for the S-UH case and the S-UL case, respectively. This tendency can be expected from the a priori emission uncertainties. The results of these two sensitivity inversions emphasize the general robustness of the inversion system to changes in the a priori emission uncertainties. Exceptions in the case of HFC-134a are discussed in the following section.

5.3.4 Regional Total Emissions

Our estimated regional total emissions are summarized in Table 5.5 and Figure 5.8. The “top-down” emission estimates presented here are the mean values of the BASE and four sensitivity inversions (S-ML, S-MS, S-UH, S-UL). The uncertainty range given here and in Table 5.5 represents the range of these five inversions based on their mean values and the analytical a posteriori uncertainty (95% confidence interval), whichever is larger. This measure was chosen to accommodate, on the one hand, the analytical uncertainty as estimated by the Bayesian formulation and estimated for each inversion run as the a posteriori uncertainty, and, on the other hand, the structural uncertainty that is reflected by the spread of the sensitivity inversions and results from choices in the parameter selection of the covariance design. The comparison between structural and analytic uncertainties reveals that the dominating type of uncertainty varies largely between different compounds and different regions. For most compounds and regions the two types of uncertainty fall within a similar range (HFC-152a; HFC-143a; HFC-125; HCFC-22; HFC-134a only in the eastern part of the domain). For HCFC-142b the structural uncertainty was generally smaller than the average a posteriori uncertainty. In contrast, for HFC-134a and the western part of the domain (British Isles, Iberian Peninsula, Western, Central W) the structural uncertainty was clearly larger than the analytical uncertainty.

This relatively large spread in the sensitivity inversions results from the differences between the sensitivity inversions with different covariance matrices (S-ML and S-MS), where a general tendency to smaller changes from the a priori (resulting in larger a posteriori emission) was observed for the western part of the domain and for Turkey. In addition, a similar tendency was observed for the same regions, except the Western region, when different a priori uncertainties were applied (S-UH, S-UL, Figure 5.7). Therefore, combining the results from all sensitivity inversions revealed relatively large uncertainties in the “top-down” estimates in a region that is relatively well covered

by the existing AGAGE network and emphasizes the use of such sensitivity tests to explore the real uncertainty of the “top-down” process and the need for more objective methods to derive the data-mismatch covariance matrix.

HCFCs

HCFC-22 is the most abundant HCFC in today’s atmosphere and has been widely used as a refrigerant and foam blowing agent in much larger quantities than other HCFCs. Due to regulations by the Montreal Protocol, global emissions have remained constant since 2007 [Carpenter and Reimann, 2014]. Our “top-down” emission estimate for the regions listed in Table 5.5 (in the following referred to as total emissions) amounted to 9.1 (4.5-14) Gg yr⁻¹. As expected, high emissions were concentrated in regions, defined by the Montreal Protocol as developing (Article 5) countries, such as Egypt, the Middle East and Turkey, accounting for 43% (22-67%) of the total emissions. Our estimates for Central and Western European (regions Western, Central W, British Isles, Iberian Peninsula and Italy) emissions are 3.1 (2.0-4.3) Gg yr⁻¹, which is 69% (57-81%) less than reported by Keller *et al.* [2012] for the same area in 2009, suggesting that HCFC-22 emissions continue to decrease in these developed countries. However, major pollution events were observed at FKL when air arrived from areas such as Egypt, which may be explained by the fact that caps to HCFC production and consumption for Article 5 parties began only in 2013. For the total domain, our a posteriori estimates were significantly lower than the a priori values. On the regional scale, a posteriori estimates were larger than a priori for the above mentioned Article-5 countries (Egypt, Middle East), whereas this tendency was inversed for Non-Article 5 countries. These results agree with the expectation that due to the stepwise phase out of HCFCs in developing countries and the inherent time lag until release to the atmosphere [Montzka, *et al.*, 2015], HCFC-22 emissions remain at considerably high levels.

HCFC-142b is applied mainly as a foam blowing agent for extruded polystyrene boards and as a replacement for CFC-12 in refrigeration applications [Derwent, *et al.*, 2007]. Our total estimated emissions sum up to 1.0 (0.5-1.6) Gg yr⁻¹. Turkey, listed as an Article 5 party, accounts for 13.8% (4.7-23.0%) of these total emissions, whereas the contribution of other Article 5 regions is less pronounced as compared to HCFC-22. Average a posteriori emissions in the Eastern Mediterranean (regions Greece, Turkey, Middle East, Egypt, Balkans and Eastern) are estimated to 0.40 (0.09-0.74) Gg yr⁻¹, which is about half of the domain total emissions. However, our inversion was not able to significantly reduce the uncertainty estimate for these regions, demonstrating the need for additional and continuous halocarbon measurements in this area. HCFC-142b emissions in Central

and Western Europe, where the use of HCFCs has practically been phased out, show a comparatively large contribution of 0.53 (0.39-0.67) Gg yr⁻¹, which accounts for 39.7% (31.3-48.5%) of the domain total emissions. Although the spatial distribution of HCFC-142b emissions in Central Europe resembles the pattern derived by *Keller et al.* [2012], dating back to emissions from 2009, our estimates indicate a reduction by a factor of ~2. Our estimates are also lower by the same factor ~2 compared to bottom-up estimates of HCFC-142b emissions, as reported in EDGARv42 [JRC/PBL, 2009] for the year 2008, for both Western Europe and the Eastern Mediterranean. However, the latter is mainly driven by generally smaller emissions in the Eastern and Balkan regions, whereas for Turkey, the Middle East and Egypt larger than EDGAR values were estimated by the inversion. The general decrease within the domain is in line with global emissions of HCFC-142b, which are considerably lower than those of HCFC-22 and have declined by 27%, from 39 (34-44) Gg yr⁻¹ to 29 (23-34) Gg yr⁻¹ between 2008 and 2012 [Carpenter and Reimann, 2014; Montzka, et al., 2015]. The comparison of a priori and a posteriori emissions of HCFC-142b shows a much more diversified pattern than for HCFC-22, with regions such as Turkey and Western, where our bottom-up assumptions were too low, whereas they were too high for Maghreb and Egypt and agreed well for Italy, Greece and Central W.

HFCs

HFC-134a is currently the preferred refrigerant in mobile air conditioning systems and, together with HFC-125, which is mostly used in refrigerant blends for residential and commercial refrigeration, belongs to the two most popular HFCs in Europe [O'Doherty, et al., 2004; O'Doherty, et al., 2009; Velders, et al., 2009; Xiang, et al., 2014]. This is reflected by the large amplitude and frequency of pollution peaks, which were observed at all continuous observations sites but especially at JFJ and CMN (Figure 5.3). Total simulated HFC-134a emissions for our analysed regions were 19.0 (13.3-25.8) Gg yr⁻¹. Emissions from Eastern Mediterranean (Greece, Turkey, Balkans, Eastern, Middle East, Egypt) summed up to 4.6 (2.5-6.9) Gg yr⁻¹, which is ~24% of the domain total emission. The remaining 63% were emitted from Central and Western Europe, totalling at 11.9 (9.4-15.2) Gg yr⁻¹. Comparing the aggregated emissions of reporting regions to UNFCCC inventories reveals, that the inversion generally estimated a posteriori emissions of HFC-134a that were 47.5% (32.0-60.3%) lower than the respective UNFCCC reports. Only HFC-134a emissions of Italy and Eastern European countries were within the range of reported UNFCCC estimates. Furthermore, our results suggest lower emission in most regions in comparison to EDGARv42_FT2010 [JRC/PBL, 2009] for the year 2010, with the exception of Greece, Turkey and the Eastern region, where both

estimates are very similar, and of Egypt and the Maghreb region, where the inversely estimated emissions were considerably larger than EDGAR values.

Table 5.5: Regional emissions as estimated in the a priori inventory and by the atmospheric inversion. All values are given in in Mg yr⁻¹. A posteriori estimates are shown as the mean values, derived from the BASE inversion and the sensitivity inversions S-ML, S-MS, S-UH and S-UL. The uncertainty range gives the maximum range provided by the respective mean values of all inversions plus the mean of the analytic uncertainty ($p < 0.05$) estimated by each individual inversion. Smaller and distant countries were aggregated to larger regions: Turkey (Turkey, Cyprus), Balkans (Serbia, Montenegro, Kosovo, Albania, Bosnia and Herzegovina, Croatia, Slovenia, Macedonia), Eastern (Ukraine, Romania, Moldova, Bulgaria), Middle East (Jordan, Lebanon, Syria, Palestine, Israel), Maghreb (Morocco, Algeria, Tunisia, Libya), Central E (Poland, Slovakia, Czech-Republic, Hungary), Central W (Switzerland, Liechtenstein, Germany, Austria, Denmark), Western (France, Luxembourg, Netherlands, Belgium), Iberian Peninsula (Spain, Portugal), British Isles (Ireland, United Kingdom).

	HFC-134a (CH ₂ FCF ₃)		HFC-125 (C ₂ HF ₅)		HFC-152a (C ₂ H ₄ F ₂)	
	Prior	Post	Prior	Post	Prior	Post
Greece	1.32±0.26	0.42 (0.31-0.63)	0.6 ±0.12	0.25 (0.19-0.31)	1.22±0.49	0.27 (0.21-0.37)
Turkey	2.85±0.58	1.45 (1.00-1.90)	0.12±0.03	0.11 (0.07-0.15)	1.11±0.78	0.62 (0.38-1.05)
Balkans	0.65±0.52	0.70 (0.37-1.03)	0.12±0.1	0.18 (0.08-0.29)	0.15±0.15	0.17 (0.10-0.35)
Eastern	1.15±0.46	0.88 (0.43-1.32)	0.34±0.14	0.32 (0.14-0.49)	0.41±0.29	0.21 (0.05-0.36)
Middle East	0.65±0.64	0.21 (0.00-0.61)	0.14±0.14	0.16 (0.00-0.37)	0.23±0.22	0.19 (0.02-0.35)
Egypt	1.14±1.14	0.94 (0.44-1.43)	0.28±0.28	0.21 (0.01-0.41)	0.46±0.46	0.09 (0.00-0.27)
Maghreb	1.18±1.17	0.89 (0.16-1.62)	0.3 ±0.3	0.39 (0.10-0.68)	0.47±0.47	0.18 (0.05-0.31)
Central E	2.64±0.53	1.57 (1.17-1.98)	1.1 ±0.22	0.76 (0.58-0.94)	0.41±0.16	0.23 (0.14-0.32)
Central W	5.67±1.14	2.40 (1.91-3.18)	0.95±0.19	0.70 (0.55-0.90)	0.38±0.2	0.26 (0.18-0.37)
Western	6.08±1.21	3.13 (2.38-3.84)	1.92±0.38	1.41 (1.24-1.58)	0.44±0.17	0.29 (0.23-0.37)
Italy	1.96±0.39	1.87 (1.64-2.09)	1.06±0.21	1.05 (0.94-1.17)	0.32±0.31	0.26 (0.19-0.32)
Iberian Pen.	4.06±0.82	1.86 (1.33-2.58)	2.03±0.41	1.52 (1.26-1.77)	0.32±0.13	0.16 (0.07-0.25)
British Isles	5.24±1.04	2.68 (2.12-3.54)	1.49±0.3	1.10 (0.99-1.20)	0.21±0.08	0.09 (0.06-0.13)
Domain Total	34.58±9.91	18.99 (31.26-25.76)	10.45±2.81	8.15 (6.15-10.26)	6.12±3.92	2.91 (1.48-4.76)
	HFC-143a (C ₂ H ₃ F ₃)		HCFC-22 (CHClF ₂)		HCFC-142b (C ₂ H ₃ ClF ₂)	
	Prior	Post	Prior	Post	Prior	Post
Greece	0.17±0.03	0.13 (0.09-0.17)	0.2 ±0.08	0.14 (0.06-0.22)	0.02±0.01	0.015 (0.005-0.024)
Turkey	0.05±0.01	0.05 (0.03-0.06)	1.38±1.39	0.85 (0.18-1.52)	0.11±0.08	0.143 (0.049-0.238)
Balkans	0.08±0.07	0.12 (0.04-0.19)	0.45±0.18	0.30 (0.12-0.48)	0.04±0.01	0.042 (0.023-0.061)
Eastern	0.09±0.04	0.09 (0.04-0.15)	1.51±0.62	0.64 (0.12-1.17)	0.12±0.05	0.075 (0.013-0.136)
Middle East	0.1 ±0.1	0.13 (0.00-0.27)	0.78±0.76	1.00 (0.42-1.82)	0.06±0.04	0.059 (0.000-0.128)
Egypt	0.2 ±0.2	0.27 (0.09-0.44)	1.55±1.55	2.08 (1.41-2.79)	0.13±0.09	0.062 (0.000-0.152)
Maghreb	0.21±0.21	0.45 (0.24-0.67)	1.57±1.57	0.56 (0.12-1.00)	0.13±0.09	0.054 (0.003-0.105)
Central (E)	0.92±0.18	0.60 (0.47-0.74)	1.18±0.47	0.36 (0.07-0.65)	0.1 ±0.04	0.052 (0.017-0.088)
Central (W)	0.65±0.13	0.53 (0.42-0.68)	1.87±0.75	0.62 (0.33-0.98)	0.15±0.06	0.128 (0.094-0.167)
Western	1.49±0.3	1.23 (1.11-1.35)	1.67±0.67	0.76 (0.52-1.00)	0.14±0.05	0.187 (0.159-0.215)
Italy	0.92±0.18	0.74 (0.65-0.83)	1.08±0.43	0.70 (0.52-0.88)	0.09±0.04	0.095 (0.071-0.119)
Iberian Pen.	1.01±0.2	0.99 (0.83-1.16)	1.03±0.41	0.39 (0.10-0.68)	0.08±0.03	0.051 (0.015-0.086)
British Isles	0.77±0.15	0.72 (0.65-0.79)	1.24±0.5	0.67 (0.52-0.81)	0.1 ±0.04	0.071 (0.055-0.087)
Domain Total	6.65±1.8	6.04 (4.64-7.50)	15.51±9.38	9.06 (4.49-13.98)	1.25±0.63	1.034 (0.513-1.606)

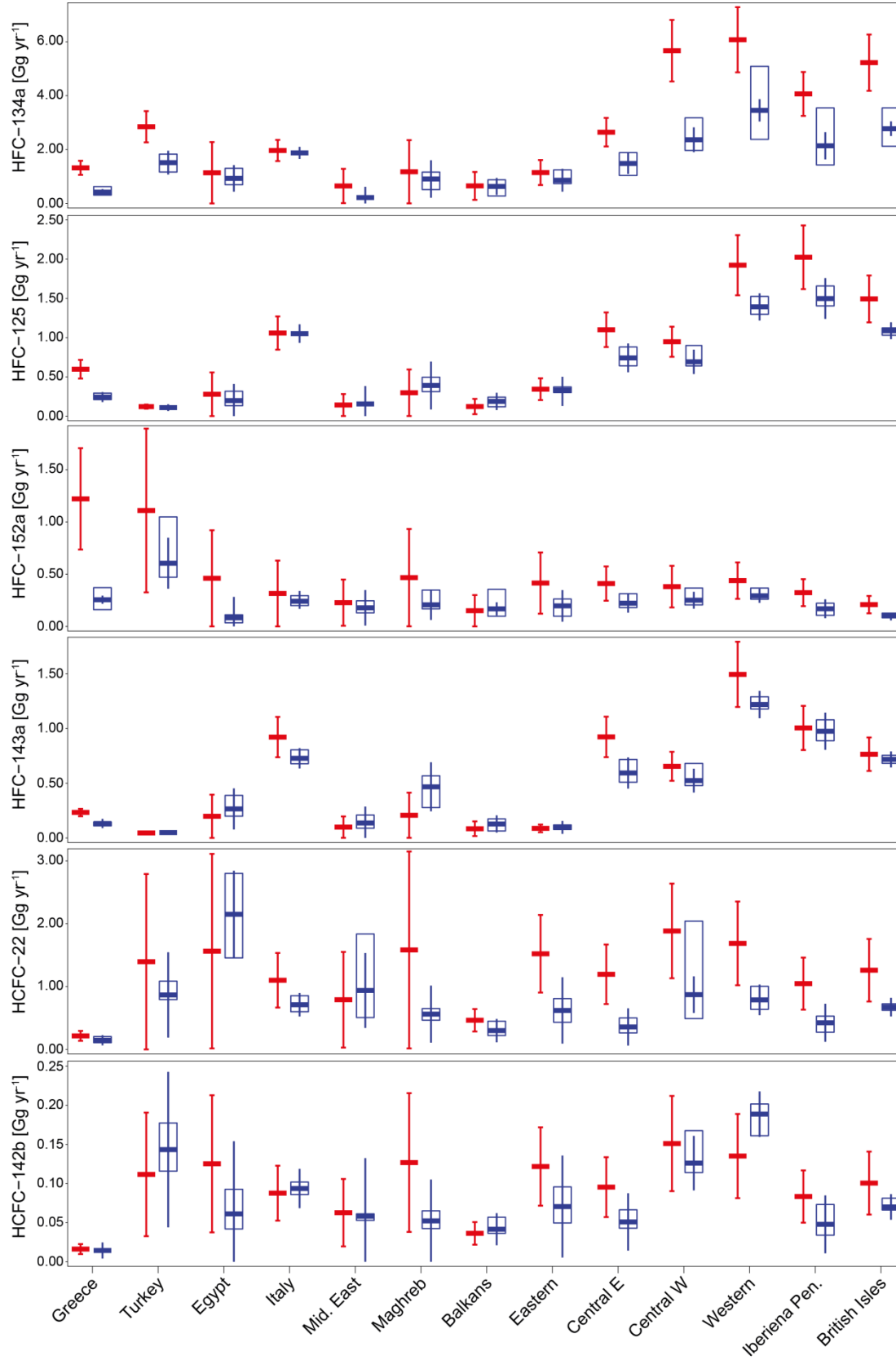


Figure 5.8: Annual emissions for the aggregated regions. A priori emissions are shown in red, with uncertainty giving the 95% confidence range. For the a posteriori estimates boxes show the range of all sensitivity inversions, whereas the thick horizontal line gives the mean of all sensitivity inversions. In addition, the blue error bars give the analytic uncertainty (95% confidence level) averaged over all uncertainty inversions.

These findings of generally smaller than reported HFC-134a emissions in Western and Central Europe resemble the results of other studies performed for earlier years [Lunt, *et al.*, 2015; Brunner, *et al.*, 2016; Say, *et al.*, 2016]. The differences between the country-wide emissions reported to UNFCCC and the range of results found in this study seem to be somewhat more pronounced than in previous studies. This is consistent with Brunner *et al.* [2016], who reported a relatively large range of regional emission estimates depending on the employed inverse modelling system.

HFC-125 domain-total emissions were estimated at 8.1 (6.1-10.3) Gg yr⁻¹ with emissions from the Eastern Mediterranean contributing 15% or 1.2 (0.5 – 2.0) Gg yr⁻¹. Our results for Turkey agree well with those reported to UNFCCC, but are three times smaller than EDGARv42_FT2000. For Greece, our estimate of 0.25 (0.19-0.31) Gg yr⁻¹ falls between the much larger UNFCCC value of 0.60 Gg yr⁻¹ and the smaller EDGARv42_FT2010 estimate of 0.1 Gg yr⁻¹. Emissions from the Eastern region, the Middle East and Egypt remained relatively close to the a priori estimates, whereas for the Balkans we derive a 50% increase compared to the a priori emissions to 0.18 Gg yr⁻¹, which is still considerably smaller than the EDGARv42_FT2010 value of 0.55 Gg yr⁻¹. This stands in contrast to the results of Keller *et al.* [2012] for the Eastern region, showing large discrepancies between “top-down” and “bottom-up” estimates in some of these countries, most likely caused by unrealistically low values reported to UNFCCC. Besides the fact, that the estimates of Keller *et al.* [2012] rely on measurements from Hungary, with a better coverage of North-Eastern Europe than we have from FKL, the discrepancies would be smaller in a retrospective view, because HFC-125 bottom-up emissions of several Eastern European countries were revised upward in the 2016 submissions to the UNFCCC for the year 2009. The largest part of the remaining HFC-125 emissions (71 %) was allocated to Central and Western Europe by the inversion and was about 30 % lower as compared to the a priori estimate with the exception of Italy, where a posteriori values were very close to those reported to UNFCCC. Our results for Western and Central Europe broadly agree with those reported by Brunner *et al.* [2016] and Lunt *et al.* [2015]. However, note that Brunner *et al.* [2016] describes a substantial underreporting of HFC-125 emission from the Iberian Peninsula in 2011, whereas we find an overestimation by ~25% for 2013. This has to do with a retrospective revision of the Spanish UNFCCC reporting, which resulted in a doubling of most HFC emissions reported in 2016. In absolute terms, our estimate of 1.5 (1.2-1.8) Gg yr⁻¹ for the year 2013 agrees well with that given in Brunner *et al.* [2016] for the year 2011 (1.1 – 2.8 Gg yr⁻¹).

HFC-143a is another major HFC, which is commonly used in refrigerant blends for stationary air conditioners. It is sparsely used in Eastern European countries (Balkans, Eastern, Greece and

Turkey), where our “top-down” estimate showed combined annual emissions of 0.39 (0.20-0.57) Gg yr⁻¹, which corresponds to 6.4% (3.3-9.5%) of the domain total of 6.0 (4.6-7.5) Gg yr⁻¹. Emissions higher than the a priori estimates were determined for Maghreb and Egypt with 0.45 (0.24-0.67) Gg yr⁻¹ and 0.27 (0.09-0.44) Gg yr⁻¹, although relatively large uncertainties are connected with these values, since advection from the respective regions was not often observed. 80% of the HFC-143a emissions within our domain have their origin in Central and Western Europe, with the main sources in the Western region and on the Iberian Peninsula. Our estimates agree within 10% with reported UNFCCC values on the domain total basis. For Turkey and the Eastern region, as well as the Iberian Peninsula and the British Isles, reported values agree closely with our estimates (Δ emission estimates < 7%), whereas our estimates of Central E, Central W, Western, Italy and Greece are 18-35% lower than UNFCCC values.

HFC-152a has the smallest 100-year global warming potential of the major HFCs and is primarily used as foam blowing agent and aerosol propellant. Our domain total “top-down” estimate was 2.8 (1.6-4.5) Gg yr⁻¹, which corresponds to only around 6% of estimated global emissions [Simmonds, *et al.*, 2016]. South-eastern Europe’s (Greece, Turkey, Balkans and Eastern) annual emissions were estimated at 1.24 (0.7-2.0) Gg yr⁻¹, corresponding to 44% (26.0-71.2%) of total domain emissions. The largest emissions from any individual region were established for Turkey, 2-3 times higher than our estimates for all other regions within the inversion domain. However, this is still almost a factor of 2 lower than what Turkey reports to the UNFCCC. The UNFCCC inventory of Greece overestimates the posterior emissions inferred in this study by a factor of 5. However, it is known that reporting of this compound is incomplete due to confidentiality considerations, which is why it is likely that the inventories for HFC-152a are incomplete and incorrect. Furthermore, for the UNFCCC, emissions of HFC-152a are reported in the country where the consumer product is manufactured. For example, if a foam is blown in country X and sold to country Y, emissions would mainly occur during usage in country Y but are reported under country X. From a global perspective this makes sense but is not compatible with real emissions in the respective countries. Emissions from Non-Annex I countries belonging to the Middle East and Northern Africa (Maghreb, Egypt) are small (0.42 (0.03-0.93) Gg yr⁻¹). Our “top-down” estimates for Central and Western Europe make up for the remaining 1.17 (0.84-1.52) Gg yr⁻¹ of the annual HFC-152a emissions. For all Central and Western European countries, reporting values to UNFCCC, we find a general tendency, that “top-down” emissions are lower than UNFCCC values, with largest discrepancies for the Iberian Peninsula and Central E. For the British Isles, our results are a factor of 2 smaller than the findings of Lunt *et al.* [2015] for the years 2010-2012. In contrast, our estimates for the British Isles agreed

within their uncertainties with those reported in Simmonds et al. [2016], which is also true for our estimates for the Central W region and the Iberian Peninsula. In contrast, our “top-down” estimates for Italy are a factor 2 smaller than reported by the latter authors.

5.3.5 Summary of Halocarbon Emissions

Our best estimate of domain total halocarbon emissions for 2013 was 85.1 (63.0-109.2) Tg CO₂eq yr⁻¹ for the four analysed HFCs and 18.3 (9.0-28.2) Tg CO₂eq for the two HCFCs. This corresponds to 12.5% (8.9-16.7%) and 2.6% (1.3-3.9%) of global halocarbon emissions [Carpenter and Reimann, 2014]. The HFC emissions from the Eastern Mediterranean (Greece, Turkey, Middle East, Egypt, Eastern, and the Balkans) accounted for 14.7 (6.7-23.3) Tg CO₂eq yr⁻¹ and the HCFC emissions from the same region for 9.7 (4.3-15.7) Tg CO₂eq yr⁻¹.

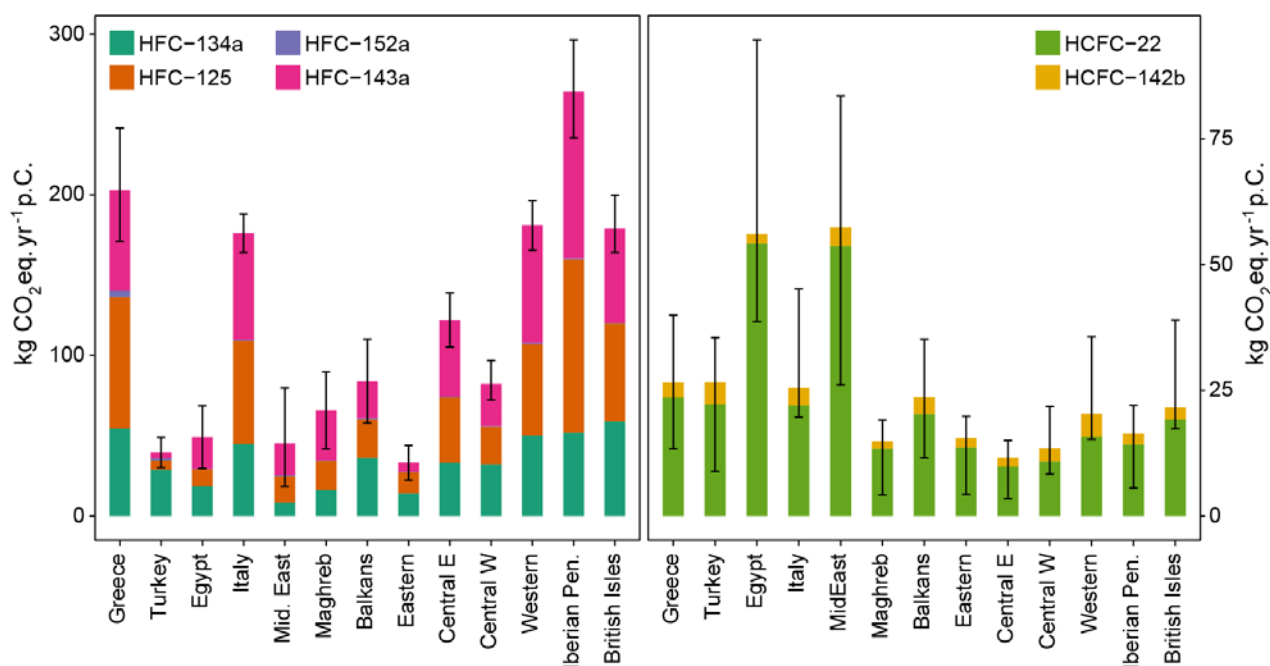


Figure 5.9: Annual per capita (p.C.) emissions in CO₂ equivalents, derived from the base inversion and all sensitivity inversions. The results have been computed using the 100-yr GWP (GWP100) values of [Carpenter and Reimann, 2014]. The bars show the average mean of all inversions, whereas the error bars show our uncertainty estimate including analytical and structural uncertainty (see Section 5.3.4 for details).

As expected, per-capita CO₂ equivalent emissions of HFCs vary strongly in the Eastern Mediterranean (Figure 5.9). For Greece, per capita emissions were similar to other Western European countries, whereas for the developing countries (Article 5 countries) in the Eastern Mediterranean (Turkey, Middle East), with the exception of Egypt, per-capita HFC emissions were much smaller. On the other hand, per capita CO₂ equivalents of HCFC emissions were largest in Article 5 countries in the Middle East and Maghreb region, where the phase-out of these compounds is delayed as compared to the Non-Article 5 countries in Western Europe. In this context, it is also interesting to

note that the HCFC per-capita emissions from Greece (Non-Article 5) are similarly large as those from its neighbour Turkey (Article-5).

5.3.6 Temporal Variability of HFC-152a Emissions

Some of the larger HFC-152a pollution peaks observed at FKL (see Figure 5.3) are not well reproduced by the transport model. The atmospheric inversion only slightly improved the comparison, indicating the inability to unambiguously assign an emission region or a constant emission process to these peaks. In the following, the transport situations experienced during the observed HFC-152a peaks are analysed in more detail.

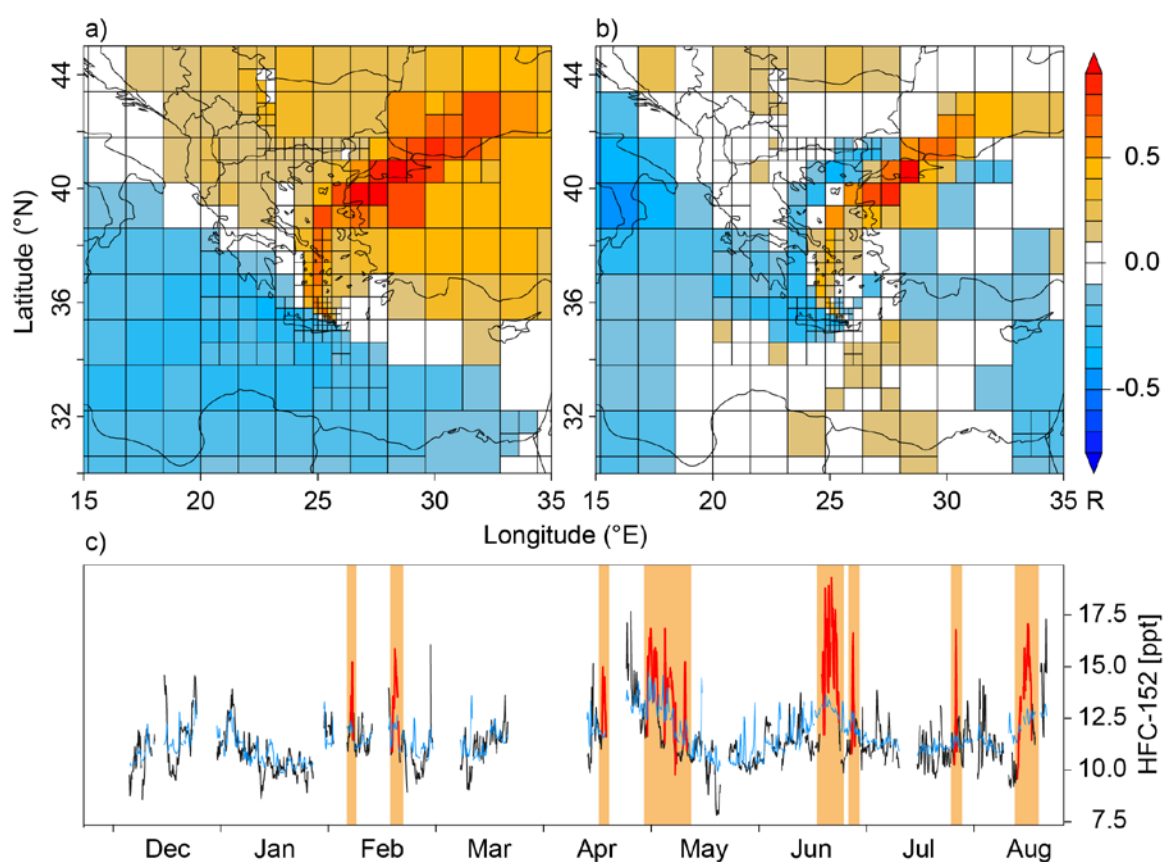


Figure 5.10: Spatial distribution of the Pearson Correlation Coefficient (R) for (a) the entire time series of HFC-152a observations at Finokalia and the per-cell source sensitivity and for (b) the period of the pollution peaks, which are highlighted in red in (c) the observed (black) and simulated a posteriori (BASE inversion) (blue) mole fractions of HFC-152a.

The time series of HFC-152a in FKL (Figure 5.10c) shows intermittently appearing pollution peaks, most pronounced in June and August, which are badly reflected by the simulations, even when a posteriori emissions are used. Especially two observed broader peaks in June and August are not visible in the simulations. This could be due to inaccuracies in the transport model and weaknesses of the inversion, or because of large, localized, and temporally varying emissions sources, such as HFC-152a production facilities [Keller, *et al.*, 2011]. However, our inversion approach assumes

temporally constant emissions and is not able to unambiguously assign a specific source location or area to individually observed pollution peaks that are caused by temporary emissions. For the localization of such emission sources, we used a simple, qualitative approach, by calculating the correlation between the observed HFC-152a time series and FLEXPART simulated source sensitivities in the individual grid cells. First, the correlation for the complete time series was calculated, thereby ignoring the proposed intermittent character of the source. Using this method, generally positive Pearson correlation coefficients were established for all land areas with maximal correlation coefficients located in grid cells in Northwestern Turkey (Figure 5.10a). To further isolate the potential source areas, correlations were calculated using only peak periods in the observations at FKL, including the times of increasing and decreasing mixing ratios at the flanks of each peak. These results showed a further restriction of significant positive correlation coefficients to Northwestern Turkey, bordering the Marmara Sea and the Bosphorus area (Figure 5.10b), which are both important industrial regions. This result could point to large contributions from the metropolitan area of Istanbul, where HFC-152a could be emitted from installed consumer products. However, due to the strong temporal variability in emissions, which seems to be inherent to the observed peaks, the results are more likely to be explained with large emissions from an industrial facility in the localized regions.

5.3.7 The Impact of Halocarbon Observations at Finokalia

Our campaign in Finokalia added halocarbon observations in an area of Europe from which emissions are only sporadically detected by the existing AGAGE network. We assessed the added value of a station in FKL, by excluding it from the inversion and estimating Eastern Mediterranean emission only from the existing AGAGE network (S-NFKL). Furthermore, we excluded all stations but FKL from the inversion to test if the existing AGAGE sites add value to our estimate of emissions in the Eastern Mediterranean (S-OFKL). The regional emission estimates using the different station setups are shown in Figure 5.11. For Greece and Turkey, which were best covered by our observations in FKL, a clear influence of the measurements at FKL on the “top-down” emission estimates can be seen. For HFC-125 and HFC-134a, used as exemplary compounds for this analysis, the inversion excluding FKL was mainly driven by the a priori values, whereas including FKL strongly reduced the emissions and the analytic uncertainty (Figure 5.12). A similar effect is seen for the Middle East and Egypt, although the number of times during which our site was sensitive to these areas was limited. These results clearly show that regional emission estimates using only AGAGE stations for areas as far as the Eastern Mediterranean are unreliable and an extension of the current network is critical for emission control in this economically very dynamic area.

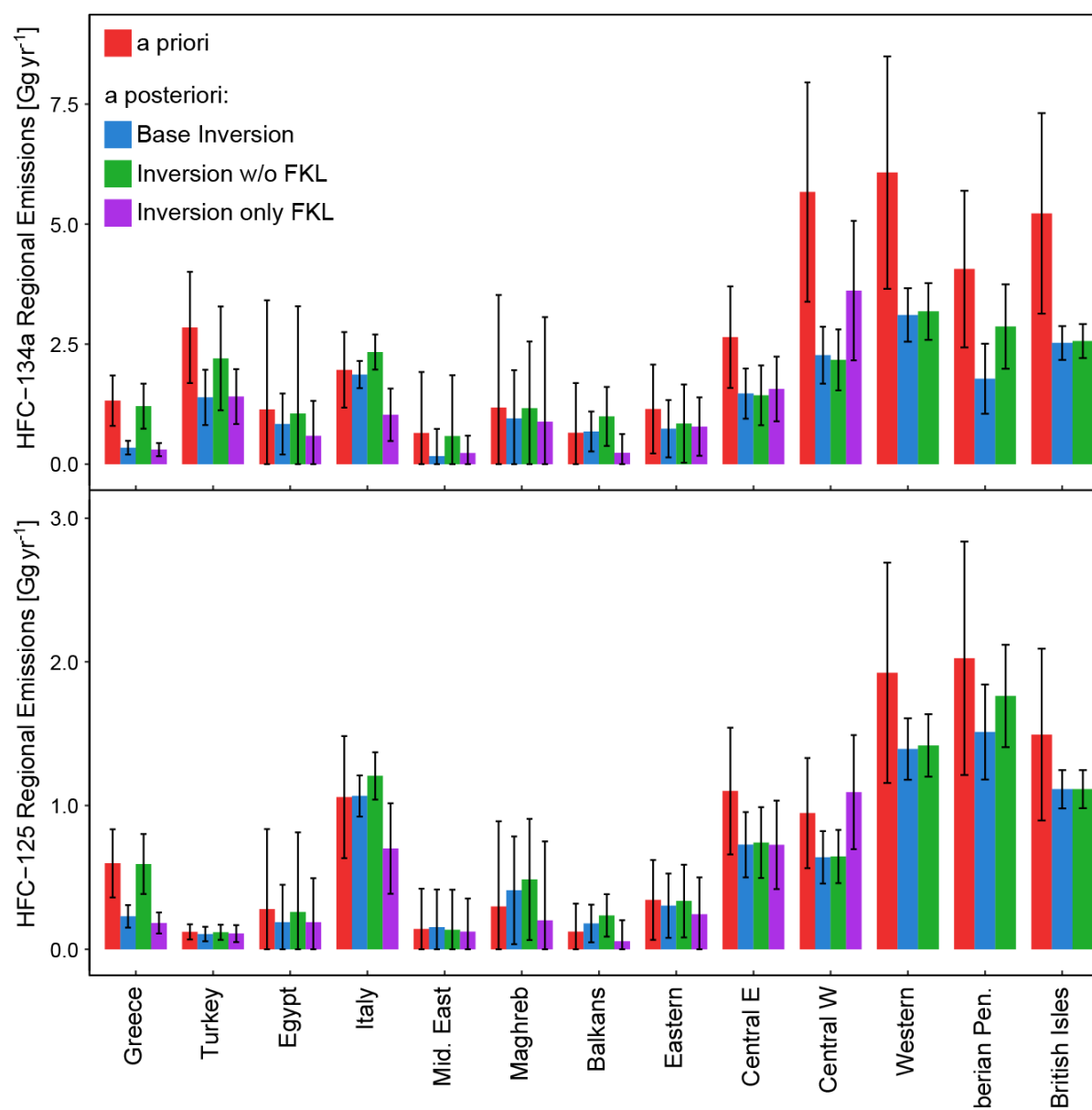


Figure 5.11: Regional annual emission estimates of 2013. The a priori of our base inversion is shown in red. A posteriori results are shown for the BASE inversion (blue), the inversion excluding Finokalia (S-NFKL, green) and the inversion only using observations from Finokalia (S-OFKL, purple). Error bars represent the 95% confidence levels. Note that for the inversion based on Finokalia observations alone (S-OFKL) the inversion domain was cropped in the West and no a posteriori emission for the western part of the domain were estimated.

For Eastern European countries and the Balkan regions, the influence of measurements at FKL reduced HFC-134a and HFC-125 emissions and emission uncertainties slightly. However, Central European measurements have a similar influence on these results. An interesting impact over larger distances can be observed for Italy and the Iberian Peninsula, where the additional measurements from FKL have more of a reducing effect on the absolute emissions than on the uncertainties, whereas emissions in Central and Western Europe including the British Isles are largely unaffected by our measurements at FKL. The effect of measurements at FKL on modelled emissions from Italy and the Iberian Peninsula can be explained by the additional constraints provided by FKL for Italy. These decreased Italian emissions and at the same time slightly increased baseline mixing ratios for

JFJ and CMN for periods with influence from the Western Mediterranean. Since simulated source sensitivities are often simultaneously elevated for Italian and Iberian source areas, the increased baseline will translate also to smaller emissions on the Iberian Peninsula even though the observations at FKL were virtually not sensitive to emissions from this region.

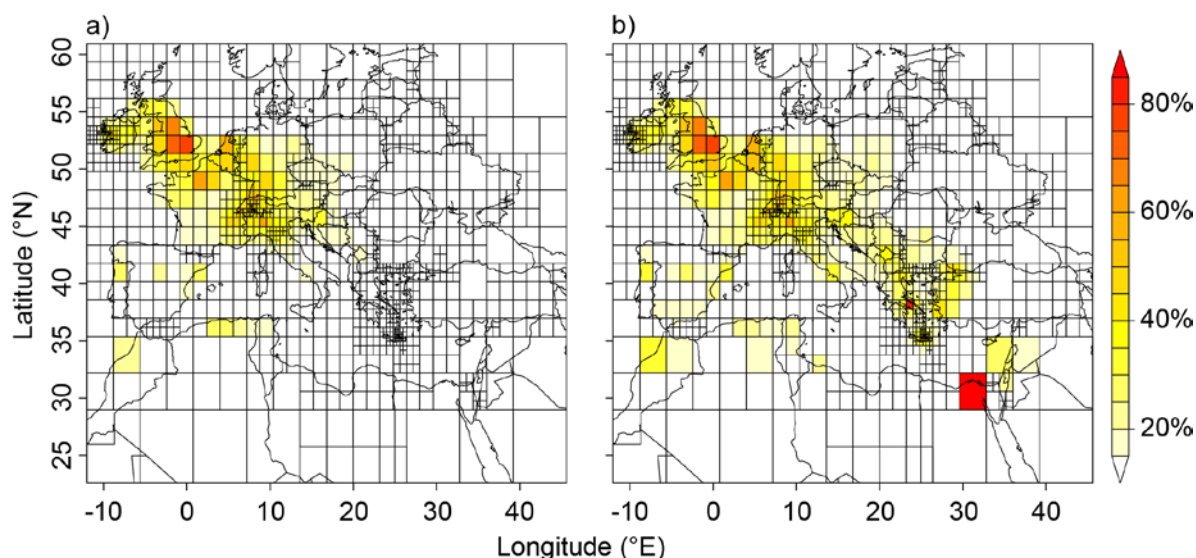


Figure 5.12: HFC-134a uncertainty reduction (%) achieved by (a) the inversion excluding observations from Finokalia (S-NFKL) and (b) the BASE inversion using observations from all four sites including Finokalia.

The inversion using only observations from FKL (S-NFKL) had virtually no effect on the a posteriori emissions and their uncertainty for Greece, Turkey, the Eastern region and the Middle East as compared with the BASE inversion. For Egypt, the Maghreb countries and the Balkans slightly reduced a posteriori estimates were observed, whereas for Italy, Central and Western Europe the a posteriori estimates differed strongly from the BASE inversion and showed little uncertainty reduction. These results indicate the importance to include all available halocarbon observations in regional estimates even if these are as distant as Monte Cimone is to Finokalia (~1600 km).

5.4 Conclusion

During a period of six months, from December 2012 to August 2013, we performed continuous halocarbon observations at the atmospheric observation site of Finokalia (Crete, GR), the first observations of this kind in the Eastern Mediterranean. The combination of these and other Western European halocarbon measurements with an atmospheric transport model, and Bayesian inversion techniques, allowed us to estimate regional-scale halocarbon emissions and for the first time pro-

vide reliable “top-town” emission estimates for the Eastern Mediterranean, a region of very diverse economic development and home to approximately 250 million people.

Due to the maritime and remote location of Finokalia, pollution from major metropolitan areas (the closest at a distance of 350-700km) tend to be better mixed into the background atmosphere at their arrival than at other continuous observation sites such as Monte Cimone (Italy) or Jungfraujoch (Switzerland). As expected this lead to generally smaller peak amplitudes for HFC-134a, HFC-125 and HFC-143a in Finokalia, compared to these sites. However periodic peaks of HFC-152a were unexpectedly high, indicating one or several strong HFC-152a emission sources within the region directly influencing Finokalia. Higher peak mole fractions than at the Western European observation sites were observed for HCFC-22 and HCFC-142b, because of continued emissions from Article 5 regions such as Turkey, Egypt and the Middle East.

A range of sensitivity inversions showed that our regional-scale results are largely independent of the uncertainty assigned to the a priori emissions and the design of the data-model-mismatch covariance matrix. In general, including off-diagonal elements in the uncertainty covariance matrices and, therefore, considering auto-correlation in the data-mismatch and a-priori uncertainty, led to lower a posteriori emission estimates (BASE and S-ML). Larger discrepancies between these sensitivity inversions were only seen for Central and Western Europe and HFC-134a emissions.

Our best estimate of a posteriori (“top-down”) emissions and their uncertainties was derived as an average over the five sensitivity inversions and considering their spread and individual analytical uncertainty. For Article 5 countries in the Eastern Mediterranean (Turkey, Middle East, Egypt) a posteriori HCFC emissions were in the range assumed in our a priori, whereas they were smaller for the Non-Article 5 country Greece. In terms of HFC emissions in the Eastern Mediterranean, we estimated much smaller emissions than reported to the UNFCCC for all analysed compounds in Greece, whereas for Turkey our “top-down” estimates were similar to UNFCCC-reported values for HFC-125 and HFC-143a, but were much and slightly smaller for HFC-134a and HFC-152a, respectively. For the remaining regions in the Eastern Mediterranean no clear trend between “top-down” and our a priori estimates could be established, partly owing to the very insecure a priori estimates. For the Western and Central European areas of our inversion domain, our “top-down” estimates largely agree with other inverse modelling studies, although our results are within the lower range of previously reported emissions. Especially for HFC-134a and HFC-125 we obtained “top-down” estimates up to a factor of two smaller than reported UNFCCC values for the British Isles, France, Benelux and Germany.

In the context of lower-than-reported HFC-152a emissions from Turkey, the inversion algorithm was not able to perfectly simulate periodically measured, large HFC-152a pollution events at Finokalia. This could either be due to temporally varying emission sources, shortcomings in the atmospheric transport model or an unsuitable inversion setup. The latter two options can be ruled out since the transport simulation and inversion worked sufficiently well for other compounds. The first possibility was further analysed by using the temporal correlation between our observations and the simulated source sensitivity within individual grid cells during and around times when pollution events were observed. This allowed for the localisation of a possible emission region, located in the northwestern part of Turkey between the Aegean coast and the city of Istanbul. The suspected temporal variability in the HFC-152a emissions rather points towards emissions from a HFC production plant than from product application and consumption.

Our measurements in Finokalia and the inversely estimated emissions show, that an additional observation site strongly increases the geographic extent and the quality of the inversion results, by reducing the a posteriori emission uncertainties in the Eastern Mediterranean in the range of 40-80% as compared to an inversion only using the Central European AGAGE observations. Including observations from Finokalia reduced estimated Greek HFC-134a emissions by a factor of four, while decreasing the uncertainty by the same factor. Additionally, the location of Finokalia allows the detection of Middle Eastern and North African emissions during specific flow conditions, which is especially interesting due to the restrictions on the use of HCFCs for developing countries by the Montreal Protocol, which recently became effective. However, measurements during several years or a fixed monitoring station would be required to investigate trends in halocarbon emissions, for a continued “top-down” validation of south-eastern European UNFCCC inventories or for the monitoring of the HCFC phase out in Eastern Mediterranean Article 5 countries.

Acknowledgements

This research was funded by the Swiss National Science Foundation (project 200021-137638), the Swiss Federal Office for the Environment (FOEN), and the Swiss State Secretariat for Education and Research and Innovation (SERI). Additional funding was obtained from the EC FP7 project InGOS (Integrated Non-CO₂ Greenhouse Gas Observing System; grant agreement number 284274) and trans-national access (TNA) from the EC FP7 ACTRIS Research Infrastructure (grant agreement number 262254). We thank the Finokalia station staff for granting access to the site and supporting the set-up and operation of our measurements. The International Foundation High Altitude

Research Stations Jungfraujoch and Gornergrat (HFSJG) is acknowledged for the opportunity to perform observations on the Jungfraujoch.

Chapter 6 Halocarbon emissions on the Iberian Peninsula, inferred from atmospheric measurements in the French Pyrenees.

To assess European halocarbon emissions, the AGAGE network is operating observation sites at 3 locations: Mace Head (Ireland), Zeppelin mountain (Spitsbergen, Norway), Jungfraujoch (Switzerland) and the affiliated station at Mt. Cimone (Italy). Although the Iberian Peninsula can be detected from these stations, it is in the periphery of their sensitive region and it is suspected, that emissions from countries closer to the observation sites may be erroneously allocated to Spain and Portugal. Therefore, a 1.5 year measurement campaign (October 2013 to June 2015) was performed at the high-alpine research facility of Pic du Midi to extend the AGAGE network's sensitivity towards the undersampled Iberian Peninsula. In this chapter the results of this campaign are presented and an atmospheric transport model, together with a Bayesian framework, similar to Chapter 5, are used to quantitatively assess emission sources of HFC-134a and HFC-125. Additionally the influence of the complementing measurements at Pic du Midi on the emission estimates are analysed by comparing an inversion with the existing AGAGE sites and the extended network, respectively, for the time period of the year 2014.

6.1 Site Description

Observations of halocarbons took place on Pic du Midi (0.14°E, 42.94°N) from October 2013 until June 2015. The Pic du Midi (PDM) high-altitude observatory is located on top of an isolated peak (2877 m a.s.l.) on the northern edge of the central Pyrenees and is frequently used for the study of ozone and atmospheric pollutants [Gheusi, *et al.*, 2011; Fu, *et al.*, 2016]. Forming a natural barrier between Spain and France, this mountain range extends over 400 km from the Mediterranean Sea to the Atlantic. The air inlet was installed on the rooftop of the laboratory building at the eastern side of the observatory complex, allowing air to be advected unobstructed towards the inlet in a sector of 270° from NW to SW, whereas westerly flows cross the complex before being detected by our instrument. Except possible small emissions of halocarbons accompanied with the air conditioning

infrastructure of the PDM observatory itself, affecting westerly winds, no significant point sources are located in the near vicinity. The two closest cities ($< 70'000$ inhabitants) are Pau and Tarbes, located 60 and 30 km to the northwest, on a plain about 1300 m below Pic du Midi. Assuming that the halocarbon emission distribution follows that of population, some possible source regions are within the sensitive area of Pic du Midi. During frequently occurring advection events with a southerly component, ahead of troughs or cyclones over the Atlantic, Pic du Midi is influenced by emissions from Zaragoza and Barcelona, at a distance of 170 km and 240 km, respectively, as well as more distant cities in Central Spain and on the Northwestern Spanish coast (Figure 6.1). To the north there are two urban areas, Bordeaux (220 km) and Toulouse (130 km), with a population of around 1 million people, whereas in the border region of northern Spain and southwestern France on the Atlantic coast, the Basque country is another often detected source region during our campaign. Standard meteorological data, as well as O_3 , NO_x and CO observations, are provided by the “Laboratoire d’Aérologie” (University of Toulouse) on a continuous basis.

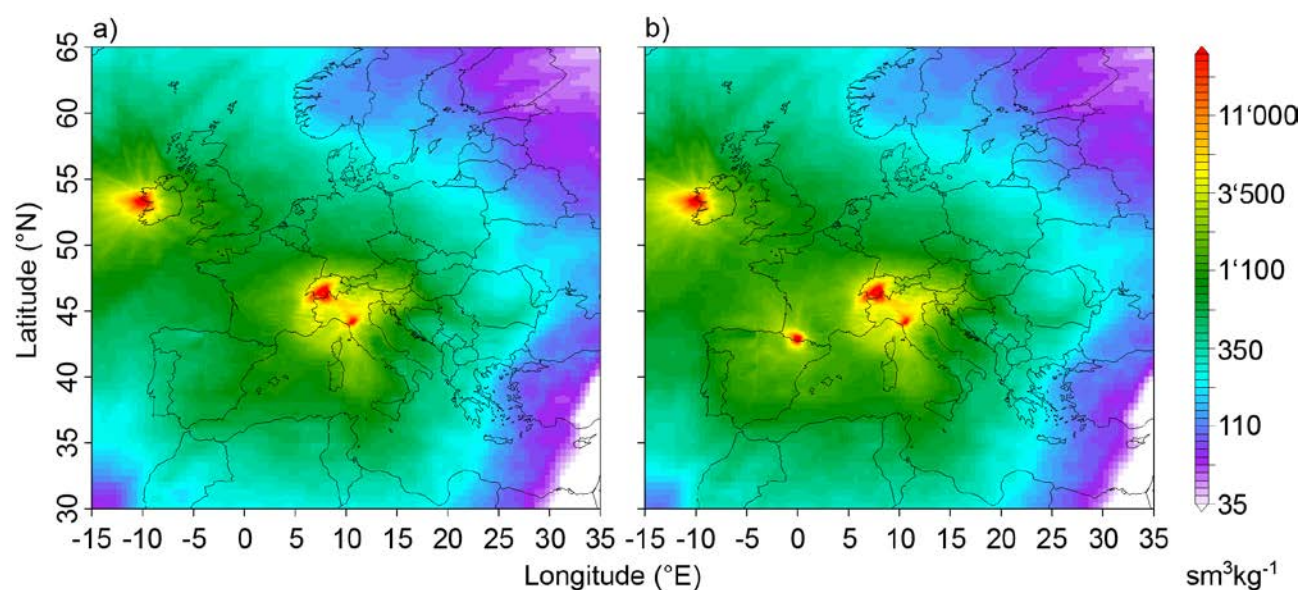


Figure 6.1: FLEXPART footprints during the Pic du Midi campaign period for the existing AGAGE network (a) and the AGAGE network including Pic du Midi.

6.2 Observations

In this section, measurements of HFC-134a, HFC-125 and HFC-152a, collected during our measurement campaign from October 2013 to June 2015 at Pic du Midi are described. Additionally locally collected flask samples, used to evaluate possible local halocarbon contamination sources at the Pic du Midi observatory are discussed. Baselines of continuous observations were derived using the “robust extraction of baseline signal” (REBS) approach by *Ruckstuhl et al.* [2012]. The integrity

of individual measurements was ensured manually by removing individual observations or observation periods showing poor chromatographic quality.

6.2.1 Flask Samples and Local Pollution Sources

Pic du Midi has been known for its astronomic observatory since the early 1900, the consequence being that the complex hosts a variety of telescopes, including the large “Bernard Lyot Telescope” (BLT), as well as installations for atmospheric science and touristic infrastructure (e.g. kitchen, hotel-rooms). In order to adapt the sensitive telescope mirrors to ambient temperatures, air condition systems are used to cool down the inside of the telescope copula in advance of the opening, which could be a potential emission source for halocarbons, used as refrigerants. In order to evaluate these possible sources of contamination, 10 flask samples were taken, using evacuated, electropolished sample flasks (2.5 L), which were filled passively at distributed sample sites throughout the observatory complex. However, due to the passive filling technique, flask pressures were equivalent to ambient pressure levels at ~2800 m a.s.l., challenging the preconcentration process during the analysis, which limits the number of runs performed on the Empa Medusa. Thus, combined with the temporally and spatially sparse sampling, these values should only be used as an indicator for possible contamination sources (Table 6.1).

Table 6.1: Mole fraction measured in flask samples, taken throughout the observatory on Pic du Midi. Every flask was measured twice and the mean of both measurements is given. Location denotes the place where the flask sample was collected as well as the direction of the sample site as seen from the ADS air inlet on the roof of the Laboratory building. X is referring to a location in the same building on different levels of the laboratory building.

Location	HFC-134a [ppt]	HFC-125 [ppt]	HFC-152a [ppt]	CFC-114 [ppt]
Background Mole Fraction ¹	85.7	18.0	11.2	16.3
BLT (outside copola) - WNW	129.1	19.6	18.8	15.5
BLT (inside copola) - WNW	3'584.4	292.0	682.8	15.7
BLT (lowest level, beside AC) - WNW	11'483.1	311.5	2'031.6	15.9
BLT (lowest level, workshop) - WNW	11'791.1	267.2	2'088.1	16.3
Coronagraph (outside copola) - S	139.3	15.5	9.1	15.5
Coronagraph (inside copola) - S	195.3	15.9	12.0	16.1
Kitchen (cold storage) - WNW	961.3	23.7	193.7	15.7
Tourist Complex (exhaust air) - WNW	420.3	16.4	40.1	15.8
Tourist Complex (gondola station) - W	83.3	16.5	9.6	16.3
Lab-Building (highest level) - X	205.7	16.5	437.6	16.4
Lab Building (ADS Room) - X	487.3	15.8	1'379.5	15.8

¹ Mean background mole fractions as estimated with REBS for HFC-134a, HFC-125 and HFC-152a. Background mole fractions for CFC-114 are based on global estimates for 2012 from *Carpenter and Reimann* [2014]

Observed HFC-134a mole fractions reached substantially high values inside the BLT at various levels, up to a factor of ~ 140 higher than the estimated mean background level at PDM during the campaign. Although simultaneous samples outside the copula were only increased by a factor of ~ 1.5 , substantial local releases of HFC-134a may have occurred every time the copula was opened. Elevated HFC-134a mole fractions, increased by a factor of ~ 5 compared to background mole fractions, were also found in samples from the tourist complex and within the room where our instrument was installed. The latter shouldn't influence the measurements, as the system is expected to be airtight. However, largest in situ mole fractions at PDM were observed during southwesterly flow, which is not in line with the direction of the BLT (see Figure 6.2).

A similar pattern was found for HFC-125 samples, with the BLT being the only sampling site showing substantially elevated HFC-125 mole fractions. Once again, an increased density of observed higher mole fractions did not correspond to favourable flow conditions for transport from the BLT to the air inlet.

Abundances of HFC-152a were also increased inside the BLT, but likewise in the Laboratory building, wherein our instrument was set up and on top of which our air inlet was installed. With mole fractions ~ 120 - 190 times higher than mean baseline values at Pic du Midi, exhaust air from these buildings may have highly affected our measurements. Combined analysis of local wind direction and HFC-152a observations during the campaign didn't show any relationship that could have been attributed to the BLT (Figure 6.2). However air escaping the building through open doors or windows could be turbulently transported to our air inlet. This should have been relatively seldom, as the rooftop platform was seldom visited and the laboratory building was normally accessed from the tourist complex.

Being aware of the fact that small scale dynamics around Pic du Midi are beyond what we can resolve using local wind measurements and to avoid the removal of observations from the south which could be attributed to emission sources in the Pyrenees or Northern Spain, we assume that only the highest mole fractions ($p > 0.99$) were caused by local emissions, during relatively calm (wind speed < 5 m/s) conditions. As a comparison to the measurements including all the data in Figure 6.3, adjusted observations are shown in Figure 6.5 and will be used for further analysis.

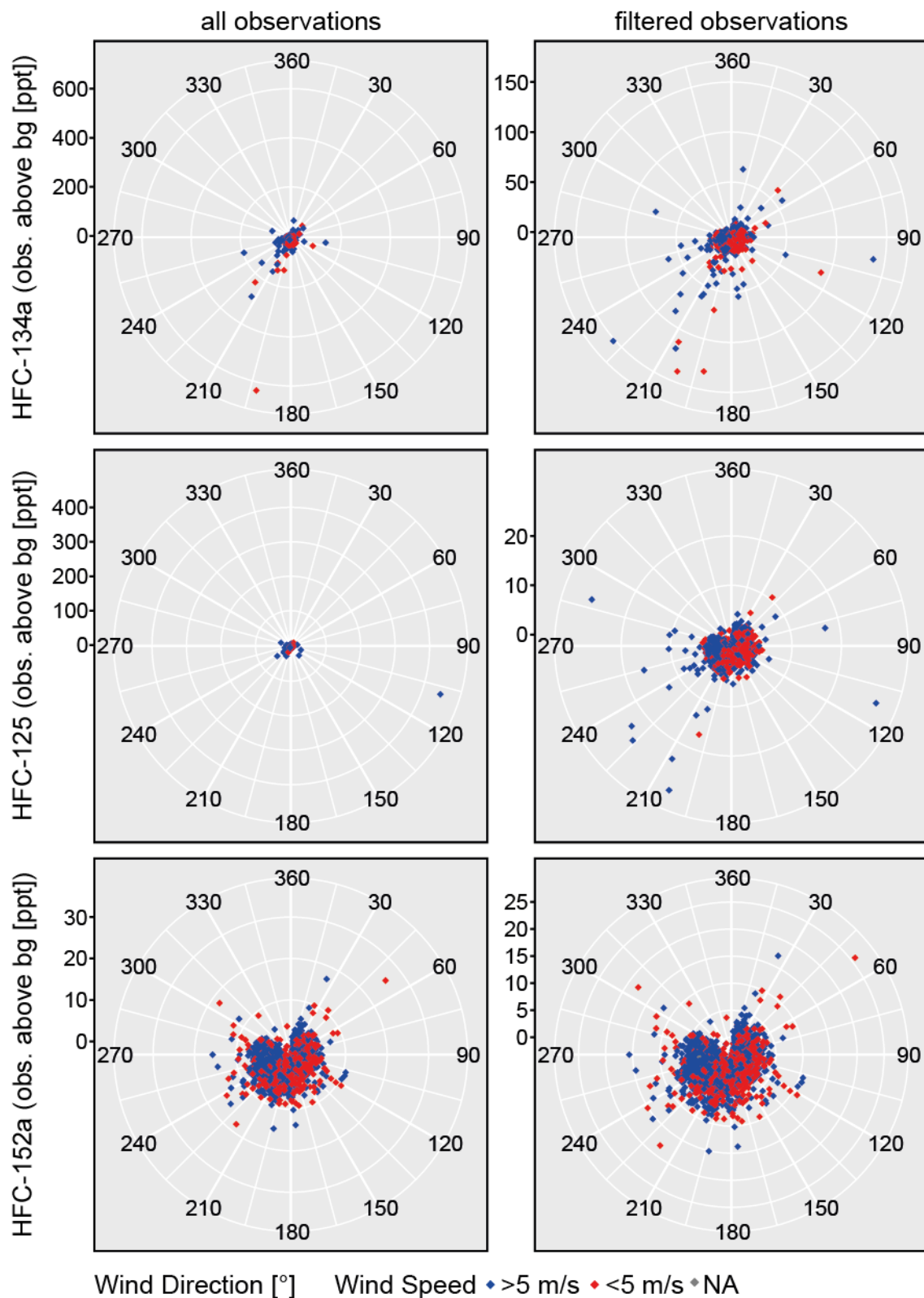


Figure 6.2: Pic du Midi observations (unfiltered and filtered for assumed local pollution) for each compound. Mean wind direction during the sampling period of each individual observation is shown, as well as wind speed (calm conditions with wind speed < 5 m/s (red), normal to windy conditions with wind speed > 5 m/s (blue)).

6.2.2 In situ Observations

HFC-134a is used in domestic refrigeration and is currently the most common cooling agent used in automobile air conditioners. At $88.7 (\pm 1.7)$ ppt (parts-per-trillion, 10^{-12}), the estimated mean background mole fraction agrees well with the similarly estimated mean background values at the 3 AGAGE sites Jungfraujoch (JFJ), Mace Head (MHD) and Monte Cimone (CMN). Over the course of the campaign, PDM sees rather frequent HFC-134a pollution events, with a maximum of 242.8 ppt (721.9 ppt if the filtering for local pollution, as explained above, is not applied), which surpasses maxima from similar mountainous observations sites such as CMN (151.1 ppt) or JFJ (120.7 ppt) by almost a factor of ~ 2 (~ 5). As a consequence the standard deviation derived for PDM observations is around twice as high as for the other sites as shown in Table 6.2.

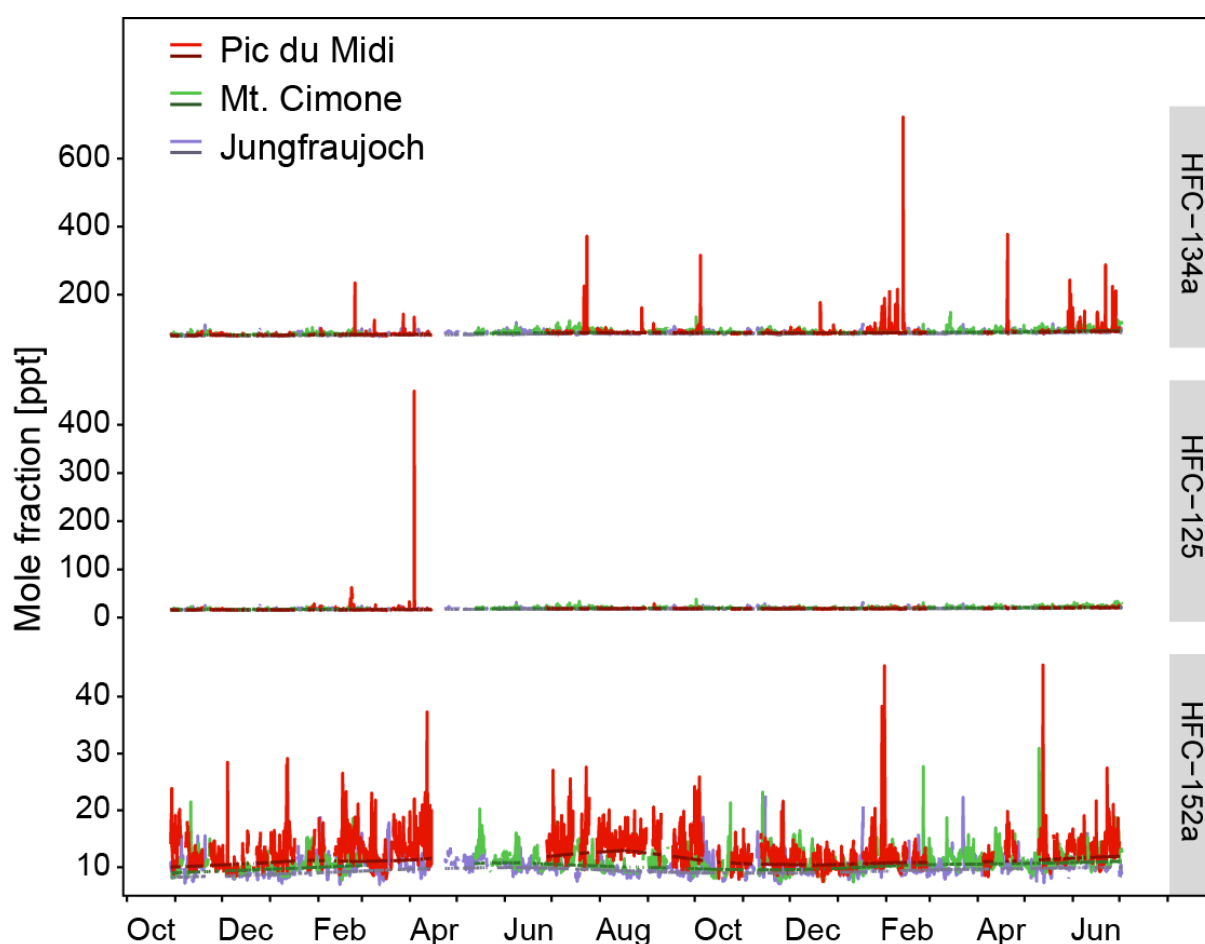


Figure 6.3: Unfiltered observations from Pic du Midi (red), Mt. Cimone (green) and Jungfraujoch (purple) during the campaign period from Oct. 2013 – Jun. 2015.

A main application of HFC-125 is in refrigerant mixtures, such as R-410a (50% HFC-32, 50% HFC-125), which are becoming more widely used, as HCFC containing refrigerants are being phased out. It is also used as a gaseous fire suppression agent. During a phase in early 2014 (January - March), the observations at PDM show frequent pollution peaks, with 3 events being markedly

different from the others, with maximum mole fractions at 46.0 ppt (470.1 ppt for unfiltered data), which is in the mean about 30% (1200%) higher than maximum mole fractions observed at JFJ and CMN. After this period, the detection of pollution events at PDM becomes scarce and the measurements between July 2014 and July 2015 are comparable to the observations at JFJ and CMN. Over the whole period, the standard deviation is 2.2 ppt, which is in the same range as observed at JFJ and CMN. Excluding the first period with distinct pollution events, the standard deviation is 1.4 ppt, which is closer to what we observe at the coastal location of MHD. The mean baseline value at PDM (18.0 ± 0.6 ppt) is in the range of the AGAGE sites (JFJ: 17.8 ± 0.3 ppt, MHD: 17.2 ± 0.2 ppt, CMN: 19.1 ± 0.6 ppt).

Table 6.2: Basic statistics for the observations taken during the Pic du Midi campaign. Observation sites are: Pic du Midi (PDM), Jungfraujoch (JFJ), Mace Head (MHD), Mt. Cimone (CMN). Shown are the number of observations (n.obs), the mean, minimum (min), maximum (max) and standard deviation (sd) of the observations and the background, which was estimated with REBS. The mean measurement uncertainty (mean unc) is the moving window uncertainty of the observations and the constant uncertainty (const unc) derived by REBS for the background.

	site	n.obs	Observations					Background (REBS)			
			mean	min	max	sd	mean unc	mean	min	max	const unc
			[ppt]	[ppt]	[ppt]	[ppt]	[ppt]	[ppt]	[ppt]	[ppt]	[ppt]
HFC-134a	PDM	2702	88.7	76.9	242.8 (721.9) ¹	11.6	0.91	85.7	79.9	92.8	1.7
	JFJ	3270	87.5	76.1	120.7	5.5	0.29	84.1	78.4	89.4	1.3
	MHD	3392	86.7	77.8	142.9	4.8	0.16	85.1	81.0	88.5	0.7
	CMN	3054	90.6	78.3	151.1	7.0	0.31	87.3	80.8	94.7	1.9
HFC-125	PDM	2749	18.7	14.3	46.0 (470.1) ¹	2.2	0.49	18.0	16.1	21.0	0.6
	JFJ	3145	18.9	15.4	32.7	1.8	0.07	17.8	16.0	19.9	0.3
	MHD	988	17.4	15.8	22.2	1.1	0.04	17.2	16.4	19.9	0.2
	CMN	3059	20.2	15.8	38.4	2.5	0.09	19.1	16.4	21.8	0.6
HFC-152a	PDM	2755	12.8	7.4	38.3 (45.6) ¹	2.9	0.23	11.2	10.0	12.9	1.2
	JFJ	3302	10.1	6.9	22.6	1.5	0.08	9.3	8.2	10.0	0.8
	MHD	3416	10.4	7.6	20.2	1.0	0.06	10.0	9.4	10.3	0.5
	CMN	3077	10.9	7.3	30.9	1.7	0.10	10.1	9.0	11.0	0.8

¹Maximum including assumed strongly locally influenced observations

HFC-152a is primarily used as foam blowing agent for the manufacturing of styrofoam insulation boards and as propellant. Unlike HFC-125 and HFC-134a observations, HFC-152a measurements at PDM show frequent pollution events in the range of peak mole fractions observed at CMN (~25-30 ppt). As an exception 6 events have been detected with mole fractions exceeding measurements at CMN, which is the AGAGE station influenced mostly by anthropogenic emissions in the Po-Valley. During these events, observations at PDM reach mole fractions of up to 38.3 ppt (45.6 ppt

for unfiltered data), 24% (48%) higher than HFC-152a maxima detected at CMN. Due to the frequent occurrence of air masses enriched with HFC-152a, the standard deviation at PDM is 2-3 times higher than at the 3 Central European AGAGE sites. Although mean background mole fractions at PDM agree with the comparison sites within uncertainties (PDM: 11.2 ± 1.2 ppt, JFJ: 9.3 ± 0.8 ppt, MHD: 10.0 ± 0.5 ppt, CMN: 10.1 ± 0.8 ppt), they are increased between July and October 2014 compared to the other sites, before reaching normal levels again for the rest of the campaign. As described before, local air samples from the laboratory building below the air inlet showed increased concentrations of HFC-152a (Table 6.1). Although we can't observe a direct relationship between local wind speeds or flow direction with the estimated background values, it is arguable if special circumstances concerning the building structure, we are not aware of, have led to a mixing of ambient air transported to the air inlet with HFC-152a enriched air from inside the building.

6.3 Atmospheric Inversion Method

The same transport model and inversion system was applied to the PDM data as was used for the inverse modelling of halocarbon emissions from the Eastern Mediterranean (Chapter 5). FLEXPART backward simulations were performed on a three-hourly basis for a release altitude of 2200 m a.s.l. for PDM. Similar to other mountain top observations, this height presents a compromise between the actual station altitude and the model elevation. The atmospheric inversion was calculated for the complete year of 2014 and the compounds HFC-134a, HFC-125 and HFC-152a using the filtered observations from PDM (Figure 6.5) and combining these with data from the same period at Mace Head (MHD), Jungfraujoch (JFJ) and Monte Cimone (CMN). The same Bayesian inversion system was applied to derive the spatial distribution of annual average emissions as described in Chapter 5. Here, the method following *Stohl et al.* [2009] to derive the data-mismatch uncertainty covariance matrix (S-MS in Section 5.2.8) was chosen and no further sensitivity inversions were conducted. A priori emissions were taken from UNFCCC reports for the year 2014 and were spatially disaggregated by population density. For individual regions (see Figure 6.4 for region definitions and inversion domain) the total a priori uncertainty was arbitrarily set to 50%, with the exception of HFC-152a emissions from Italy, Slovenia and Croatia. In these countries HFC-152a is only reported as part of unspecified HFC emissions and the a priori uncertainty was set to 100 %. A priori baseline mixing ratios were taken from the REBS method [*Ruckstuhl, et al.*, 2012] independently applied to each site and compound (see Section 5.2.3). In order to document the added value of the PDM observations, two sets of inversions were carried out: one including the observations from PDM and another one without these observations, only relying on data from MHD, JFJ, and CMN. Both inversions used irregular inversion grids with the size of the grid cells inversely

related to the FLEXPART simulated total source sensitivity. When omitting the PDM observations from the inversion, the inversion grid was coarser resolved over the Iberian Peninsula and Southern France.

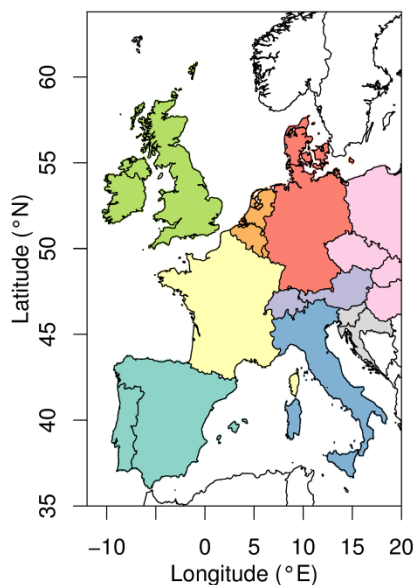


Figure 6.4: Indication of regions/countries for which individual emission estimates were derived (the country abbreviations follow the ISO 2-letter country codes): United Kingdom, Ireland (UK-IR: green), Spain, Portugal (ES-PT: turquoise), France (FR: yellow), Italy (IT: blue), Switzerland, Austria, Liechtenstein (CH-AT-LI: purple), Belgium, Netherlands, Luxembourg (BE-NL-LU: orange), Germany, Denmark (DE-DK: red), Poland, Czech Republic, Slovakia, Hungary (PL-CZ-SK-HU: pink), Slovenia, Croatia (SI-HR: grey).

6.4 Simulated Mole Fractions

Observed and simulated time series of three-hourly HFC-134a values showed a relatively close agreement at all sites (Figure 6.5). Many of the observed pollution peaks were already captured by the simulation using the a priori simulations. The Pearson correlation coefficient for the a priori simulations was better than 0.65 for all sites and was improved after the inversion with a posteriori simulations showing correlation coefficient between 0.7 for CMN and 0.9 for MHD (Figure 6.6). The agreement between observations and simulations was very similar for the two mountain top sites JFJ and PDM, whereas generally better performance was reached for the remote coastal site at MHD (Figure 6.6). As also seen in previous inversions (see Chapter 5), the normalised standard deviation was reduced in the a posteriori simulations and further away from the ideal value of unity than in the a priori simulations. In combination, the increased correlation coefficient and the reduced normalised standard deviation resulted in slightly reduced Taylor skill scores for the a posteriori simulation. However, the simulated RMSE was reduced by more than 15 % at all sites, lending credibility to the inverse modelling results.

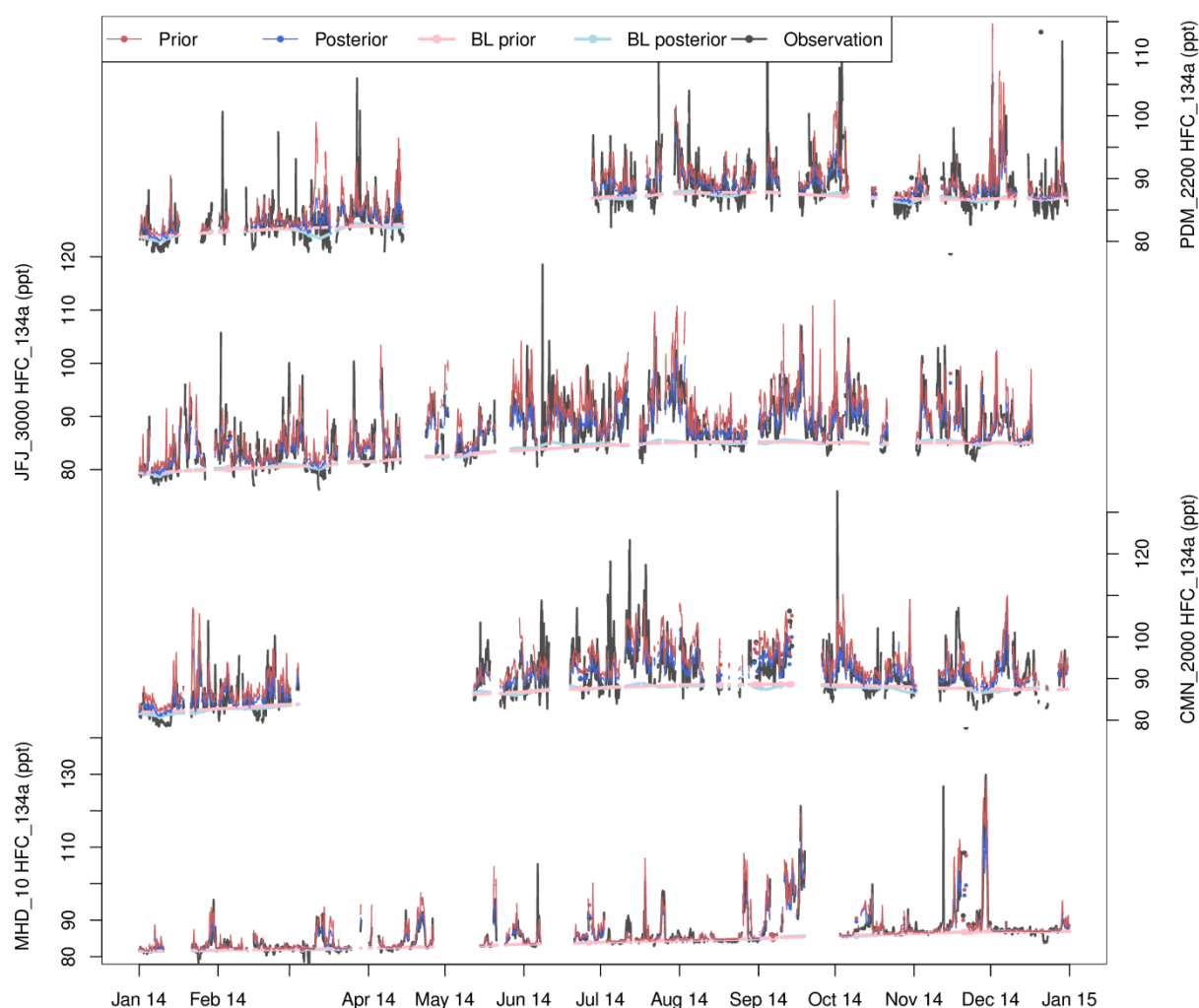


Figure 6.5: Observed (black) and simulated (prior: red; posterior: blue) HFC-134a time series at the four sites Pic du Midi (PDM), Jungfrauoch (JFJ), Monte Cimone (CMN) and Mace Head (MHD). Also given are the baseline mole fractions as used in the simulations (prior: light red; posterior: light blue). Note that the y axes were scaled for each site separately. All data represent 3-hourly averages.

For HFC-125 simulations the same tendencies of the comparison statistics (improved correlation and RMSE, slightly degraded normalised standard deviation) as for HFC-134a were achieved (Figure 6.6). For HFC-152a and at all sites the simulation performed much worse than for the other two HFCs. However, the performance somewhat improved through the inversion, reaching correlation coefficients in the range from 0.6 to 0.7 and normalised standard deviations around 0.5 (Figure 6.6). For PDM the model performance for HFC-152a was reduced as compared with the other sites, possibly indicating a certain degree of local pollution affecting the observations which the model could not account for. This was already expected based on local flask samples in the laboratory building, showing mole fractions a factor of ~100-200 higher than the atmospheric background.

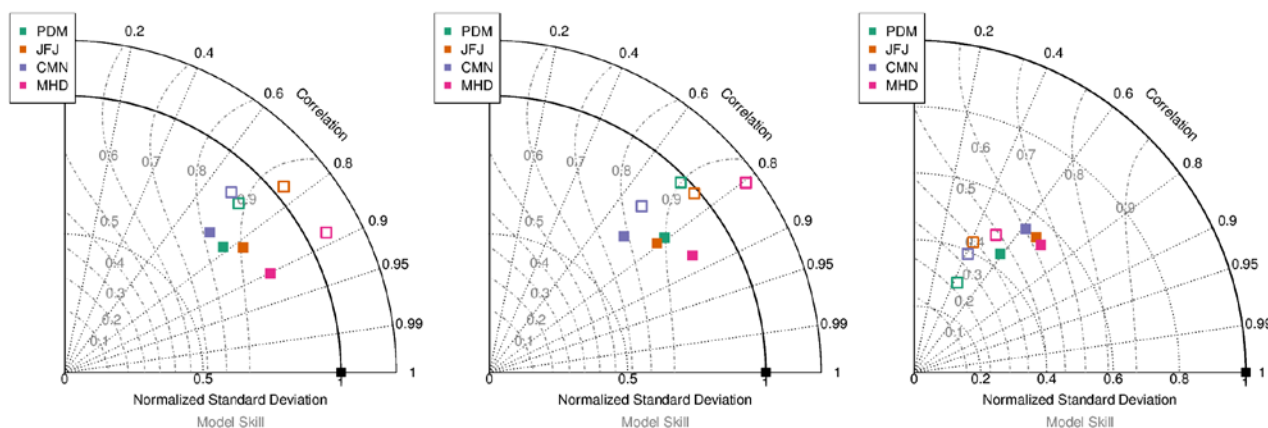


Figure 6.6: Taylor plots of the model performance for (left) HFC-134a, (centre) HFC-125, (right) HFC-152a at the four observation sites and for (open symbols) a priori and (filled symbols) a posteriori emissions.

6.5 Regional Emission Estimates

The atmospheric inversion of HFC-134a observations resulted in generally smaller a posteriori than a priori emissions throughout most of Western and Central Europe (Figure 6.7). In agreement with the previous inverse modelling results for the year 2013 (Chapter 5), these reductions were especially pronounced in Germany, France and Spain (Figure 6.7). A smaller reduction from a priori to a posteriori was established for the UK, which is in contrast to the results for 2013 when also reductions by a factor of two were established for the British Isles. When comparing the inversion results for the runs with and without PDM, the differences in the emission distribution appear small. Although emissions were established with higher resolution for the Iberian Peninsula when using the PDM observations, the total HFC-134a emissions from this region were essentially the same (Figure 6.7). However, adding the observations from PDM considerably reduced the a posteriori uncertainties for the Iberian Peninsula. Even when looking at the spatial emission distribution within Spain, the similarities between both inversions (with and without PDM) are striking (Figure 6.8). A posteriori emissions were mostly smaller than a priori emissions except for an area west of Madrid, which showed larger than a priori emissions in both inversions. However, the inversion using PDM was able to allocate emission differences in much more detail as if PDM was not included. For example, it is interesting to note that this inversion strongly reduced emission for the grid cells containing the cities of Bilbao (northern Spanish coast) and Barcelona (north-eastern Mediterranean coast) while increasing the emissions for the area of Zaragoza (central north-eastern Spain). On the French side of the Pyrenees the inversion also predicted smaller emissions for the urban areas of Toulouse, Pau and Tarbes. Total French emissions were virtually unaffected by the use of observations from PDM.

For HFC-125 a similar picture was observed: a posteriori emissions for the Iberian Peninsula were very similar whether or not PDM simulations were used in the inversion (Figure 6.7 and Figure 6.8). However, there was a stronger (not significant) tendency towards lower emission from the Iberian Peninsula when using PDM, whereas emission from France again remained unaltered.

For HFC-152a large differences were seen for the inversions including or omitting observations from PDM (Figure 6.8). However, as indoor concentrations for HFC-152a were massively higher than in ambient air, this could have been caused by leakages from the building and no quantitative assessment of national sources was performed.

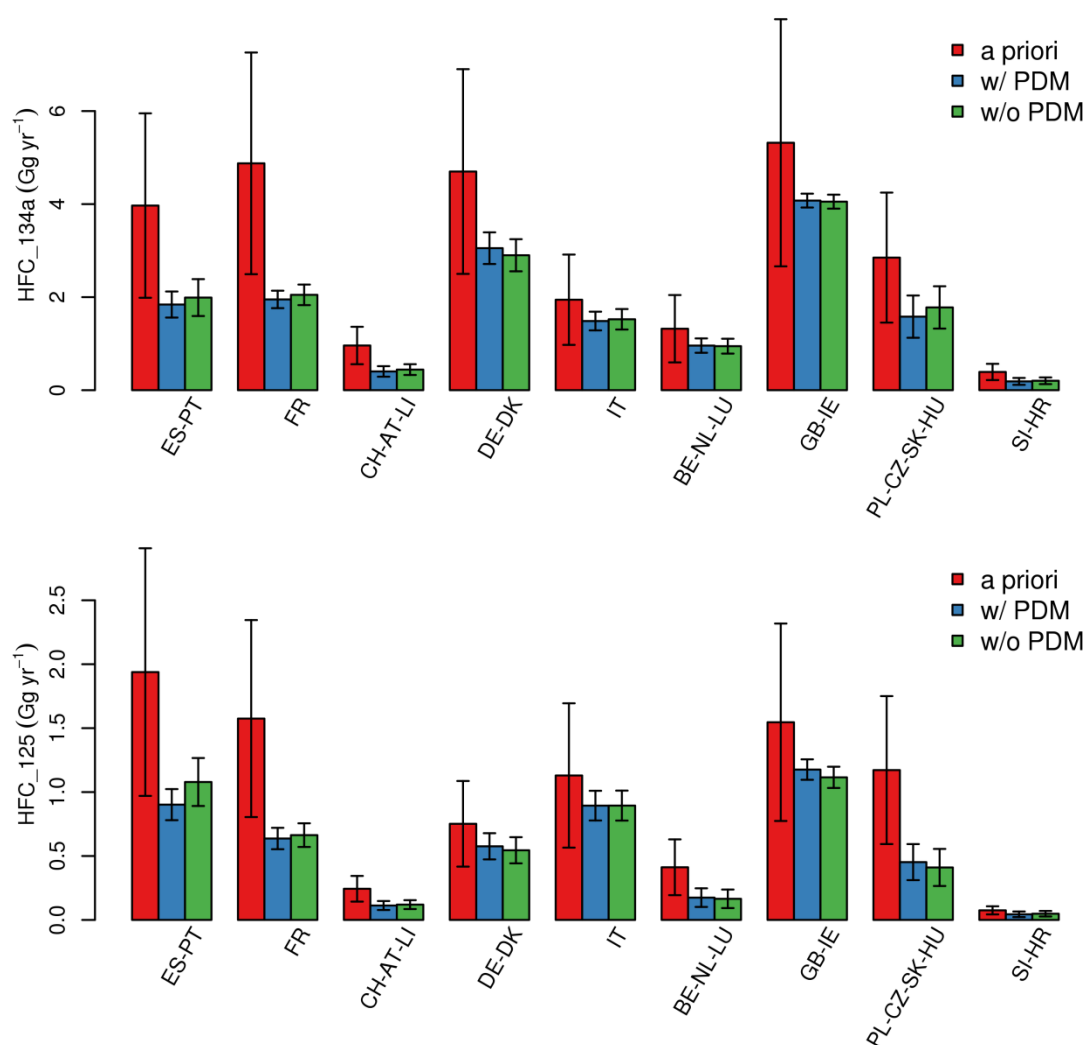


Figure 6.7: Annual average emissions for different Western and Central European countries/regions for the year 2014: (top) HFC-134a, (bottom) HFC-125. A priori values are given in red, a posteriori values in blue and green for the inversion with and without PDM, respectively. The error bars represent the 1-s uncertainty of the annual average emissions.

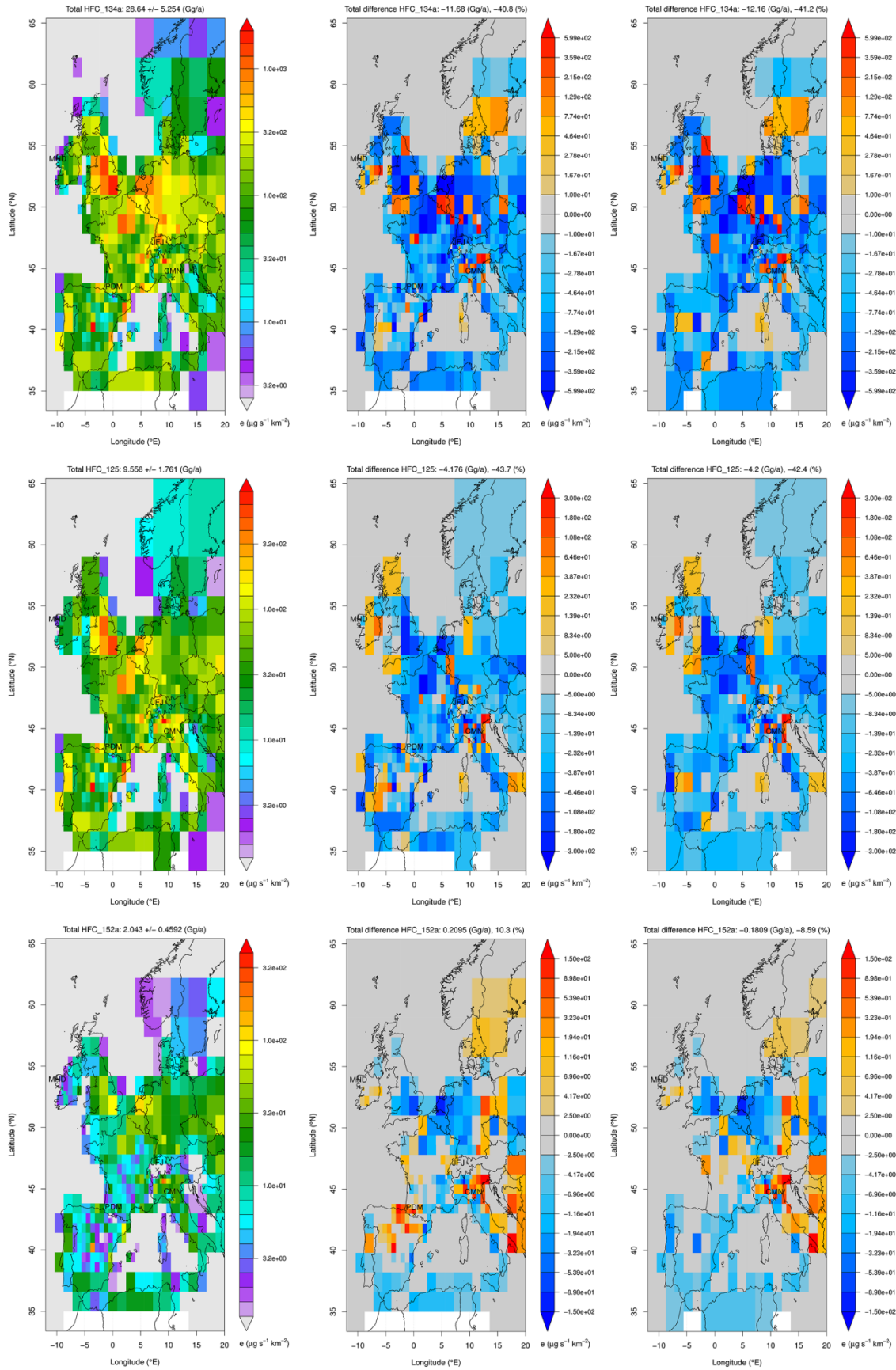


Figure 6.8: Annual average emission distribution of (top) HFC-134a, (middle) HFC-125 and (bottom) HFC-152a: (left) a priori, (centre) a posteriori difference with PDM, (right) a posteriori difference without PDM for the year 2014.

Chapter 7 Conclusion and Outlook

This PhD thesis addressed the detection of unmonitored halocarbons in the troposphere and the quantitative source attribution of regional halocarbon emissions, including measurements from two campaigns in regions previously not or poorly covered by observations.

The aim of the first part was the application of highly sensitive analysis techniques, incorporating a Medusa-GC-MS, to thoroughly scan the atmosphere for undetected halogenated substances (Chapter 4).

With this approach several compounds have been detected in the atmosphere, which were not monitored yet. In the course of this study research was then focused on trends and sources of HCFC-31, which was measured for the first time in the troposphere. This compound is mainly emitted as a by-product during the industrial production of HFC-32. Modelled global emission estimates showed an increase of HCFC-31 emissions in the first decade after 2000, with peak emissions of 840 t yr^{-1} in 2011 and declining emissions thereafter. Although these emissions are small compared to historical emissions of major CFCs (i.e. peaking at several hundred thousand tons per year), they are important as they may have been prevented by good factory practice. Therefore, it would be desirable to have only negligible emissions from this source and it is important not only to detect the locations where this compound is emitted, but also analyse the related production process and means for its control.

Under the Montreal Protocol emissive uses of HCFC-31 and all other HCFCs will be banned globally. However, the emission of compounds as by-products does not count as emissive use under this agreement. Regarding the fact, that also HCFC-133a was detected recently in the atmosphere from the production of HFCs [Laube, *et al.*, 2014; Vollmer, *et al.*, 2015c], emissions during the production of HFCs and potentially also from fourth generation HFOs are a long-term issue. As a consequence, a global long-term monitoring of these and other potential halogenated by-products within regionally representative measurement sites is required.

In the future, the successfully applied but laborious approach used in this study could be tremendously simplified by the application of newly available time-of-flight (TOF) mass spectrometers. They not only enable the detection of all mass fragments at the same time but also with unprecedented mass resolution. This will allow the electronic storage of mass spectrums as digital archives that could potentially replace most of the archiving of air in sampling canisters at observation sites. Such data archives from representative measurement sites would be of great value for future retrospective studies of the atmospheric history of newly detected compounds.

In recent years, atmospheric inverse modelling methods have been introduced, allowing the estimate of regional halocarbon emissions based on a combination of atmospheric observations and atmospheric transport models. Especially Lagrangian Particle Dispersion Models (LPDMs), operated in time-inversed mode, have proved to be efficient tools to derive source sensitivities required by the inverse modelling approach. The results of these “top-down” emission estimates not only provide insights about source regions of specified compounds but can also be used to support “bottom-up” inventories on the national level, reported as part of international agreements such as the Montreal Protocol and the Kyoto Protocol. In Chapter 5 and Chapter 6, the existing global halocarbon measurement network (AGAGE) was supplemented with a 6-month measurement campaign in Finokalia (Crete) and a 1.5 year measurement campaign at Pic du Midi in the French Pyrenees. These two campaigns aimed towards increasing the sensitivity of the existing network in source regions that are currently underrepresented by the existing observation network and allowed more precise emission estimates from the Southeastern Mediterranean and the Iberian Peninsula.

The remote, maritime location of Finokalia enabled the detection of emissions from Southeastern European countries such as Turkey, Greece and the Balkans as well as from North Africa and the Middle East under specific flow conditions. The addition of the observations from Finokalia to the existing AGAGE network in the inverse estimation of emissions was able to substantially alter the a posteriori emission results and increase their quality by reducing the a posteriori emission uncertainties in the Southeastern Mediterranean. In contrast, the high-alpine measurement campaign on Pic du Midi revealed a much smaller influence on inversely estimated emissions when combined with the observations from the existing AGAGE sites. However, here as well smaller uncertainties and a spatially higher resolved source attribution were achieved.

It was found that HFC emissions reported to the UNFCCC were mainly higher than our estimates, regarding the Southeastern Mediterranean region (e.g. Greece and Turkey). Only HFC-125 and HFC-143a emission estimates from Turkey agreed well with their inventories. A similar finding

towards misreported “bottom-up” HFC inventories was also found for Central and Western Europe, largely agreeing with other inverse modelling studies. This pattern was supported by the inversions of HFC-134a and HFC-125, conducted with campaign data from Pic du Midi. HCFC emissions, inferred from measurements at Finokalia, were shown to be a factor 2 higher for Egypt and the Middle East on a per-capita basis compared to the other estimated regions. In the light of the HCFC regulations of the Montreal Protocol for Article 5 countries, which recently became effective, these results could be particularly interesting for the comparison with future halocarbon measurement campaigns in these regions.

This part of the thesis shows that additional continuous observation sites or regular flask sampling, extending the current AGAGE network, can help to increase the coverage and the quality of “top-down” emission estimates on a high spatial resolution. However, the usefulness of additional measurement stations is determined by their strategic placement, defined by meteorological flow patterns and at large enough distances to existing observation sites and potential emission sources. Additionally, an initial examination of local contaminations is advised to ensure minimal local influence on measurement data.

Several long-term projects with a regional focus for the estimation of emissions have recently been devised. Examples for national projects are the Swiss Carbo Count CH and the UK-based GAUGE networks, which are both used to estimate emissions of greenhouse gases. On a continental scale the European ICOS network is also used to estimate greenhouse gas emissions and in the US, two-weekly airplane flask measurements are performed by NOAA for estimating emissions of both, greenhouse gases and ozone-depleting substances.

Although a higher spatial coverage of measurements will on its own improve “top-down” emission estimates, additional attention has also to be given to improve transport models and inversion frameworks in the future. An issue which needs to be investigated in more detail in this respect are the different uncertainties which are introduced to the results. Currently, the uncertainty covariance matrices describing the a priori state and the combined model-data-mismatch are rather subjectively defined. As a consequence, the spread of possible results, provided by the use of different approaches to define those matrices, can sometimes surpass the calculated analytical uncertainty. It would therefore be desirable to further pursue the development and thorough testing of more objective methods to quantify these introduced uncertainties, such as the application of maximum likelihood methods to estimate uncertainty covariance parameters [Michalak, *et al.*, 2005] or the recently developed hierarchical Bayesian methods [Ganesan, *et al.*, 2014].

Another parameter that has to be taken into consideration is the uncertainty introduced by the transport-model itself, which is used to characterize the source sensitivities. It is known, that it is particularly difficult for LPDMs, driven by global meteorological models, to represent processes which are defining transport to mountainous observation sites such as Jungfraujoch or Pic du Midi. Therefore, the coupling of higher resolved meteorological models for certain regions with the existing LPDMs would be desirable to ensure a better reproduction of smaller scale transport processes. Additionally also here, a better objective quantification of transport-model uncertainties is encouraged to understand the influence of the different parameters, such as the boundary layer height on the a posteriori result, provided by the inversion framework.

In summary, future focus should be on the spatial extension of the halocarbon measurement network to avoid underrepresented regions and on an improved and more objective quantification of uncertainties introduced to the inversely estimated results. With networks installed also in other highly industrialized regions of the world (e.g. South-East Asia), this could ensure the detailed verification and improvement of “bottom-up” inventories, to build the necessary trust in those monitoring instruments, allowing for a global plan of action.

References

- Agarwal, R. S., L. Kuijpers, J. A. Baker, J. Banks, S. Bernhardt, J. M. Calm, D. Clodic, K. E. Hickman, F. J. Keller, H. König, et al. (2002). *Report of the refrigeration , air conditioning and heat pumps technical options committee*, 193-197 pp., United Nations Environment Programme, Ozone Secretariat, Nairobi, Kenya.
- Andersen, S. O., M. L. Halberstadt, and N. Borgford-Parnell (2013). Stratospheric ozone, global warming, and the principle of unintended consequences - An ongoing science and policy success story, *J. Air Waste Manag. Assoc.*, *63* (6), 607-647, doi: 10.1080/10962247.2013.791349.
- Ashbaugh, L. L., W. C. Malm, and W. Z. Sadeh (1985). A residence time probability analysis of sulfur concentrations at Grand Canyon National Park, *Atmos. Environ.*, *19* (8), 1263-1270, doi: 10.1016/0004-6981(85)90256-2.
- Balsiger, C., C. Holliger, and P. Höhener (2005). Reductive dechlorination of chlorofluorocarbons and hydrochlorofluorocarbons in sewage sludge and aquifer sediment microcosms, *Chemosphere*, *61* (3), 361-373, doi: 10.1016/j.chemosphere.2005.02.087.
- Barletta, B., P. Nissenson, S. Meinardi, D. Dabdub, F. Sherwood Rowland, R. A. VanCuren, J. Pederson, G. S. Diskin, and D. R. Blake (2011). HFC-152a and HFC-134a emission estimates and characterization of CFCs, CFC replacements, and other halogenated solvents measured during the 2008 ARCTAS campaign (CARB phase) over the South Coast Air Basin of California, *Atmos. Chem. Phys.*, *11* (6), 2655-2669, doi: 10.5194/acp-11-2655-2011.
- Bergamaschi, P., M. Corazza, U. Karstens, M. Athanassiadou, R. L. Thompson, I. Pison, A. J. Manning, P. Bousquet, A. Segers, A. T. Vermeulen, et al. (2015). Top-down estimates of European CH₄ and N₂O emissions based on four different inverse models, *Atmos. Chem. Phys.*, *15* (2), 715-736, doi: 10.5194/acp-15-715-2015.
- Bhatnagar, A., and R. W. Carr (1996). HCFC-31: the CHClFO₂ + NO -> CHClFO + NO₂ reaction and Cl atom elimination from CHClFO, *Chem. Phys. Lett.*, *258* (5), 651-656, doi: 10.1016/0009-2614(96)00704-X.
- Bonasoni, P., A. Stohl, P. Cristofanelli, F. Calzolari, T. Colombo, and F. Evangelisti (2000). Background ozone variations at Mt. Cimone Station, *Atmos. Environ.*, *34* (29-30), 5183-5189, doi: 10.1016/S1352-2310(00)00268-5.
- Braathen, G. O., A. L. Nohende Ajavon, P. A. Newman, J. Pyle, A. R. Ravishankara, J. F. Bornman, N. D. Paul, X. Tang, S. O. Andersen, and L. Kuijpers (2012). *Handbook for the Montreal Protocol on Substances that Deplete the Ozone Layer*, United Nations Environment Programme, Ozone Secretariat, Nairobi, Kenya.

- Brunner, D., T. Arnold, S. Henne, A. J. Manning, R. L. Thompson, M. Maione, S. O'Doherty, and S. Reimann (2016). Comparison of four inverse modelling systems applied to the estimation of HFC-125, HFC-134a and SF₆ emissions over Europe, *in preparation*.
- Brunner, D., S. Henne, C. A. Keller, S. Reimann, M. K. Vollmer, S. O'Doherty, and M. Maione (2012a). An extended Kalman-filter for regional scale inverse emission estimation, *Atmos. Chem. Phys.*, 12 (7), 3455-3478, doi: 10.5194/acp-12-3455-2012.
- Brunner, D., S. Henne, C. A. Keller, M. K. Vollmer, S. Reimann, and B. Buchmann (2012b). Estimating European Halocarbon Emissions Using Lagrangian Backward Transport Modeling and in Situ Measurements at the Jungfraujoch High-Alpine Site, in *Lagrangian Modeling of the Atmosphere*, edited by J. Lin, D. Brunner, C. Gerbig, A. Stohl, A. Luhar and P. Webley, pp. 207-222, American Geophysical Union, Washington, D.C.
- Carpenter, L. J., and S. Reimann (Lead Authors) J. B. Burkholder, C. Clerbaux, B. D. Hall, R. Hossaini, J. C. Laube and S. A. Yvon-Lewis (2014). Ozone-Depleting Substances (ODSs) and Other Gases of Interest to the Montreal Protocol, Chapter 1 in *Scientific Assessment of Ozone Depletion: 2014*, Global Ozone Research and Monitoring Project - Report No. 55, World Meteorological Organization, Geneva, Switzerland.
- Charmet, A. P., P. Stoppa, N. Tasinato, S. Giorgianni, V. Barone, M. Biczysko, J. Bloino, C. Cappelli, I. Carnimeo, and C. Puzzarini (2013). An integrated experimental and quantum-chemical investigation on the vibrational spectra of chlorofluoromethane, *J. Chem. Phys.*, 139 (16), 164302, doi: 10.1063/1.4825380.
- Chipperfield, M. (1991). Stratospheric ozone depletion over the Arctic, *Nature*, 349 (6307), 279-280, doi: 10.1038/349279a0.
- Clemmer, P. G., A. M. Smith, H. S. Tung, and J. S. Bass (2002). Process for the production of Difluoromethane, Allied Signal Inc., Patent No. US 6365580 B1, Washington D. C., USA.
- Cunnold, D. M., R. G. Prinn, R. A. Rasmussen, P. G. Simmonds, F. N. Alyea, C. A. Cardelino, A. J. Crawford, P. J. Fraser, and R. D. Rosen (1983). The Atmospheric Lifetime Experiment: 3. Lifetime methodology and application to three years of CFCl₃ data, *J. Geophys. Res. Oceans*, 88 (C13), 8379-8400, doi: 10.1029/JC088iC13p08379.
- Derwent, R. G., P. G. Simmonds, B. R. Grealley, S. O'Doherty, A. McCulloch, A. Manning, S. Reimann, D. Folini, and M. K. Vollmer (2007). The phase-in and phase-out of European emissions of HCFC-141b and HCFC-142b under the Montreal Protocol: Evidence from observations at Mace Head, Ireland and Jungfraujoch, Switzerland from 1994 to 2004, *Atmos. Environ.*, 41 (4), 757-767, doi: 10.1016/j.atmosenv.2006.09.009.
- DFG (2013). Carcinogenic Substances, in *List of MAK and BAT Values 2013*, edited by Deutsche-Forschungsgemeinschaft, pp. 155-173, Wiley-VCH Verlag GmbH & Co. KGaA, Weinheim, Germany.
- Eckert, E., A. Laeng, S. Lossow, S. Kellmann, G. Stiller, T. von Clarmann, N. Glatthor, M. Höpfner, M. Kiefer, H. Oelhaf, et al. (2016). MIPAS IMK/IAA CFC-11 (CCl₃F) and CFC-12 (CCl₂F₂) measurements: accuracy, precision and long-term stability, *Atmos. Meas. Tech.*, 9 (7), 3355-3389, doi: 10.5194/amt-9-3355-2016.

- Enting, I. G. (2002). *Inverse Problems in Atmospheric Constituent Transport*, Cambridge University Press, Cambridge, United Kingdom.
- Fang, X., A. Stohl, Y. Yokouchi, J. Kim, S. Li, T. Saito, S. Park, and J. Hu (2015). Multiannual Top-Down Estimate of HFC-23 Emissions in East Asia, *Environ. Sci. Technol.*, *49* (7), 4345-4353, doi: 10.1021/es505669j.
- Fang, X., R. L. Thompson, T. Saito, Y. Yokouchi, J. Kim, S. Li, K. R. Kim, S. Park, F. Graziosi, and A. Stohl (2014). Sulfur hexafluoride (SF₆) emissions in East Asia determined by inverse modeling, *Atmos. Chem. Phys.*, *14* (9), 4779-4791, doi: 10.5194/acp-14-4779-2014.
- Farman, J. (1990). Halocarbons and Stratospheric Ozone — a Warning from Antarctica, in *Sustaining Earth: Response to the Environmental Threat*, edited by D. J. R. Angell, J. D. Comer and M. L. N. Wilkinson, pp. 71-76, Palgrave Macmillan, London, United Kingdom.
- Farman, J. C., B. G. Gardiner, and J. D. Shanklin (1985). Large losses of total ozone in Antarctica reveal seasonal ClO_x/NO_x interaction, *Nature*, *315* (6016), 207-210, doi: 10.1038/315207a0.
- Frischknecht, R. (1999). Umweltrelevanz natürlicher Kältemittel: Ökobilanzen von Wärmepumpen und Kälteanlagen, Forschungsprogramm Umgebungs- und Abwärme, Bundesamt für Energie, Bern, Switzerland.
- Fu, X., N. Maruszczak, L. E. Heimbürger, B. Sauvage, F. Gheusi, E. M. Prestbo, and J. E. Sonke (2016). Atmospheric mercury speciation dynamics at the high-altitude Pic du Midi Observatory, Southern France, *Atmos. Chem. Phys.*, *16* (9), 5623-5639, doi: 10.5194/acp-16-5623-2016.
- Ganesan, A. L., M. Rigby, A. Zammit-Mangion, A. J. Manning, R. G. Prinn, P. J. Fraser, C. M. Harth, K. R. Kim, P. B. Krummel, S. Li, et al. (2014). Characterization of uncertainties in atmospheric trace gas inversions using hierarchical Bayesian methods, *Atmos. Chem. Phys.*, *14* (8), 3855-3864, doi: 10.5194/acp-14-3855-2014.
- Gerasopoulos, E., G. Kouvarakis, M. Vrekoussis, M. Kanakidou, and N. Mihalopoulos (2005). Ozone variability in the marine boundary layer of the eastern Mediterranean based on 7-year observations, *J. Geophys. Res. Atmos.*, *110* (D15), D15309, doi: 10.1029/2005JD005991.
- Gerbig, C., S. Körner, and J. C. Lin (2008). Vertical mixing in atmospheric tracer transport models: error characterization and propagation, *Atmos. Chem. Phys.*, *8* (3), 591-602, doi: 10.5194/acp-8-591-2008.
- Gheusi, F., F. Ravetta, H. Delbarre, C. Tsamalis, A. Chevalier-Rosso, C. Leroy, P. Augustin, R. Delmas, G. Ancellet, G. Athier, et al. (2011). Pic 2005, a field campaign to investigate low-tropospheric ozone variability in the Pyrenees, *Atmos. Res.*, *101* (3), 640-665, doi: 10.1016/j.atmosres.2011.04.014.
- Graziosi, F., J. Arduini, F. Furlani, U. Giostra, L. J. M. Kuijpers, S. A. Montzka, B. R. Miller, S. J. O'Doherty, A. Stohl, P. Bonasoni, et al. (2015). European emissions of HCFC-22 based on eleven years of high frequency atmospheric measurements and a Bayesian inversion method, *Atmos. Environ.*, *112*, 196-207, doi: 10.1016/j.atmosenv.2015.04.042.

- Greally, B. R., A. J. Manning, S. Reimann, A. McCulloch, J. Huang, B. L. Dunse, P. G. Simmonds, R. G. Prinn, P. J. Fraser, D. M. Cunnold, et al. (2007). Observations of 1,1-difluoroethane (HFC-152a) at AGAGE and SOGE monitoring stations in 1994–2004 and derived global and regional emission estimates, *J. Geophys. Res. Atmos.*, *112* (D6), 2156-2202, doi: 10.1029/2006JD007527.
- Hanna, S. R. (1982). Applications in Air Pollution Modeling, in *Atmospheric Turbulence and Air Pollution Modelling: A Course held in The Hague, 21–25 September, 1981*, edited by F. T. M. Nieuwstadt and H. van Dop, pp. 275-310, Springer, Dordrecht, Netherlands.
- Harris, N. R. P., and D. J. Wuebbles (Lead Authors) J. S. Daniel, J. Hu, L. J. M. Kuijpers, K. S. Law, M. J. Prather and R. Schofield (2014). Scenarios and information for policymakers, Chapter 5 in *Scientific Assessment of Ozone Depletion*, Global Ozone Research and Monitoring Project - Report No. 55, World Meteorological Organization, Geneva, Switzerland.
- Haynes, P. H. (2005). Transport and Mixing in the Atmosphere, in *Mechanics of the 21st Century: Proceedings of the 21st International Congress of Theoretical and Applied Mechanics, Warsaw, Poland, 15–21 August 2004*, edited by W. Gutkowski and T. A. Kowalewski, pp. 139-152, Springer, Dordrecht, Netherlands.
- Henne, S., D. Brunner, D. Folini, S. Solberg, J. Klausen, and B. Buchmann (2010). Assessment of parameters describing representativeness of air quality in-situ measurement sites, *Atmos. Chem. Phys.*, *10* (8), 3561-3581, doi: 10.5194/acp-10-3561-2010.
- Henne, S., D. Brunner, B. Oney, M. Leuenberger, W. Eugster, I. Bamberger, F. Meinhardt, M. Steinbacher, and L. Emmenegger (2016). Validation of the Swiss methane emission inventory by atmospheric observations and inverse modelling, *Atmos. Chem. Phys.*, *16* (6), 3683-3710, doi: 10.5194/acp-16-3683-2016.
- Henne, S., D. E. Shallcross, S. Reimann, P. Xiao, D. Brunner, S. O'Doherty, and B. Buchmann (2012). Future Emissions and Atmospheric Fate of HFC-1234yf from Mobile Air Conditioners in Europe, *Environ. Sci. Technol.*, *46* (3), 1650-1658, doi: 10.1021/es2034608.
- Herrmann, E., E. Weingartner, S. Henne, L. Vuilleumier, N. Bukowiecki, M. Steinbacher, F. Conen, M. Collaud Coen, E. Hammer, Z. Jurányi, et al. (2015). Analysis of long-term aerosol size distribution data from Jungfraujoch with emphasis on free tropospheric conditions, cloud influence, and air mass transport, *J. Geophys. Res. Atmos.*, *120* (18), 9459-9480, doi: 10.1002/2015JD023660.
- Hodnebrog, Ø., M. Etminan, J. S. Fuglestad, G. Marston, G. Myhre, C. J. Nielsen, K. P. Shine, and T. J. Wallington (2013). Global warming potentials and radiative efficiencies of halocarbons and related compounds: A comprehensive review, *Rev. Geophys.*, *51* (2), 300-378, doi: 10.1002/rog.20013.
- Höhener, P., D. Werner, C. Balsiger, and G. Pasteris (2003). Worldwide Occurrence and Fate of Chlorofluorocarbons in Groundwater, *Crit. Rev. Env. Sci. Tec.*, *33* (1), 1-29, doi: 10.1080/10643380390814433.

- Hu, L., S. A. Montzka, J. B. Miller, A. E. Andrews, S. J. Lehman, B. R. Miller, K. Thoning, C. Sweeney, H. Chen, D. S. Godwin, et al. (2015). U.S. emissions of HFC-134a derived for 2008–2012 from an extensive flask-air sampling network, *J. Geophys. Res. Atmos.*, 120 (2), 801-825, doi: 10.1002/2014JD022617.
- IPCC (2013). Climate Change 2013: The Physical Science Basis. Contribution of Working Group I to the Fifth Assessment Report of the Intergovernmental Panel on Climate Change, edited by T. F. Stocker, D. Qin, G. K. Plattner, M. Tignor, S. K. Allen, J. Boschung, A. Nauels, Y. Xia, V. Bex and P. M. Midgley, p. 1535, Cambridge University Press, Cambridge, United Kingdom and New York, NY, USA, doi: 10.1017/CBO9781107415324.
- IPCC (2014a). Climate Change 2014: Impacts, Adaptation, and Vulnerability. Part A: Global and Sectoral Aspects. Contribution of Working Group II to the Fifth Assessment Report of the Intergovernmental Panel on Climate Change, edited by C. B. Field, V. R. Barros, D. J. Dokken, K. J. Mach, M. D. Mastrandrea, T. E. Bilir, M. Chatterjee, K. L. Ebi, Y. O. Estrada, R. C. Genova, B. Girma, E. S. Kissel, A. N. Levy, S. MacCracken, P. R. Mastrandrea and L. L. White, p. 1132, Cambridge University Press, Cambridge, United Kingdom and New York, NY, USA.
- IPCC (2014b). Climate Change 2014: Synthesis Report. Contribution of Working Groups I, II and III to the Fifth Assessment Report of the Intergovernmental Panel on Climate Change, edited by R. K. Pachauri and L. A. Meyer, IPCC, Geneva, Switzerland.
- IPCC/TEAP (2005). Safeguarding the Ozone Layer and the Global Climate System: Issues Related to Hydrofluorocarbons and Perfluorocarbons (SROC), edited by B. Metz, L. Kuijpers, S. Solomon, S. O. Andersen, O. Davidson, J. Pons, D. de Jager, T. Kestin, M. Manning and L. Meyer, p. 478, Cambridge, United Kingdom.
- Jacob, D. (1999). *Introduction to Atmospheric Chemistry*, Princeton University Press, Princeton, USA.
- Jones, A. E., and J. D. Shanklin (1995). Continued decline of total ozone over Halley, Antarctica, since 1985, *Nature*, 376 (6539), 409-411, doi: 10.1038/376409a0.
- JRC/PBL (2009). Emission Database for Global Atmospheric Research (EDGAR), release version 4.0, Tech. rep. available at: <http://edgar.jrc.ec.europa.eu>.
- Keller, C. A., D. Brunner, S. Henne, M. K. Vollmer, S. O'Doherty, and S. Reimann (2011). Evidence for under-reported western European emissions of the potent greenhouse gas HFC-23, *Geophys. Res. Lett.*, 38 (15), L15808, doi: 10.1029/2011GL047976.
- Keller, C. A., M. Hill, M. K. Vollmer, S. Henne, D. Brunner, S. Reimann, S. O'Doherty, J. Arduini, M. Maione, Z. Ferenczi, et al. (2012). European Emissions of Halogenated Greenhouse Gases Inferred from Atmospheric Measurements, *Environ. Sci. Technol.*, 46 (1), 217-225, doi: 10.1021/es202453j.
- Kim, J., S. Li, K. R. Kim, A. Stohl, J. Mühle, S. K. Kim, M. K. Park, D. J. Kang, G. Lee, C. M. Harth, et al. (2010). Regional atmospheric emissions determined from measurements at Jeju Island, Korea: Halogenated compounds from China, *Geophys. Res. Lett.*, 37 (12), L12801, doi: 10.1029/2010GL043263.

- Kloss, C., M. J. Newland, D. E. Oram, P. J. Fraser, C. A. M. Brenninkmeijer, T. Röckmann, and J. C. Laube (2014). Atmospheric Abundances, Trends and Emissions of CFC-216ba, CFC-216ca and HCFC-225ca, *Atmosphere*, 5 (2), 420-434, doi: 10.3390/atmos5020420.
- Kouvarakis, G., K. Tsigaridis, M. Kanakidou, and N. Mihalopoulos (2000). Temporal variations of surface regional background ozone over Crete Island in the southeast Mediterranean, *J. Geophys. Res. Atmos.*, 105 (D4), 4399-4407, doi: 10.1029/1999JD900984.
- Langenfelds, R. L., P. J. Fraser, R. J. Francey, L. P. Steele, L. W. Porter, and C. E. Allison (1996). *The Cape Grim air archive: The first seventeen years, 1978-1995*, Bureau of Meteorology and CSIRO Division of Atmospheric Research, Melbourne, Australia.
- Langenfelds, R. L., P. B. Krummel, P. J. Fraser, L. P. Steele, J. Ward, and N. T. Somerville (2014). Archiving of Cape Grim air, in *Baseline Atmospheric Program Australia 2009-2010*, edited by N. Derek, P. B. Krummel and S. J. Cleland, pp. 44-45, Australian Bureau of Meteorology and CSIRO Marine and Atmospheric Research.
- Laube, J., C., M. J. Newland, C. Hogan, C. A. M. Brenninkmeijer, P. J. Fraser, P. Martinerie, D. E. Oram, C. E. Reeves, T. Rockmann, J. Schwander, et al. (2014). Newly detected ozone-depleting substances in the atmosphere, *Nat. Geosci.*, 7 (4), 266-269, doi: 10.1038/ngeo2109.
- Levin, I., T. Naegler, R. Heinz, D. Osusko, E. Cuevas, A. Engel, J. Ilmberger, R. L. Langenfelds, B. Neininger, C. v. Rohden, et al. (2010). The global SF₆ source inferred from long-term high precision atmospheric measurements and its comparison with emission inventories, *Atmos. Chem. Phys.*, 10 (6), 2655-2662, doi: 10.5194/acp-10-2655-2010.
- Lovelock, J. E. (1974). The electron capture detector, *J. Chromatogr. A*, 99, 3-12, doi: 10.1016/S0021-9673(00)90840-9.
- Lovelock, J. E., and A. J. Watson (1978). Electron-capture detector: Theory and practice II, *J. Chromatogr. A*, 158, 123-138, doi: 10.1016/S0021-9673(00)89961-6.
- Lunt, M. F., M. Rigby, A. L. Ganesan, A. J. Manning, R. G. Prinn, S. O'Doherty, J. Mühle, C. M. Harth, P. K. Salameh, T. Arnold, et al. (2015). Reconciling reported and unreported HFC emissions with atmospheric observations, *Proc. Natl. Acad. Sci. U.S.A.*, 112 (19), 5927-5931, doi: 10.1073/pnas.1420247112.
- Maione, M., U. Giostra, J. Arduini, F. Furlani, F. Graziosi, E. Lo Vullo, and P. Bonasoni (2013). Ten years of continuous observations of stratospheric ozone depleting gases at Monte Cimone (Italy) — Comments on the effectiveness of the Montreal Protocol from a regional perspective, *Sci. Total Environ.*, 445–446, 155-164, doi: 10.1016/j.scitotenv.2012.12.056.
- Maione, M., F. Graziosi, J. Arduini, F. Furlani, U. Giostra, D. R. Blake, P. Bonasoni, X. Fang, S. A. Montzka, S. J. O'Doherty, et al. (2014). Estimates of European emissions of methyl chloroform using a Bayesian inversion method, *Atmos. Chem. Phys.*, 14 (18), 9755-9770, doi: 10.5194/acp-14-9755-2014.
- Manning, A. J., D. B. Ryall, R. G. Derwent, P. G. Simmonds, and S. O'Doherty (2003). Estimating European emissions of ozone-depleting and greenhouse gases using observations and a modeling back-attribution technique, *J. Geophys. Res. Atmos.*, 108 (D14), 2156-2202, doi: 10.1029/2002JD002312.

- McCulloch, A., P. Ashford, and P. M. Midgley (2001). Historic emissions of fluorotrichloromethane (CFC-11) based on a market survey, *Atmos. Environ.*, *35* (26), 4387-4397, doi: 10.1016/s1352-2310(01)00249-7.
- Michalak, A. M., A. Hirsch, L. Bruhwiler, K. R. Gurney, W. Peters, and P. P. Tans (2005). Maximum likelihood estimation of covariance parameters for Bayesian atmospheric trace gas surface flux inversions, *J. Geophys. Res. Atmos.*, *110* (D24), 2156-2202, doi: 10.1029/2005JD005970.
- Midgley, P. M., and A. McCulloch (1999). Properties and Applications of Industrial Halocarbons, in *Reactive Halogen Compounds in the Atmosphere*, edited by P. Fabian and O. N. Singh, pp. 129-153, Springer, Berlin, Heidelberg, Germany.
- Miller, B. R., and L. J. M. Kuijpers (2011). Projecting future HFC-23 emissions, *Atmos. Chem. Phys.*, *11* (24), 13259-13267, doi: 10.5194/acp-11-13259-2011.
- Miller, B. R., R. F. Weiss, P. K. Salameh, T. Tanhua, B. R. Grealley, J. Mühle, and P. G. Simmonds (2008). Medusa: A Sample Preconcentration and GC/MS Detector System for in Situ Measurements of Atmospheric Trace Halocarbons, Hydrocarbons, and Sulfur Compounds, *Anal. Chem.*, *80* (5), 1536-1545, doi: 10.1021/ac702084k.
- Molina, M. J., and F. S. Rowland (1974). Stratospheric sink for chlorofluoromethanes: chlorine atom-catalysed destruction of ozone, *Nature*, *249* (5460), 810-812, doi: 10.1038/249810a0.
- Montzka, S. A., B. D. Hall, and J. W. Elkins (2009). Accelerated increases observed for hydrochlorofluorocarbons since 2004 in the global atmosphere, *Geophys. Res. Lett.*, *36* (3), L03804, doi: 10.1029/2008GL036475.
- Montzka, S. A., M. McFarland, S. O. Andersen, B. R. Miller, D. W. Fahey, B. D. Hall, L. Hu, C. Siso, and J. W. Elkins (2015). Recent Trends in Global Emissions of Hydrochlorofluorocarbons and Hydrofluorocarbons: Reflecting on the 2007 Adjustments to the Montreal Protocol, *J. Phys. Chem. A*, *119* (19), 4439-4449, doi: 10.1021/jp5097376.
- Muller, R., P. J. Crutzen, J. U. Groo, C. Burhl, J. M. Russell, H. Gernandt, D. S. McKenna, and A. F. Tuck (1997). Severe chemical ozone loss in the Arctic during the winter of 1995-96, *Nature*, *389* (6652), 709-712, doi: 10.1038/39564.
- Myhre, G., D. Shindell, F. M. Bréon, W. Collins, J. Fuglestad, J. Huang, D. Koch, J. F. Lamarque, D. Lee, B. Mendoza, et al. (2013). Anthropogenic and Natural Radiative Forcing, in *Climate Change 2013: The Physical Science Basis. Contribution of Working Group I to the Fifth Assessment Report of the Intergovernmental Panel on Climate Change*, edited by T. F. Stocker, D. Qin, G. K. Plattner, M. Tignor, S. K. Allen, J. Boschung, A. Nauels, Y. Xia, V. Bex and P. M. Midgley, pp. 659-740, Cambridge University Press, Cambridge, United Kingdom and New York, NY, USA, doi: 10.1017/CBO9781107415324.018.
- Newman, P. A., L. D. Oman, A. R. Douglass, E. L. Fleming, S. M. Frith, M. M. Hurwitz, S. R. Kawa, C. H. Jackman, N. A. Krotkov, E. R. Nash, et al. (2009). What would have happened to the ozone layer if chlorofluorocarbons (CFCs) had not been regulated?, *Atmos. Chem. Phys.*, *9* (6), 2113-2128, doi: 10.5194/acp-9-2113-2009.

- Nisbet, E., and R. Weiss (2010). Top-Down Versus Bottom-Up, *Science*, 328 (5983), 1241-1243, doi: 10.1126/science.1189936.
- NOAA-ESRL (2016a). Global Monitoring Division - Halocarbons and other Atmospheric Trace Gases (HATS) Sampling Network Site Information, available from: <http://www.esrl.noaa.gov/gmd/hats/> (Accessed 23 October 2016).
- NOAA-ESRL (2016b). Global Monitoring Division - Observatories, available from: <http://www.esrl.noaa.gov/gmd/> (Accessed 23 October 2016).
- O'Doherty, S., D. M. Cunnold, A. Manning, B. R. Miller, R. H. J. Wang, P. B. Krummel, P. J. Fraser, P. G. Simmonds, A. McCulloch, R. F. Weiss, et al. (2004). Rapid growth of hydrofluorocarbon 134a and hydrochlorofluorocarbons 141b, 142b, and 22 from Advanced Global Atmospheric Gases Experiment (AGAGE) observations at Cape Grim, Tasmania, and Mace Head, Ireland, *J. Geophys. Res. Atmos.*, 109 (D6), D06310, doi: 10.1029/2003JD004277.
- O'Doherty, S., D. M. Cunnold, B. R. Miller, J. Mühle, A. McCulloch, P. G. Simmonds, A. J. Manning, S. Reimann, M. K. Vollmer, B. R. Grealley, et al. (2009). Global and regional emissions of HFC-125 (CHF_2CF_3) from in situ and air archive atmospheric observations at AGAGE and SOGE observatories, *J. Geophys. Res. Atmos.*, 114 (D23), D23304, doi: 10.1029/2009JD012184.
- O'Doherty, S., M. Rigby, J. Mühle, D. J. Ivy, B. R. Miller, D. Young, P. G. Simmonds, S. Reimann, M. K. Vollmer, P. B. Krummel, et al. (2014). Global emissions of HFC-143a (CH_3CF_3) and HFC-32 (CH_2F_2) from in situ and air archive atmospheric observations, *Atmos. Chem. Phys.*, 14 (5), 9249-9258, doi: 10.5194/acp-14-9249-2014.
- Park, K., and T. S. Rhee (2015). Source characterization of carbon monoxide and ozone over the Northwestern Pacific in summer 2012, *Atmos. Environ.*, 111 (0), 151-160, doi: 10.1016/j.atmosenv.2015.04.015.
- Prinn, R. G., P. G. Simmonds, R. A. Rasmussen, R. D. Rosen, F. N. Alyea, C. A. Cardelino, A. J. Crawford, D. M. Cunnold, P. J. Fraser, and J. E. Lovelock (1983). The Atmospheric Lifetime Experiment: 1. Introduction, instrumentation, and overview, *J. Geophys. Res. Oceans*, 88 (C13), 8353-8367, doi: 10.1029/JC088iC13p08353.
- Prinn, R. G., R. F. Weiss, P. J. Fraser, P. G. Simmonds, D. M. Cunnold, F. N. Alyea, S. O'Doherty, P. Salameh, B. R. Miller, J. Huang, et al. (2000). A history of chemically and radiatively important gases in air deduced from ALE/GAGE/AGAGE, *J. Geophys. Res. Atmos.*, 105 (D14), 17751-17792, doi: 10.1029/2000JD900141.
- Ramanathan, V. (1975). Greenhouse Effect Due to Chlorofluorocarbons: Climatic Implications, *Science*, 190 (4209), 50-52, doi: 10.1126/science.190.4209.50.
- Reimann, S., A. J. Manning, P. G. Simmonds, D. M. Cunnold, R. H. J. Wang, J. Li, A. McCulloch, R. G. Prinn, J. Huang, R. F. Weiss, et al. (2005). Low European methyl chloroform emissions inferred from long-term atmospheric measurements, *Nature*, 433 (7025), 506-508, doi: 10.1038/nature03220.

- Reimann, S., D. Schaub, K. Stemmler, D. Folini, M. Hill, P. Hofer, B. Buchmann, P. G. Simmonds, B. R. Greally, and S. O'Doherty (2004). Halogenated greenhouse gases at the Swiss High Alpine Site of Jungfraujoch (3580 m asl): Continuous measurements and their use for regional European source allocation, *J. Geophys. Res. Atmos.*, *109* (D5), D05307, doi: 10.1029/2003JD003923.
- Reimann, S., M. K. Vollmer, D. Folini, M. Steinbacher, M. Hill, B. Buchmann, R. Zander, and E. Mahieu (2008). Observations of long-lived anthropogenic halocarbons at the high-Alpine site of Jungfraujoch (Switzerland) for assessment of trends and European sources, *Sci. Total Environ.*, *391* (2), 224-231, doi: 10.1016/j.scitotenv.2007.10.022.
- Rhew, R. C., B. R. Miller, and R. F. Weiss (2000). Natural methyl bromide and methyl chloride emissions from coastal salt marshes, *Nature*, *403* (6767), 292-295, doi: 10.1038/35002043.
- Rigby, M., A. L. Ganesan, and R. G. Prinn (2011). Deriving emissions time series from sparse atmospheric mole fractions, *J. Geophys. Res. Atmos.*, *116* (D8), D08306, doi: 10.1029/2010JD015401.
- Rigby, M., J. Mühle, B. R. Miller, R. G. Prinn, P. B. Krummel, L. P. Steele, P. J. Fraser, P. K. Salameh, C. M. Harth, R. F. Weiss, et al. (2010). History of atmospheric SF₆ from 1973 to 2008, *Atmos. Chem. Phys.*, *10* (21), 10305-10320, doi: 10.5194/acp-10-10305-2010.
- Rigby, M., R. G. Prinn, S. O'Doherty, B. R. Miller, D. Ivy, J. Mühle, C. M. Harth, P. K. Salameh, T. Arnold, R. F. Weiss, et al. (2014). Recent and future trends in synthetic greenhouse gas radiative forcing, *Geophys. Res. Lett.*, *41* (7), 2623-2630, doi: 10.1029/2013GL059099.
- Rigby, M., R. G. Prinn, S. O'Doherty, S. A. Montzka, A. McCulloch, C. M. Harth, J. Mühle, P. K. Salameh, R. F. Weiss, D. Young, et al. (2013). Re-evaluation of the lifetimes of the major CFCs and CH₃CCl₃ using atmospheric trends, *Atmos. Chem. Phys.*, *13* (5), 2691-2702, doi: 10.5194/acp-13-2691-2013.
- Robinson, S. A., and D. J. Erickson (2015). Not just about sunburn – the ozone hole's profound effect on climate has significant implications for Southern Hemisphere ecosystems, *Glob. Change Biol.*, *21* (2), 515-527, doi: 10.1111/gcb.12739.
- Ruckstuhl, A. F., S. Henne, S. Reimann, M. Steinbacher, B. Buchmann, and C. Hueglin (2012). Robust extraction of baseline signal of atmospheric trace species using local regression, *Atmos. Meas. Tech.*, *5* (11), 2613-2624, doi: 10.5194/amt-5-2613-2012.
- Saikawa, E., M. Rigby, R. G. Prinn, S. A. Montzka, B. R. Miller, L. J. M. Kuijpers, P. J. B. Fraser, M. K. Vollmer, T. Saito, Y. Yokouchi, et al. (2012). Global and regional emission estimates for HCFC-22, *Atmos. Chem. Phys.*, *12* (21), 10033-10050, doi: 10.5194/acp-12-10033-2012.
- Sander, S. P., R. R. Friedl, J. R. Barker, D. M. Golden, M. J. Kurylo, P. H. Wine, J. P. D. Abbatt, J. B. Burkholder, C. E. Kolb, G. K. Moortgat, et al. (2011). Chemical kinetics and photochemical data for use in atmospheric studies: Evaluation No. 17 of the NASA Panel for Data Evaluation, NASA/JPL, Pasadena, USA.
- Say, D., A. J. Manning, S. O'Doherty, M. Rigby, D. Young, and A. Grant (2016). Re-Evaluation of the UK's HFC-134a Emissions Inventory Based on Atmospheric Observations, *Environ. Sci. Technol.*, *50* (20), 11129-11136, doi: 10.1021/acs.est.6b03630.

- Scheifinger, H., and A. Kaiser (2007). Validation of trajectory statistical methods, *Atmos. Environ.*, *41* (39), 8846-8856, doi: 10.1016/j.atmosenv.2007.08.034.
- Scheutz, C., Y. Dote, A. M. Fredenslund, and P. Kjeldsen (2007a). Attenuation of Fluorocarbons Released from Foam Insulation in Landfills, *Environ. Sci. Technol.*, *41* (22), 7714-7722, doi: 10.1021/es0707409.
- Scheutz, C., A. M. Fredenslund, P. Kjeldsen, and M. Tant (2007b). Release of Fluorocarbons from Insulation Foam in Home Appliances during Shredding, *J. Air Waste Manag. Assoc.*, *57* (12), 1452-1460, doi: 10.3155/1047-3289.57.12.1452.
- Scheutz, C., A. M. Fredenslund, J. Nedenskov, and P. Kjeldsen (2010a). Release and fate of fluorocarbons in a shredder residue landfill cell: 1. Laboratory experiments, *Waste Manage.*, *30* (11), 2153-2162, doi: 10.1016/j.wasman.2010.03.035.
- Scheutz, C., A. M. Fredenslund, J. Nedenskov, and P. Kjeldsen (2010b). Release and fate of fluorocarbons in a shredder residue landfill cell: 2. Field investigations, *Waste Manage.*, *30* (11), 2163-2169, doi: 10.1016/j.wasman.2010.03.033.
- Scheutz, C., and P. Kjeldsen (2003). Capacity for Biodegradation of CFCs and HCFCs in a Methane Oxidative Counter-Gradient Laboratory System Simulating Landfill Soil Covers, *Environ. Sci. Technol.*, *37* (22), 5143-5149, doi: 10.1021/es026464+.
- Schoenenberger, F., M. K. Vollmer, M. Rigby, M. Hill, P. J. Fraser, P. B. Krummel, R. L. Langenfelds, T. S. Rhee, T. Peter, and S. Reimann (2015). First observations, trends, and emissions of HCFC-31 (CH_2ClF) in the global atmosphere, *Geophys. Res. Lett.*, *42* (18), 7817-7824, doi: 10.1002/2015GL064709.
- Seibert, P., and A. Frank (2004). Source-receptor matrix calculation with a Lagrangian particle dispersion model in backward mode, *Atmos. Chem. Phys.*, *4*, 51-63, doi: 10.5194/acp-4-51-2004.
- Shantan Rao, P., B. Narsaiah, Y. Rambabu, M. Sridhar, and K. V. Raghavan (2015). Catalytic Processes for Fluorochemicals: Sustainable Alternatives, in *Industrial Catalysis and Separation: Innovations for Process Intensification*, edited by K. V. Raghavan and B. M. Reddy, pp. 407-435, Apple Academic Press, Toronto, Canada.
- Simmonds, P. G., S. O'Doherty, G. Nickless, G. A. Sturrock, R. Swaby, P. Knight, J. Ricketts, G. Woffendin, and R. Smith (1995). Automated Gas Chromatograph/Mass Spectrometer for Routine Atmospheric Field Measurements of the CFC Replacement Compounds, the Hydrofluorocarbons and Hydrochlorofluorocarbons, *Anal. Chem.*, *67* (4), 717-723, doi: 10.1021/ac00100a005.
- Simmonds, P. G., M. Rigby, A. J. Manning, M. F. Lunt, S. O'Doherty, A. McCulloch, P. J. Fraser, S. Henne, M. K. Vollmer, J. Mühle, et al. (2016). Global and regional emissions estimates of 1,1-difluoroethane (HFC-152a, CH_3CHF_2) from in situ and air archive observations, *Atmos. Chem. Phys.*, *16* (1), 365-382, doi: 10.5194/acp-16-365-2016.
- Solomon, S., D. J. Ivy, D. Kinnison, M. J. Mills, R. R. Neely, and A. Schmidt (2016). Emergence of healing in the Antarctic ozone layer, *Science*, *353* (6296), 269-274, doi: 10.1126/science.aae0061.

- SPARC (2016). SPARC Report on the Mystery of Carbon Tetrachloride, edited by P. A. Q. Liang, S. Newman and S. Reimann, SPARC Report No. 7, WCRP-13/2016, available at www.sparc-climate.org/publications/sparc-reports/sparc-report-no7.
- Spivakovsky, C. M., J. A. Logan, S. A. Montzka, Y. J. Balkanski, M. Foreman-Fowler, D. B. A. Jones, L. W. Horowitz, A. C. Fusco, C. A. M. Brenninkmeijer, M. J. Prather, et al. (2000). Three-dimensional climatological distribution of tropospheric OH: Update and evaluation, *J. Geophys. Res. Atmos.*, *105* (D7), 8931-8980, doi: 10.1029/1999JD901006.
- Steinbacher, M., M. K. Vollmer, B. Buchmann, and S. Reimann (2008). An evaluation of the current radiative forcing benefit of the Montreal Protocol at the high-Alpine site Jungfraujoch, *Sci. Total Environ.*, *391* (2–3), 217-223, doi: 10.1016/j.scitotenv.2007.10.003.
- Stemmler, K., D. Folini, S. Uhl, M. K. Vollmer, S. Reimann, S. O'Doherty, B. R. Grealley, P. G. Simmonds, and A. J. Manning (2007). European Emissions of HFC-365mfc, a Chlorine-Free Substitute for the Foam Blowing Agents HCFC-141b and CFC-11, *Environ. Sci. Technol.*, *41* (4), 1145-1151, doi: 10.1021/es061298h.
- Stohl, A. (1996). Trajectory statistics-A new method to establish source-receptor relationships of air pollutants and its application to the transport of particulate sulfate in Europe, *Atmos. Environ.*, *30* (4), 579-587, doi: 10.1016/1352-2310(95)00314-2.
- Stohl, A., C. Forster, A. Frank, P. Seibert, and G. Wotawa (2005). Technical note: The Lagrangian particle dispersion model FLEXPART version 6.2, *Atmos. Chem. Phys.*, *5* (9), 2461-2474, doi: 10.5194/acp-5-2461-2005.
- Stohl, A., M. Hittenberger, and G. Wotawa (1998). Validation of the lagrangian particle dispersion model FLEXPART against large-scale tracer experiment data, *Atmos. Environ.*, *32* (24), 4245-4264, doi: 10.1016/S1352-2310(98)00184-8.
- Stohl, A., J. Kim, S. Li, S. O'Doherty, J. Mühle, P. K. Salameh, T. Saito, M. K. Vollmer, D. Wan, R. F. Weiss, et al. (2010). Hydrochlorofluorocarbon and hydrofluorocarbon emissions in East Asia determined by inverse modeling, *Atmos. Chem. Phys.*, *10* (8), 3545-3560, doi: 10.5194/acp-10-3545-2010.
- Stohl, A., P. Seibert, J. Arduini, S. Eckhardt, P. Fraser, B. R. Grealley, C. Lunder, M. Maione, J. Mühle, S. O'Doherty, et al. (2009). An analytical inversion method for determining regional and global emissions of greenhouse gases: Sensitivity studies and application to halocarbons, *Atmos. Chem. Phys.*, *9* (5), 1597-1620, doi: 10.5194/acp-9-1597-2009.
- Stohl, A., and T. Trickl (2001). Long-Range Transport of Ozone from the North American Boundary Layer to Europe: Observations and Model Results, in *Air Pollution Modeling and Its Application XIV*, edited by S. E. Gryning and F. A. Schiermeier, pp. 257-266, Springer, Boston, USA.
- Stolarski, R., R. Bojkov, L. Bishop, C. Zerefos, J. Staehelin, and J. Zawodny (1992). Measured trends in stratospheric ozone, *Science*, *256* (5055), 342, doi: 10.1126/science.256.5055.342
- Taylor, K. E. (2001). Summarizing multiple aspects of model performance in a single diagram, *J. Geophys. Res. Atmos.*, *106* (D7), 7183-7192, doi: 10.1029/2000JD900719.

- Thompson, R. L., and A. Stohl (2014). FLEXINVERT: an atmospheric Bayesian inversion framework for determining surface fluxes of trace species using an optimized grid, *Geosci. Model Dev.*, 7 (5), 2223-2242, doi: 10.5194/gmd-7-2223-2014.
- UN (2016). UN Population Division - World Population Prospects 2015, available from: <https://esa.un.org/unpd/wpp/DataQuery/> (Accessed 18 July 2016).
- UNEP (2016). Ozone Secretariat - Treaties and Decisions, available from: <http://ozone.unep.org/en/treaties-and-decisions> (Accessed 08 October 2016).
- UNFCCC (1997). Kyoto Protocol to the United Nations Framework Convention on Climate Change, available from: http://unfccc.int/kyoto_protocol/items/2830.php (Accessed).
- UNFCCC (2016a). National Inventory Submissions 2016, available from: http://unfccc.int/national_reports/annex_i_ghg_inventories/national_inventories_submissions/items/9492.php (Accessed 28 August 2016).
- UNFCCC (2016b). Status of the Doha Amendment, available from: http://unfccc.int/kyoto_protocol/doha_amendment/items/7362.php (Accessed 08 October 2016).
- UOC (2016). Finokalia Station - for Research and Education on the Environment since 1993 (University of Crete - ECPL), available from: <http://finokalia.chemistry.uoc.gr> (Accessed 12 August 2016).
- Velders, G. J. M., S. O. Andersen, J. S. Daniel, D. W. Fahey, and M. McFarland (2007). The importance of the Montreal Protocol in protecting climate, *Proc. Natl. Acad. Sci. U.S.A.*, 104 (12), 4814-4819, doi: 10.1073/pnas.0610328104.
- Velders, G. J. M., D. W. Fahey, J. S. Daniel, M. McFarland, and S. O. Andersen (2009). The large contribution of projected HFC emissions to future climate forcing, *Proc. Natl. Acad. Sci. U.S.A.*, 106 (27), 10949-10954, doi: 10.1073/pnas.0902817106.
- Velders, G. J. M., A. R. Ravishankara, M. K. Miller, M. J. Molina, J. Alcamo, J. S. Daniel, D. W. Fahey, S. A. Montzka, and S. Reimann (2012). Preserving Montreal Protocol Climate Benefits by Limiting HFCs, *Science*, 335 (6071), 922-923, doi: 10.1126/science.1216414.
- Velders, G. J. M., S. Solomon, and J. S. Daniel (2014). Growth of climate change commitments from HFC banks and emissions, *Atmos. Chem. Phys.*, 14 (9), 4563-4572, doi: 10.5194/acp-14-4563-2014.
- Vogelezang, D. H. P., and A. A. M. Holtslag (1996). Evaluation and model impacts of alternative boundary-layer height formulations, *Bound.-Lay. Meteorol.*, 81 (3), 245-269, doi: 10.1007/bf02430331.
- Vollmer, M. K., B. R. Miller, M. Rigby, S. Reimann, J. Mühle, P. B. Krummel, S. O'Doherty, J. Kim, T. S. Rhee, and R. F. Weiss (2011). Atmospheric histories and global emissions of the anthropogenic hydrofluorocarbons HFC-365mfc, HFC-245fa, HFC-227ea, and HFC-236fa, *J. Geophys. Res. Atmos.*, 116 (D8), doi: 10.1029/2010JD015309.
- Vollmer, M. K., S. Reimann, M. Hill, and D. Brunner (2015a). First Observations of the Fourth Generation Synthetic Halocarbons HFC-1234yf, HFC-1234ze(E), and HCFC-1233zd(E) in the Atmosphere, *Environ. Sci. Technol.*, 49 (5), 2703-2708, doi: 10.1021/es505123x.

- Vollmer, M. K., T. S. Rhee, M. Rigby, D. Hofstetter, M. Hill, F. Schoenenberger, and S. Reimann (2015b). Modern inhalation anesthetics: Potent greenhouse gases in the global atmosphere, *Geophys. Res. Lett.*, *42* (5), 1606-1611, doi: 10.1002/2014GL062785.
- Vollmer, M. K., M. Rigby, J. C. Laube, S. Henne, T. S. Rhee, L. J. Gooch, A. Wenger, D. Young, L. P. Steele, R. L. Langenfelds, et al. (2015c). Abrupt reversal in emissions and atmospheric abundance of HCFC-133a ($\text{CF}_3\text{CH}_2\text{Cl}$), *Geophys. Res. Lett.*, *42* (20), 8702-8710, doi: 10.1002/2015GL065846.
- Vollmer, M. K., and R. F. Weiss (2002). Simultaneous determination of sulfur hexafluoride and three chlorofluorocarbons in water and air, *Mar. Chem.*, *78* (2-3), 137-148, doi: 10.1016/S0304-4203(02)00015-4.
- Vollmer, M. K., L. X. Zhou, B. R. Grealley, S. Henne, B. Yao, S. Reimann, F. Stordal, D. M. Cunnold, X. C. Zhang, M. Maione, et al. (2009). Emissions of ozone-depleting halocarbons from China, *Geophys. Res. Lett.*, *36* (15), L15823, doi: 10.1029/2009GL038659.
- Wismer, J. A. (2003). Recovery of HFC-32, Atofina Chemicals Inc., Patent No. 6605193 B2, USA.
- World Meteorological Organization (WMO) (2014). *Scientific Assessment of Ozone Depletion*, 416 pp., World Meteorological Organization, Global Ozone Research and Monitoring Project - Report No. 55, Geneva, Switzerland.
- Xiang, B., P. K. Patra, S. A. Montzka, S. M. Miller, J. W. Elkins, F. L. Moore, E. L. Atlas, B. R. Miller, R. F. Weiss, R. G. Prinn, et al. (2014). Global emissions of refrigerants HCFC-22 and HFC-134a: Unforeseen seasonal contributions, *Proc. Natl. Acad. Sci. U.S.A.*, *111* (49), 17379-17384, doi: 10.1073/pnas.1417372111.
- Zellweger, C., J. Forrer, P. Hofer, S. Nyeki, B. Schwarzenbach, E. Weingartner, M. Ammann, and U. Baltensperger (2003). Partitioning of reactive nitrogen (NO_y) and dependence on meteorological conditions in the lower free troposphere, *Atmos. Chem. Phys.*, *3* (3), 779-796, doi: 10.5194/acp-3-779-2003.

Acknowledgements

First, I would like to address my sincerest gratitude to my dissertation supervisor Prof. Thomas Peter for his continued support of my research, his insightful comments and recommendations, as well as his motivation and patience throughout the process of this dissertation.

I would like to address my heartfelt thanks to my direct supervisors at Empa, Dr. Stefan Reimann and Dr. Dominik Brunner for their guidance, their encouragement and support over the years, which made the successful completion of this thesis possible in the first place.

I also owe gratitude to our department head, Dr. Lukas Emmenegger, for his goodwill, flexibility and support during my time at Empa.

I am grateful to all my colleagues at Empa who provided a friendly and supportive environment for my research. A special thank you also belongs to Dr. Stephan Henne, for the countless hours of support regarding the modelling and many other aspects of this project and to Matz Hill for all of his help and invaluable knowledge in organizing and setting up the measurement campaigns, maintaining the instruments, analysing the chromatographic data and making the campaigns much more enjoyable. I also want to thank Dr. Martin Vollmer for his assistance with the measurements and his recommendations, adding a lot of value to my research. I am grateful to Dr. Corinne Hörger, Simon Wyss and Benjamin Sprenger for sharing an office with me, providing an enjoyable work atmosphere and helping me in various ways. Irina Vögtle deserves a special mention for her assistance during the installation of the instrument on Pic du Midi. I would also like to thank my fellow Ph.D. students Dr. Brian Oney and Dr. Simon Eyer for the time spent together in- and outside of Empa.

Additionally, I would also like to extend special thanks to the people who were involved in the measurement campaigns, for their help with the organization and monitoring of our instruments. For the measurement campaigns in Finokalia, big thanks are owed particularly to Dr. Giorgos Kouvarakis and Prof. Nikolaos Mihalopoulos from the University of Crete. Concerning the measurement campaign on Pic du Midi, I want to specially thank Dr. François Gheusi from the University of Toulouse and the technicians at Pic du Midi.

Finally, there are no words to express my endless gratitude to my family and Carla, for all their help, their motivation and their support in every way possible to finish this thesis and beyond. Thank you!